

Spectroscopy, fundamental symmetry tests and quantum  
simulation with trapped ions

by

Thaned Pruttivarasin

A dissertation submitted in partial satisfaction of the

requirements for the degree of

Doctor of Philosophy

in

Physics

in the

Graduate Division

of the

University of California, Berkeley

Committee in charge:

Professor Hartmut Häffner  
Professor Dan Stamper-Kurn  
Professor Eli Yablonovitch

Spring 2014



## Abstract

Spectroscopy, fundamental symmetry tests and quantum simulation  
with trapped ions

by

Thaned Pruttivarasin

Doctor of Philosophy in Physics

University of California, Berkeley

Professor Hartmut Häffner, Chair

This dissertation reports on precision measurements of the atomic structure of calcium ions ( $^{40}\text{Ca}^+$ ), application of trapped  $^{40}\text{Ca}^+$  ions as a probe for a violation of fundamental symmetry and prospects of performing quantum simulations with trapped ion.

We demonstrate a novel technique to perform spectroscopy on the dipole transition of  $^{40}\text{Ca}^+$  that circumvents usual difficulties from dark resonances and Doppler heating. The center of the atomic transition can be detected to a precision of 200 kHz or less with an integration time of 10 minutes. We apply this method to directly measure the influence of micromotion on the fluorescence spectra and confirm the dependence of the modulation index on the radial trap frequency.

We measure the branching fraction of the excited  $^2\text{P}_{1/2}$  state of  $^{40}\text{Ca}^+$  to be 0.93565(7) using a simple experimental scheme readily applicable to many other ion species. Our result for  $^{40}\text{Ca}^+$  distinguishes well among various theoretically calculated values, which is important in guiding further developments of the theoretical work.

We apply the Ramsey spectroscopy technique based on a pair of correlated ions to probe the effect of the violation of local Lorentz invariance (LLI). The energy difference between the two components of the Bell state  $|\Psi_B\rangle = |m_J = \frac{5}{2}, m_J = -\frac{5}{2}\rangle + |m_J = \frac{1}{2}, m_J = -\frac{1}{2}\rangle$  in the  $D_{5/2}$  manifold of  $^{40}\text{Ca}^+$  is monitored for 12 hours. We found that the energy component related to the violation of LLI varies less than  $17 \pm 22$  mHz. Assuming a hydrogen-like model of  $^{40}\text{Ca}^+$ , the measurement result provides us the bound of the LLI parameter  $C_0^{(2)}$  to be  $1.7 \pm 2.2 \times 10^{-17}$ .

Based on numerical simulations, we show that the Aubry transition in the Frenkel-Kontorova model with trapped ion can be observed for practical experimental parameters such as the strength and wavelength of the optical lattice, which serves as an external perturbing periodic potential. Moreover, we also show that the normal mode structure of ion chain can change significantly as we vary the strength of the optical lattice.

To my mom,  
who made everything possible.

## Acknowledgments

I have always wondered why it takes six years to do a graduate study in physics. Now I know. Life as a graduate student is not easy, and certainly I am grateful to all the support I have received during my six years in Berkeley.

I am greatly indebted to the two most important people in my study and my life here: Hartmut and Mike. I would like to thank my advisor, Hartmut, for giving me an opportunity to do whatever I wanted. Anything I wanted to try, he (almost always) supported it and usually gave me (almost) unlimited money to spend. Six years is a long time and I learnt a great deal of everything from him. Mike is my life saver, a lab partner and a friend I have been so lucky to have. We joined the lab from the beginning and built everything from an empty “lattice” room to what we have today. I am fully aware that I am probably not the easiest person to work with. I would like to thank you two for putting up with me and guiding my path toward something relevant.

I have been surrounded by many great people who have worked in Haeffner Group. The first batch of staffs, Axel, Boyan, Nikos, Soenke and Sankar, have helped me in daily life in the lab since the starting of the project. I greatly enjoyed their company for the past couple of years. I also would like to thank subsequent members of the group (which are too many to list here)—Dylan, Ishan, Mark, Chris and many others—for all the fun things you all shared with me.

The physics department here has been important for my experience here at Berkeley. I would like to thank all AMO people (Dan, Holger, Dima, Ed, Ryan, Zhao, Pei-chan, Shao-yu, Geena, Brian and many others) for sharing their wisdom anytime I had any question (or whenever I just wanted a quick chat or a few imperial optics posts). Also the department staffs (Anne, Donna and especially Joseph) have made my life here 100 times easier.

1721 MLK has been my “home” for four years, and in this home there are three people who I spent my time with outside work everyday: Bier, Jane and Bright. Thank you for all the memorable time we had together. I am also grateful to all the help I received from P Pure, P Gade, P Numrin, Champ, Fook, Oak, Jack and Sali. I also would like to thank Trinuch for everything you have done for me for the past year.

I would like to especially thank Nong Som for providing mental supports and sharing things about cats. Definitely sometimes it feels like I have a personal psychiatrist that I can just seek for help. (Fortunately, I did not need that kind of professional consultant.)

I do not know how my life would have turned out without tremendous support from my family: Mama, P Nick, P Bee and Khun Ar. Thank you for all the love and care. Thank you for everything. Again, I hope I did not let you down. And if somehow you are reading this, I wish you are here to see it, Papa.

# Contents

<b>1</b>	<b>Introduction</b>	<b>1</b>
<b>2</b>	<b>Trapping and cooling of ions</b>	<b>5</b>
2.1	Trapping of charged particles . . . . .	5
2.2	Atomic structure of calcium . . . . .	9
2.2.1	Neutral calcium atoms and calcium ions . . . . .	9
2.2.2	Electric quadrupole shift . . . . .	11
2.2.3	Magnetic sub-levels . . . . .	11
2.3	Interaction of light with a two-level atom . . . . .	12
2.3.1	Rabi oscillation . . . . .	12
2.3.2	Doppler cooling . . . . .	14
<b>3</b>	<b>Lasers and experimental setup</b>	<b>21</b>
3.1	Laser sources . . . . .	21
3.1.1	Diode lasers . . . . .	21
3.1.2	Frequency doubling system (422 nm) . . . . .	23
3.1.3	Narrow linewidth diode laser (729 nm) . . . . .	23
3.1.4	Switching and frequency shifting of lasers . . . . .	28
3.2	Experimental setup . . . . .	28
3.2.1	General structure of the laboratory . . . . .	28
3.2.2	Helical resonator . . . . .	33
3.2.3	Vacuum system and trap construction . . . . .	33
<b>4</b>	<b>Spectroscopy of dipole transitions</b>	<b>37</b>
4.1	Dark resonances and Doppler heating . . . . .	37
4.2	Spectroscopy with a single probe laser . . . . .	38
4.2.1	Time evolution of atomic populations . . . . .	39
4.2.2	Spectroscopy on dipole transitions with fast laser switching . . . . .	41
4.3	Micromotion modulated spectra . . . . .	42
4.3.1	Micromotion spectra at different trap frequencies . . . . .	42
4.3.2	Spectral modulation due to intensity gradient . . . . .	47
<b>5</b>	<b>Measurement of branching fraction</b>	<b>51</b>
5.1	Measurement of branching fractions based on photon counting . . . . .	51
5.1.1	Theoretical considerations for measurement of branching fractions	51

5.1.2	Experimental procedure for measuring the branching fraction . . . . .	53
5.2	Sources of uncertainties . . . . .	55
5.3	Measurement result and discussion . . . . .	58
<b>6</b>	<b>Observation of the Hanle effect with trapped ions</b>	<b>61</b>
6.1	Introduction to the Hanle effect . . . . .	61
6.1.1	Coherence in the excited state . . . . .	62
6.1.2	Optical Bloch equations with all magnetic sub-levels . . . . .	65
6.2	The Hanle effect in trapped calcium ion . . . . .	69
6.2.1	$^2S_{1/2} \rightarrow ^2P_{1/2}$ transition . . . . .	69
6.2.2	$^2D_{3/2} \rightarrow ^2P_{1/2}$ transition . . . . .	71
6.3	Experimental considerations . . . . .	73
<b>7</b>	<b>Spectroscopy with correlated atoms</b>	<b>75</b>
7.1	Introduction . . . . .	75
7.2	Spectroscopy with correlated ions . . . . .	77
7.2.1	State preparation . . . . .	78
7.2.2	State readout . . . . .	79
7.2.3	Detection of the parity oscillation signal . . . . .	82
7.2.4	Correlated ions with additional sympathetically cooling ions .	84
7.3	Measurement of magnetic field gradient . . . . .	84
7.4	Test of local Lorentz invariance using correlated ions . . . . .	86
7.4.1	Energy shift due to the violation of LLI in $^{40}\text{Ca}^+$ . . . . .	86
7.4.2	Experimental procedure . . . . .	87
7.4.3	Experimental result . . . . .	91
<b>8</b>	<b>Quantum simulation of the Frenkel-Kontorova model</b>	<b>97</b>
8.1	The Frenkel-Kontorova model . . . . .	97
8.2	Numerical simulation of the Frenkel-Kontorova model with trapped ions	102
8.3	Using trapped ions to study nano-scale friction . . . . .	106
8.4	Experimental progress toward realizing the FK model with trapped ions.	108
<b>9</b>	<b>Summary and outlook</b>	<b>113</b>
<b>Bibliography</b>		<b>117</b>
<b>A</b>	<b>Matrix elements between magnetic sub-levels</b>	<b>125</b>
A.1	Geometry . . . . .	125
A.2	General form of the matrix elements . . . . .	125
A.2.1	$J = 1/2 \rightarrow J = 1/2$ . . . . .	126
A.2.2	$J = 3/2 \rightarrow J = 1/2$ . . . . .	127
<b>B</b>	<b>AtomicDensityMatrix package for Mathematica<sup>®</sup></b>	<b>129</b>

<b>C Electronics and experiment controls</b>	<b>131</b>
C.1 Pulse sequencer and direct digital synthesizer (DDS) . . . . .	131
C.1.1 Pulser . . . . .	133
C.1.2 Direct digital synthesizer (DDS) . . . . .	135
C.1.3 Using the Pulser . . . . .	136
C.2 DC voltage control using digital-to-analog converter (DAC) . . . . .	141



# List of Figures

2-1	Dynamical trapping of a charged particle.	6
2-2	Radio-frequency electrodes and endcaps in a Paul trap.	7
2-3	Atomic structure of neutral calcium atoms.	9
2-4	Atomic structure of singly ionized calcium ions ( $^{40}\text{Ca}^+$ ).	10
2-5	Simple picture of Doppler cooling.	15
2-6	Crystal of 37 ions under Doppler cooling.	18
3-1	Frequency doubling cavity for generation of 422 nm light.	24
3-2	Bow-tie cavity currently used in our experiment.	24
3-3	Cavity ring-down signal for the high finesse cavity.	25
3-4	High finesse stable cavity for the 729 nm laser light. The picture is taken from [43].	26
3-5	Setup for the high finesse cavity for the 729 nm laser light.	26
3-6	Setting of the locking parameters for the 729 nm diode laser using a FALC module.	27
3-7	Beat signals between laser light shifted by 220 MHz using an AOM and the unshifted light.	28
3-8	Beam paths for 729 nm and ions imaging.	29
3-9	A modification to a standard double pass AOM setup.	29
3-10	Layout of the laboratory.	30
3-11	Cavity center frequency as a function of time.	32
3-12	Short-term drift of the center frequency of the high finesse cavity.	33
3-13	The half-wave resonator used to generate voltages out-of-phase from each other on the two ends of the resonator.	34
3-14	Vacuum setup for the experiment.	35
3-15	The Paul trap used in our experiment.	36
4-1	Typical lambda-level structure for an atom with a simple valence electron and a low lying D-state.	38
4-2	Typical averaged fluorescence dynamics collected for $\sim 10^6$ measurement cycles.	40
4-3	The fluorescence spectrum of the $^2\text{S}_{1/2} \rightarrow ^2\text{P}_{1/2}$ transition for $^{40}\text{Ca}^+$ .	42
4-4	Micromotion modulated fluorescence spectra of the $\text{S}_{1/2} \rightarrow \text{P}_{1/2}$ transition.	44
4-5	Micromotion modulated fluorescence spectra of the $\text{D}_{3/2} \rightarrow \text{P}_{1/2}$ transition.	45

4-6	Relationship between the two radial trap frequencies, $f_x$ and $f_y$ . . . . .	46
4-7	Micromotion modulation index, $\beta$ , measured as a function of trap frequency, $f_x$ . . . . .	47
4-8	Effect of laser light intensity gradient, $\beta'$ , on the simulated fluorescence spectra with $\beta = 0$ . . . . .	49
4-9	Effect of laser light intensity gradient, $\beta'$ , on the simulated fluorescence spectra with $\beta = 1.0$ . . . . .	50
5-1	Pulse sequence for measuring the branching fraction. . . . .	54
5-2	Branching fraction $p$ measured for different magnetic field strength and orientation. . . . .	56
5-3	Measurement of the branching fraction compared to various theoretical calculations in the literature. . . . .	58
5-4	Energy diagram involving the excited $^2P_{3/2}$ state which has three decay channels. . . . .	59
6-1	Condition for creating coherence in the excited states. . . . .	62
6-2	Typical experimental setup to observe the Hanle effect. . . . .	63
6-3	Typical Hanle signal. . . . .	64
6-4	Diagram of the parameters of the 8-level Bloch equations. . . . .	65
6-5	The Hanle effect for $^2S_{1/2} \rightarrow ^2P_{1/2}$ excitation. . . . .	70
6-6	The Hanle effect for $^2D_{3/2} \rightarrow ^2P_{1/2}$ excitation. . . . .	72
6-7	Sharp resonances at low magnetic field strength for the narrowband excitation. . . . .	72
7-1	Bell state created from different Zeeman levels of the D-state of two ions.	77
7-2	Parity oscillations of the two ions with $ \Psi_B\rangle = \frac{1}{\sqrt{2}}( SD\rangle +  DS\rangle)$ . . .	80
7-3	Parity oscillations of the two ions with $ \Psi_B\rangle = \frac{1}{2}( D; m_J = -\frac{1}{2}\rangle +  D; m_J = \frac{1}{2}\rangle)$ . . . . .	81
7-4	Histogram of the readout for two ions. . . . .	83
7-5	Four-ion configuration. . . . .	84
7-6	Effect of sympathetic cooling on the parity signal. . . . .	85
7-7	Electric quadrupole shift as a function of applied electric field gradient.	88
7-8	Phase jump due to an instantaneous change in the magnetic field gradient. . . . .	89
7-9	Effects of the phase shift and offset shift. . . . .	90
7-10	Variation in the magnetic field observed for 12 hours. . . . .	92
7-11	Variation in the axial trap frequency observed for 12 hours. . . . .	93
7-12	Variation in the frequency of the quadrupole shift of the ions observed for 12 hours. . . . .	94
7-13	Allan deviation of the frequency calculated from the phase data shown in Fig. 7-12. . . . .	95
8-1	The Frenkel-Kontorova model. . . . .	98
8-2	Left: system with a very weak external potential. Right: system with a very strong external potential. . . . .	98

8-3	Maps generated using Eq. (8.3) for different values of $\kappa$ . . . . .	100
8-4	The hull function of the incommensurate FK model in different phases. The figure is taken from [91]. . . . .	101
8-5	Linear chain of ion in an optical lattice created by a standing wave formed by an optical cavity. . . . .	103
8-6	Effect of an optical lattice at 405 nm on the ion chain. . . . .	104
8-7	The effect of the optical lattice on the mode structure of the ion chain. .	106
8-8	Dynamics of the last ion in a chain with different optical lattice power when the first ion is kicked. . . . .	107
8-9	Center-of-mass position of the chain as a function of the axial tilting of the trap ( $\gamma$ ) for different optical lattice powers. . . . .	107
8-10	Our current trap with an optical cavity for the realization of the FK model. . . . .	109
8-11	Mechanism to align the optical lattice with the trap in-vacuum. . . . .	110
A-1	Coordinate of the direction of light propagation $\hat{n}$ . The angle $\alpha$ mea- sure the polarization of the light with respect to the vertical direction. .	126
C-1	Hardware wiring configuration for the Pulser. . . . .	132
C-2	The Pulse break-out board and two DDS boards under testing. . . . .	132
C-3	Sample pulse sequence. . . . .	133
C-4	Block diagram of the DDS board. . . . .	137
C-5	Filtering of DC voltages. . . . .	141



# List of Tables

2.1	The values of $g_J$ for different levels of $^{40}\text{Ca}^+$ . . . . .	12
3.1	Laser light wavelengths required to perform experiments. . . . .	22
3.2	Laser light frequencies measured by the wave-meter for trapping of $^{40}\text{Ca}^+$ . . . . .	31
5.1	List of measurement uncertainties for the branching fraction of $^{40}\text{Ca}^+$ . . . . .	57
7.1	Energy shifts due to magnetic field gradient for each possible combination of the state $ \Psi_B\rangle =  1/2, -1/2\rangle +  5/2, -5/2\rangle$ . . . . .	86

# Chapter 1

## Introduction

Driven by the prospect of quantum computing, the field of trapped ions has been undergoing a rapid technological development in the past two decades. Quantum coherence in trapped ions has been engineered such that it is tremendously immune to external disturbance. Combined with our mastery in manipulating the quantum state of the ions by means of laser light, experimentalists have been able to realize many quantum computation algorithms with trapped ions in recent years [1, 2, 3]. Many leading experimental physics groups in the world are working toward realizing more complicated protocols and scaling up quantum networks based on trapped ions [4].

Outside the context of quantum computing, progress in using trapped ions in precision measurements is also immense. One of the most promising candidates for the next generation atomic clocks is realized using trapped  $\text{Hg}^+$  and  $\text{Al}^+$  [5, 6]. Moreover, by engineering the quantum states of the ions, we can use ions as a sensitive probe of external fields such as the strength of the magnetic field and the electric field gradient [7]. Some of heavier ion species can be used as a probe of exotic effects such as the parity non-conservation or the time-variation of the fine structure constant [8]. Beyond trapping of atomic ions, ion trapping techniques are recently applied to performing spectroscopy of molecules [9]. These experimental tools help propel our understanding of not only the complex atomic or molecular structures, but also many fundamental physical phenomena such as the effect of gravity on the atomic energy levels [10].

Another exciting emerging field is quantum simulation with trapped ions. The idea of using a well-controlled quantum system to simulate Hamiltonians has been proposed many years ago by Richard Feynman [11]. At the beginning, most of the experiments related to quantum simulations were performed with neutral atoms trapped in optical lattices. The realization of the Mott insulator is perhaps one of the most well-known experimental work in the past decade [12]. Trapped ions have a slower start mainly because the number of particles trapped is rather small compared to typical neutral atom traps. However, there have been many proposals in using trapped ions as a test-bed for quantum simulations [13, 14, 15]. Experimental works in this direction have also been undergoing rapid development [16, 17, 18, 19, 20].

The story of ion trapping experiments at Berkeley, especially the so-called “lattice”

project, started roughly five years ago with the goal of using a linear chain of trapped ions in an optical lattice to perform a quantum simulation of the Frenkel-Kontorova model [21]. However, the experimental setup did not work the way we envisioned. The optical cavity that we put in the vacuum system was likely to become misaligned during the bake-out. It is not clear what caused this problem since the cavity worked well before in a separated test vacuum chamber. In any case, the realization of the original intended work is still something we look forward to in the future.

Despite the mishap in the experimental setup, we did not get discouraged and looked for interesting physics to explore with the setup that we have. Fortunately, the robustness of trapped ions allows us to explore many aspects of physics we did not even think about at the beginning of this project. There are two main categories of the experiment that the lattice project gave birth to for the past 5 years. The first category is related to the study of open quantum systems and the thermal behavior of the ion chain. The work includes local detection of quantum correlation in trapped ions [22] and energy transport in a chain of up to 37 ions [23]. This part is covered extensively in Michael Ramm's thesis.

The second category of our experiments is related to precision spectroscopy using trapped ions. This is the main part of this thesis. The outline is given in the following:

We begin in **Chapter 2** by reviewing the physics of trapping and cooling of ions. The atomic structure of  $^{40}\text{Ca}^+$  is presented along with the analysis of the corresponding atom-light interaction. This leads to the technique of Doppler cooling and sideband cooling which are essential in controlling the quantum state of  $^{40}\text{Ca}^+$ . **Chapter 3** describes the experimental setup that we use with an emphasis on the laser systems. The trap construction and the layout of the vacuum chamber are described in details in Michael Ramm's thesis.

In **Chapter 4**, we demonstrate a novel experimental scheme to perform spectroscopy of dipole transitions in trapped ions. We show how the usual problems of Doppler heating and dark resonances can be circumvented by rapidly alternating between the spectroscopy and the repumper laser light. Then we apply this method to directly measure the modulation index of the fluorescence spectrum caused by the so-called micromotion. We observe for the first time the dependence of the modulation index on the trap frequency. The main result of this chapter is reported in Ref. [24].

**Chapter 5** contains our work on a precision measurement of the branching fractions of the excited  $^2\text{P}_{1/2}$  state of  $^{40}\text{Ca}^+$ . The experimental scheme is based on fast photon counting during population transfers of the ions between the ground state and the metastable D-state. The precision of our measurement is enough to clearly distinguish among different theoretical values. This simple experimental method is applicable to many ion species used in modern ion trapping experiments. The main result of this chapter is reported in Ref. [25].

The prospect of precisely measuring the lifetime of the excited  $^2\text{P}_{1/2}$  state of  $^{40}\text{Ca}^+$  using the Hanle effect is the main topic of **Chapter 6**. This is motivated by the discrepancy between the value measured in 1993 by Jin *et al.* [26] and recently calculated value in 2011 by Safronova *et al.* [27]. In this chapter, we describe the physics and theoretical considerations of many possible experimental schemes to measure the lifetime via the Hanle effect in trapped  $^{40}\text{Ca}^+$ . We analyze some of the potential sys-

tematic uncertainties and the expected precision of the measurement based on this method.

In **Chapter 7**, we demonstrate a technique of using correlated ions to as a probe for various external fields. We describe the experimental scheme and measure the magnetic field gradient and the electric field gradient using a pair of trapped  $^{40}\text{Ca}^+$ . We then apply this technique to probe possible small changes in the atomic transition energy due to the violation of Local Lorentz Invariance (LLI). We report the preliminary experimental bound of the violation.

In **Chapter 8**, we investigate the prospect of using trapped ions to realize the Frenkel-Kontorova model in conjunction with an optical lattice. We report on numerical simulations that show the feasibility of the experiment using practical experimental parameters. The main result of this chapter is reported in Ref. [28].

In **Chapter 9**, we summarize the work and discuss potential improvements and some of the future plans for the experiment.



# Chapter 2

## Trapping and cooling of ions

Due to strong interactions between charged particles (ions) and electromagnetic fields, we can tightly confine charged particles with either oscillating electric fields (the Paul trap) or a combination of static electric and magnetic field (the Penning trap). Both mechanisms provide trapping depths on the order of 1 eV and oscillation frequencies of more than 1 MHz. This is many times stronger than that of neutral atoms in magneto-optical traps (MOT) or dipole traps. Strong confinement allows us to perform Doppler cooling of trapped ions efficiently, which is crucial in using trapped ions to perform various precision measurements described in the subsequent chapters. In this chapter we describes the most important building blocks of experiments with trapped ions: the Paul trap and laser cooling.

### 2.1 Trapping of charged particles

Since trapping of a charged particle using only static electric fields is prohibited by the Maxwell's equations, the idea of using oscillating electric fields to dynamically trap ions was pioneered by Wolfgang Paul back in 1953 (see his Nobel lecture at [29]). At any instant of time, the ion experiences a saddle point quadrupole potential generated by a set of electrodes, as shown in Fig. 2-1. The fast driving field effectively shakes the ion back and forth, resulting in an induced “motional” dipole moment of the particle. This induced dipole moment is then pulled toward the saddle point (the radio-frequency (RF) null) which has the lowest electric field gradient.

To mathematically describe the motion of trapped particles, we consider a geometry of electrodes given in Fig. 2-2 and follow an analysis given in [31, 32]. The applied potentials  $V_0$  on the two pairs of electrodes oscillate out of phase with each other at a frequency  $\Omega_D$ . The potential near the trap center is given by

$$\Phi(x, y, t) = V_0 \sin(\Omega_D t) \frac{x^2 - y^2}{R^2}, \quad (2.1)$$

where  $x$  and  $y$  are positions along each pair of electrodes, and  $R$  is a characteristic length depending on the distance between electrodes.

Additionally, we also apply a static potential to the endcaps (as shown in Fig.

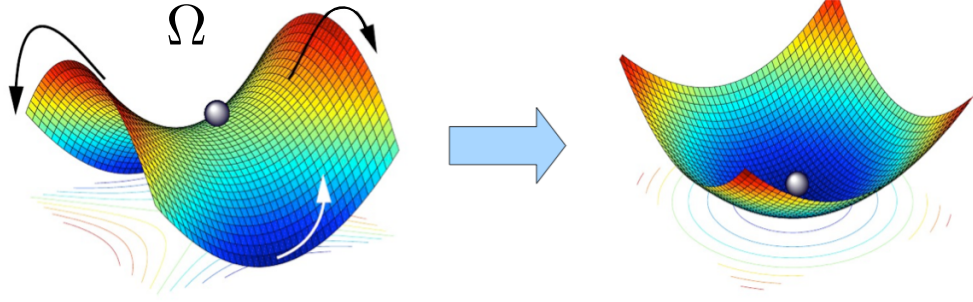


Figure 2-1: Dynamical trapping of a charged particle. A saddle point potential is oscillating with a frequency  $\Omega_D$ , resulting in an effective trapping in all directions. This diagram is adapted from [30].

2-2) to provide a confinement in the  $z$  direction (along the trap axis). This is given by

$$U(x, y, z) = \frac{\kappa U_0}{Z_0^2} \left( z^2 - \frac{x^2 + y^2}{2} \right), \quad (2.2)$$

where  $U_0$  is the potential applied to the endcaps,  $\kappa$  is a geometrical constant, and  $Z_0$  is a characteristic length depending on the distance between the endcaps.

We analyze the motion of the ions by first calculating the electric field near the trap center. This is given by

$$\vec{E} = -\vec{\nabla}(\Phi + U) \quad (2.3)$$

$$= -2V_0 \frac{x\hat{x} - y\hat{y}}{R^2} \sin(\Omega_D t) - \frac{\kappa U_0}{Z_0^2} (2z\hat{z} - x\hat{x} - y\hat{y}). \quad (2.4)$$

The equations of motion can then be written in the following form:

$$\ddot{u}_i + (a_i + 2q_i \sin(\Omega_D t)) \frac{\Omega_D^2}{4} u_i = 0, \quad (2.5)$$

where  $u_i$  is a displacement from the trap center along the  $\hat{i}$  direction, and we introduced the dimensionless variables

$$a_x = a_y = -\frac{1}{2}a_z = -\frac{4Q\kappa U_0}{mZ_0^2\Omega_D^2} \quad (2.6)$$

$$q_x = -q_y = \frac{4QV_0}{mR^2\Omega_D^2} \quad (2.7)$$

$$q_z = 0, \quad (2.8)$$

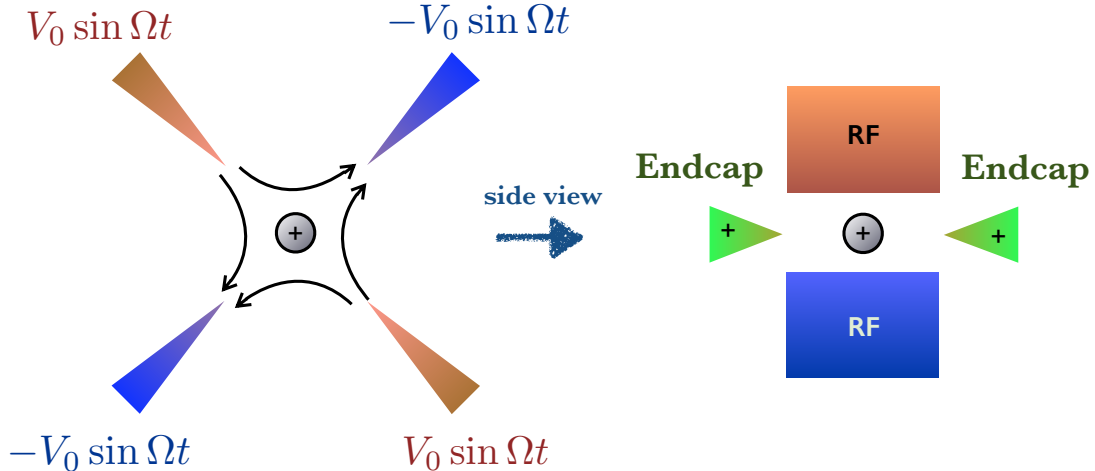


Figure 2-2: Radio-frequency electrodes and endcaps in a Paul trap.

and  $Q/m$  is a charge-to-mass ratio of the ion.

The form of equations given in Eq. (2.5) is called the Mathieu equation which is a very important class of equations related to many fields in physics. A general solution to the Mathieu equation is complicated, but in our case, we only need to look at the lowest order solution.

If we look closely at Eq. (2.5), we can see that the motion of the charged particle should have two distinct time scales: a fast motion oscillating at  $\Omega_D$  and a slower one that depends on the electric field gradient. We call the fast motion to be the “micromotion” and the slower motion to be the “secular” motion. We write the displacement as

$$u_i = \mu_i + s_i, \quad (2.9)$$

where  $\mu$  and  $s$  are displacements corresponding to the micromotion and secular motion, respectively. Substituting into Eq. (2.5) yields

$$\ddot{\mu}_i + \ddot{s}_i + (a_i + 2q_i \sin(\Omega_D t)) \frac{\Omega_D^2}{4} (\mu_i + s_i) = 0. \quad (2.10)$$

We assume that  $\ddot{\mu}_i \gg \ddot{s}_i$  and  $s_i \gg \mu_i$ . The equation of motion becomes

$$\ddot{\mu}_i + (a_i + 2q_i \sin(\Omega_D t)) \frac{\Omega_D^2}{4} s_i = 0. \quad (2.11)$$

We then use a fact that the micromotion oscillates with  $\Omega_D$  and obtain

$$\begin{aligned} -\Omega_D^2 \mu_i + (a_i + 2q_i \sin(\Omega_D t)) \frac{\Omega_D^2}{4} s_i &= 0 \\ \frac{a_i + 2q_i \sin(\Omega_D t)}{4} s_i &= \mu_i. \end{aligned} \quad (2.12)$$

Substituting  $\mu_i$  from the last expression into Eq. (2.10) gives

$$\ddot{s}_i = -(a_i + 2q_i \sin(\Omega_D t))^2 \frac{\Omega_D^2}{16} s_i. \quad (2.13)$$

After averaging over the period of the micromotion, the equation of motion for the secular motion is given by

$$\ddot{s}_i = -(a_i^2 + 2q_i^2) \frac{\Omega_D^2}{16} s_i, \quad (2.14)$$

which indicates that the secular motion is, to the first order, harmonic with a frequency of

$$\omega_i = \frac{\Omega_D}{4} \sqrt{a_i^2 + 2q_i^2}. \quad (2.15)$$

The motion of the charged particle is a combination of the micromotion and secular motion:

$$\begin{aligned} u_i &= \mu_i + s_i \\ &= u_{0i} \cos(\omega_i t + \delta_i) \left( 1 + \frac{a_i}{4} + \frac{q_i}{2} \sin(\Omega_D t) \right) \\ &\approx u_{0i} \cos(\omega_i t + \delta_i) \left( 1 + \frac{q_i}{2} \sin(\Omega_D t) \right), \end{aligned} \quad (2.16)$$

where  $u_{0i}$  is the amplitude of the secular motion and we use the fact that typically  $a_i \ll 1$  in the last step.

An important remark that we want to keep in mind is that the micromotion is intrinsically not a harmonic oscillator. It is a driven motion caused by the oscillating potential on the trap electrodes. The secular motion, on the other hand, behaves very much like an ideal harmonic oscillator. This is true in experiments where the amplitude of the secular motion is small, which is well justified for Doppler cooled ions in a typical Paul trap.

Another observation related to the experimental setup is the dependence of the secular trap frequency  $\omega_i$  on the drive frequency  $\Omega_D$  and amplitude  $V_0$ . From Eq. (2.6-2.8) and (2.15), we can see that, for a small end cap potential ( $U_0 \sim 0$ ), we have  $\omega_i \propto V_0/\Omega_D$ . This relation might give an impression that we should keep the drive frequency low to have higher trap frequency. While this statement is true, experimentally we have a rule of thumb that the highest trap frequency we can achieve by increasing the amplitude  $V_0$  of the RF drive for a given  $\Omega_D$  is roughly  $\Omega_D/10$ .

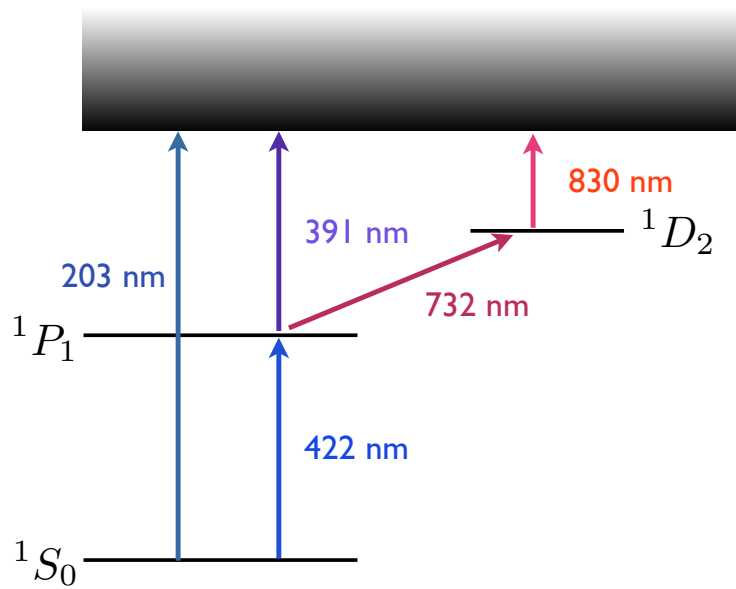


Figure 2-3: Atomic structure of neutral calcium atoms.

Pushing the trap frequency beyond this will make the trap unstable. This means that, for example, getting a trap frequency of 3 MHz requires the drive frequency to be at least 30 MHz.

## 2.2 Atomic structure of calcium

The trapping mechanism described in the previous section works with any kind of charged particle regardless of its internal structure. However, in our experiment, the charge particles are in fact ionized calcium atoms which have an internal structure. In this section we describe the atomic structure of calcium atoms and ions, which is essential in understanding of Doppler cooling and quantum state manipulations of  $^{40}\text{Ca}^+$ ions.

### 2.2.1 Neutral calcium atoms and calcium ions

The first step in our experiments is to create calcium ions from vapor of neutral calcium atoms. Calcium bought from suppliers comes in the form of small metallic grains. In the experiment, we produce a gaseous beam of calcium by heating up these small grains and use laser light to photo-ionize them. We produce calcium ions by essentially removing one electron from each calcium atom.

A calcium atom has two valence electrons, and the atomic structure is given in Fig. 2-3 with each state notated by the term symbol  $^{2s+1}L_J$ . We can see that there

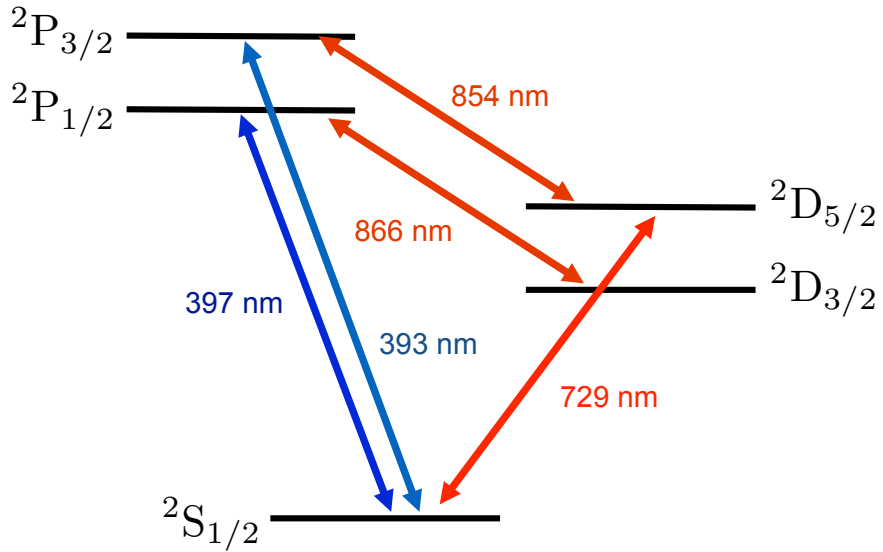


Figure 2-4: Atomic structure of singly ionized calcium ions ( $^{40}\text{Ca}^+$ ).

are at least three ways to ionize a calcium atom: a direct 203 nm path, a two-step 422+391 nm path and a three-step 422+732+830 nm path. We use a two-step 422+391 nm path for photo-ionization since it requires only two laser beams which are conveniently available.<sup>1</sup> This photo-ionization path is also more efficient than the three-photon path.

The reason why calcium and other elements with two valence electrons are ideal for trapped ion experiments is because there is only one valence electron after a process of photo-ionization. The atomic structure is then approximately similar to that of hydrogen atoms.

There are two calcium isotopes used in modern trapped ion experiments:  $^{40}\text{Ca}^+$  and  $^{43}\text{Ca}^+$ . In our experiment, we use only  $^{40}\text{Ca}^+$  which has no hyperfine structure. The atomic structure of  $^{40}\text{Ca}^+$  is relatively simple, as shown in Fig. 2-4. The 397 nm and 866 nm transitions are used for Doppler cooling. The 729 nm transition is a quadrupole transition with a lifetime of about 1 second [33]. We use this  $^2\text{S}_{1/2} \rightarrow ^2\text{D}_{5/2}$  transition as a qubit. The 854 nm transition is for depopulating the  $\text{D}_{5/2}$  level and broadening of the quadrupole transition, which is important in performing sideband cooling.

---

<sup>1</sup>We produced the first ions in our trap using the three-step photo-ionization scheme. However, it was difficult to find the transition frequency of the 732 nm laser light so we switched to the two-step scheme.

## 2.2.2 Electric quadrupole shift

The valence electron for different  $m_J$  states interacts differently with the external electric field gradient. Since ions in a Paul trap are trapped using static potentials in the axial direction, there is always an electric field gradient along the axial direction  $\hat{z}$ . The energy shift from the interaction between the atomic quadrupole moment and the electric field gradient for the  $D_{5/2}$  states is given by [34, 35]:

$$\Delta E_{\text{quad}} = \hbar\omega_{\text{quad}} = \frac{1}{4} \frac{m\omega_{\text{axial}}^2}{e} |Q| A \times \begin{cases} -1 & \text{if } m_J = \pm \frac{5}{2} \\ \frac{1}{5} & \text{if } m_J = \pm \frac{3}{2}, \\ \frac{4}{5} & \text{if } m_J = \pm \frac{1}{2} \end{cases} \quad (2.17)$$

where  $m$  is the mass of the ion,  $\omega_{\text{axial}}$  is the axial trap frequency,  $A$  is a geometric factor depending on the asymmetry of the electric field gradient and the direction of the quantization axis, and  $|Q| \sim 1.9ea_0^2$  is a quadrupole moment of  $D_{5/2}$  state of  $^{40}\text{Ca}^+$  [7].

## 2.2.3 Magnetic sub-levels

With a static magnetic field  $\vec{B}$  applied to the ions, each state splits into smaller Zeeman sub-levels according to its magnetic quantum number. The linear energy splitting is given by

$$\Delta E_{\text{Zeeman}}^{(1)} = g_J \mu_B m_J |\vec{B}|, \quad (2.18)$$

where  $\mu_B$  is Bohr's magneton,  $m_J$  is the magnetic quantum number and the Landé  $g_J$  factor given by

$$g_J = 1 + \frac{J(J+1) + S(S+1) - L(L+1)}{2J(J+1)}. \quad (2.19)$$

Table 2.1 summarizes the value of  $g_J$  for each state of  $^{40}\text{Ca}^+$ . We always apply a magnetic field of about 3-4 G in our setup. This gives the Zeeman splitting on the order of 2-3 MHz.

There are also energy shifts which are quadratic in the magnitude of the magnetic field. In the low field limit, these can be calculated using the second-order perturbation theory. This quadratic Zeeman shift is given by [34]

$$\Delta E_{\text{Zeeman}}^{(2)} = K \frac{(\mu_B |\vec{B}|)^2}{hf_{\text{FS}}}, \quad (2.20)$$

where  $K = 6/25, 4/25$  and  $0$  for  $m_J = \pm 1/2, \pm 3/2$  and  $\pm 5/2$ , respectively, and  $f_{\text{FS}}$  is the frequency of the corresponding fine-structure energy level. For the D levels of  $^{40}\text{Ca}^+$ ,  $f_{\text{FS}} = 1.8$  THz.

State	$g_J$
$^2S_{1/2}$	2
$^2P_{1/2}$	2/3
$^2P_{3/2}$	4/3
$^2D_{3/2}$	4/5
$^2D_{5/2}$	6/5

Table 2.1: The values of  $g_J$  for different levels of  $^{40}\text{Ca}^+$

## 2.3 Interaction of light with a two-level atom

Once we have understood the atomic structure of  $^{40}\text{Ca}^+$ , we want to control and manipulate the quantum state of calcium ions. For this we use laser light. To the lowest order, we can describe the ion as an ideal two-level system interacting with a monochromatic driving laser field, resulting in the Rabi oscillations of atomic states. Next we add decoherence due to a spontaneous decay of the excited state, which is important in Doppler cooling.

### 2.3.1 Rabi oscillation

We consider an ion with two levels: the ground state  $|g\rangle$  and the excited state  $|e\rangle$ . We first ignore the motional degree-of-freedom of the ion and analyze the atomic population transfer from interaction with laser light. Many standard textbooks such as [36] have detailed analysis on Rabi oscillations. Here we only highlight the most important results.

#### 2.3.1.1 Static ion

First we consider the ion as static by ignoring the momentum transfer of the laser light onto the ion. We approximate the electric field of the laser light interacting with the ion as a plane wave:

$$\vec{E}(\vec{r}, t) = \vec{E}_0 e^{i(\vec{k} \cdot \vec{r} - \omega_{\text{laser}} t + \phi)}, \quad (2.21)$$

where  $\vec{r}$  is the vector position of the atom,  $\vec{k}$  is the wave-vector of the laser light and  $\phi$  is the phase of the laser light. We assume that the ion is a point-like particle located at  $\vec{r} = 0$ . We introduce the detuning  $\delta = \omega_0 - \omega_{\text{laser}}$  where  $\omega_0$  is the frequency of the atomic transition. In the interaction picture, the light-ion interaction Hamiltonian is given by

$$H = \begin{pmatrix} -\hbar\delta & \frac{\hbar\Omega_R}{2} e^{i\phi} \\ \frac{\hbar\Omega_R}{2} e^{-i\phi} & 0 \end{pmatrix}, \quad (2.22)$$

where  $\Omega_R$  is the Rabi frequency associated with the laser light intensity.

Let us consider the frequency of the laser light to be on resonance ( $\delta = 0$ ). The time evolution of any initial state

$$|\Psi(t=0)\rangle = a|e\rangle + b|g\rangle = \begin{pmatrix} a \\ b \end{pmatrix} \quad (2.23)$$

is given by

$$|\Psi(t)\rangle = e^{-iHt} |\Psi(t=0)\rangle = \begin{pmatrix} \cos(\frac{\theta}{2}) & i\sin(\frac{\theta}{2})e^{i\phi} \\ i\sin(\frac{\theta}{2})e^{-i\phi} & \cos(\frac{\theta}{2}) \end{pmatrix} \begin{pmatrix} a \\ b \end{pmatrix}, \quad (2.24)$$

where  $\theta = -\Omega_R t$  and we set  $\hbar = 1$ . Suppose that  $\phi = 0$  and initially the ion is in the ground state, the time evolution of the populations is given by

$$|\Psi(t)\rangle = i\sin\left(\frac{\theta}{2}\right)|e\rangle + \cos\left(\frac{\theta}{2}\right)|g\rangle = \begin{pmatrix} i\sin\left(\frac{\theta}{2}\right) \\ \cos\left(\frac{\theta}{2}\right) \end{pmatrix}. \quad (2.25)$$

This shows that the atomic population oscillates sinusoidally between  $|g\rangle$  and  $|e\rangle$ . The probability of finding the ion in the ground state is given by

$$P_g(t) = \cos^2\left(\frac{\theta}{2}\right) = \cos^2\left(\frac{\Omega_R t}{2}\right). \quad (2.26)$$

We use the term  $\pi$ -pulse to indicate an interaction duration such that  $\theta = \pi$ . This means if the initial atomic population is in the ground state, after an application of a  $\pi$ -pulse, all the atomic population is transferred to the excited state. A  $\pi/2$ -pulse is used to indicate an interaction duration such that  $\theta = \pi/2$ . If the initial atomic population is in the ground state, after an application of a  $\pi/2$ -pulse, we create a super-position state  $|\Psi\rangle = i|e\rangle + |g\rangle$ .

### 2.3.1.2 Trapped ion

We now include the motional degree of freedom of the ion. Since the ion motion is approximately harmonic with a frequency of  $\omega$  in a Paul trap, we also label its motional state using  $|n\rangle$ , where  $n$  is the vibrational quantum number. The Hamiltonian of the light-ion interaction is given by [37, 38]

$$H = -\hbar\delta|e\rangle\langle e| + \hbar\omega\left(a^\dagger a + \frac{1}{2}\right) + \frac{\hbar\Omega_R}{2}(\sigma^+e^{-ikx} + \sigma^-e^{ikx}), \quad (2.27)$$

where  $\sigma^\pm$  is the atomic raising and lowering operator of the electronic states and  $a$  is the lowering operator for the ion motion. The term  $kx$  is usually written out using the Lamb-Dicke parameter  $\eta = k\sqrt{\hbar/2m\omega}$  as  $kx = \eta(a + a^\dagger)$ . Usually we work in a Lamb-Dicke regime where  $\eta \ll 1$ .

For  $\delta = 0$ , similar to the case where we ignored the ion motion, the atomic population oscillates back and forth between  $|g\rangle$  and  $|e\rangle$ . However, the motion of the ion in the trap results in a modulation of the spatial overlap between the ion and

the light. Thus the effective Rabi frequency between  $|g\rangle$  and  $|e\rangle$  also depends on the motional amplitude of the ion. The Rabi oscillation frequency between each pair of  $|n, g\rangle$  and  $|n, e\rangle$  is given by [39]

$$\Omega_{Rn} = \Omega_R(1 - \eta^2 n). \quad (2.28)$$

If the probability distribution of the vibrational quantum number is given by  $p(n)$ , then Eq. (2.26) is replaced by

$$P_g(t) = \sum_{n=0}^{\infty} p(n) \cos^2 \left( \frac{\Omega_R(1 - \eta^2 n)t}{2} \right), \quad (2.29)$$

meaning that the contrast of the Rabi oscillations may decrease due to the averaging of many different Rabi frequencies from different motional states.

### 2.3.2 Doppler cooling

In reality Rabi oscillations cannot persist forever due to a possibility of spontaneous decay from the excited state  $|e\rangle$  back to the ground state  $|g\rangle$ . The incoherent process is dominant when the decay rate is comparable to or larger than the Rabi frequency. Experimentally we rely on this fast spontaneous decay to quickly reduce kinetic energy of the ions by means of light scattering. This so-called Doppler cooling generally brings the temperature of the ion low enough to be in a Lamb-Dicke regime ( $\eta^2 n \ll 1$ ) within a few milli-seconds.

#### 2.3.2.1 Intuitive picture of Doppler cooling

Doppler cooling relies on the Doppler effect, which is a shift in the observed frequency of the laser light due to the motion of the observer. Consider an ion moving back and forth in a harmonic trap. If the laser frequency is red-detuned from the atomic transition, the ion will be more likely to absorb photons when moving towards the laser light, as shown in Fig. 2-5. The momentum of the photon imparted on the ion upon absorptions then reduces the magnitude of the momentum of the ion. The kinetic energy is then reduced. We achieve the highest cooling efficiency when the imbalance of the photon absorption rate between the ion moving away from the laser light and toward the laser light is maximized. If the linewidth (or the decay rate) of the atomic transition is given by  $\gamma$ , this is achieved by having the laser frequency at  $\delta \sim -\gamma/2$ .

However, after any absorption of a photon, an ion must emit a photon out due to spontaneous emissions. Assume that the ion is not polarized, the emission pattern is isotropic in the low laser light intensity limit. This random emission process is a heating mechanism which we cannot avoid. Balancing the cooling process due to photon absorptions and the heating process due to random emissions yields an ion energy (or temperature) in steady state. This so-called Doppler temperature is

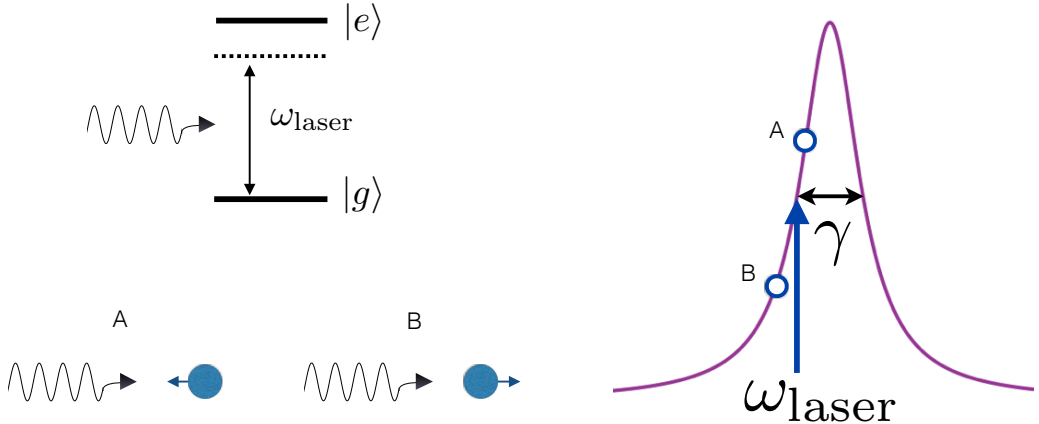


Figure 2-5: Simple picture of Doppler cooling. A laser light red-detuned from the atomic transition makes the ion more likely to absorb photons with moving toward the laser light (scenario A) compared to the ion moving away from the laser light (scenario B). Hence, on average, the momentum of the ion is reduced.

approximately given by [32]

$$T_d \approx \frac{\gamma \hbar}{2k_B}. \quad (2.30)$$

### 2.3.2.2 The master equations

A standard way to mathematically incorporate spontaneous emission is to use the quantum Liouville equation [38]:

$$\frac{d}{dt}\rho = -\frac{i}{\hbar}[H, \rho] + \mathcal{L}\rho, \quad (2.31)$$

where  $\mathcal{L}$  is the Lindblad operator. The form of  $\mathcal{L}$  is given by

$$\mathcal{L}\rho = \frac{\gamma}{2}(2\sigma^-\tilde{\rho}\sigma^+ - \sigma^+\sigma^-\rho - \rho\sigma^+\sigma^-), \quad (2.32)$$

where  $\gamma$  is the decay rate of the excited state and  $\tilde{\rho}$  is the density matrix after a spontaneous emission:

$$\tilde{\rho} = \int_{-1}^1 du N(u) e^{ikux} \rho e^{-ikux}. \quad (2.33)$$

$N(u)$  is a geometrical factor corresponds to the pattern of spontaneous emissions.

At the low saturation limit, the population of the excited state can be ignored along with the coherence between the electronic ground and excited states. With this, we obtain a set of differential equations describing populations of the ground state in different vibrational quantum numbers  $n$ :

$$\begin{aligned} \frac{d}{dt}\rho_{nn} = & -\gamma \frac{\Omega_R^2}{4} \left( \sum_k \frac{|\langle n | e^{ikx} | k \rangle|^2}{[(k-n)\omega - \delta]^2 + \gamma^2/4} \rho_{nn} \right) \\ & + \gamma \frac{\Omega_R^2}{4} \left( \sum_{k,r} \int_{-1}^1 du N(u) \frac{|\langle n | e^{ikux} | k \rangle|^2 |\langle k | e^{-ikx} | r \rangle|^2}{[(k-r)\omega - \delta]^2 + \gamma^2/4} \rho_{rr} \right), \end{aligned} \quad (2.34)$$

where  $\rho_{nn} = \langle n | \rho | n \rangle$ .

In the Lamb-Dicke regime,

$$e^{ikx} = e^{i\eta(a+a^\dagger)} \sim 1 + i\eta(a + a^\dagger) - \frac{\eta^2}{2}(a^2 + a^\dagger a + aa^\dagger + a^{\dagger 2}). \quad (2.35)$$

We substitute this expression into the matrix elements in Eq. (2.34):

$$\langle n | e^{ikx} | k \rangle \sim \langle n | 1 + i\eta(a + a^\dagger) - \frac{\eta^2}{2}(a^2 + a^\dagger a + aa^\dagger + a^{\dagger 2}) | k \rangle. \quad (2.36)$$

After applications of  $a$  and  $a^\dagger$  to the vibrational state, we obtain (up to the second order in  $\eta$ )

$$|\langle n | e^{ikx} | k \rangle|^2 = (1 - \eta^2(2k+1))\delta_{n,k} + \eta^2 k \delta_{n,k-1} + \eta^2(k+1)\delta_{n,k+1}. \quad (2.37)$$

Now the summations in the RHS of Eq. (2.34) can be explicitly evaluated:

$$\begin{aligned} \sum_k \frac{|\langle n | e^{ikx} | k \rangle|^2}{[(k-n)\omega - \delta]^2 + \gamma^2/4} \rho_{nn} = \\ \left( \frac{1 - \eta^2(2n+1)}{\delta^2 + \gamma^2/4} + \frac{\eta^2(n+1)}{(\omega - \delta)^2 + \gamma^2/4} + \frac{\eta^2 n}{(\omega + \delta)^2 + \gamma^2/4} \right) \rho_{nn}, \end{aligned} \quad (2.38)$$

and

$$\begin{aligned} \sum_{k,r} \frac{|\langle n | e^{ikux} | k \rangle|^2 |\langle k | e^{-ikx} | r \rangle|^2}{[(k-r)\omega - \delta]^2 + \gamma^2/4} \rho_{rr} = & \left( \frac{1 - \eta^2(1+u^2)(2n+1)\rho_{nn}}{\delta^2 + \gamma^2/4} \right) \rho_{nn} + \\ & \left( \frac{\alpha\eta^2(n+1)}{\delta^2 + \gamma^2/4} + \frac{\eta^2(n+1)}{(\omega + \delta)^2 + \gamma^2/4} \right) \rho_{n+1,n+1} + \\ & \left( \frac{\alpha\eta^2 n}{\delta^2 + \gamma^2/4} + \frac{\eta^2 n}{(\omega - \delta)^2 + \gamma^2/4} \right) \rho_{n-1,n-1}. \end{aligned} \quad (2.39)$$

By introducing

$$\alpha = \int_{-1}^1 du N(u) u^2, \quad (2.40)$$

and  $P_n = \rho_{nn}$ , we write the rate equation to be

$$\begin{aligned} \dot{P}_n = & -\gamma \frac{\Omega_D^2 \eta^2}{4} \left( \frac{n+1}{(\omega - \delta)^2 + \gamma^2/4} + \frac{n}{(\omega + \delta)^2 + \gamma^2/4} + \frac{\alpha(2n+1)}{\delta^2 + \gamma^2/4} \right) P_n \\ & + \gamma \frac{\Omega_D^2 \eta^2}{4} \left( \frac{\alpha}{\delta^2 + \gamma^2/4} + \frac{1}{(\omega + \delta)^2 + \gamma^2/4} \right) (n+1) P_{n+1} \\ & + \gamma \frac{\Omega_D^2 \eta^2}{4} \left( \frac{\alpha}{\delta^2 + \gamma^2/4} + \frac{1}{(\omega - \delta)^2 + \gamma^2/4} \right) n P_{n-1}. \end{aligned} \quad (2.41)$$

We define the transitional rate

$$A_{\pm} = \frac{\alpha}{\delta^2 + \gamma^2/4} + \frac{1}{(\omega \mp \delta)^2 + \gamma^2/4}, \quad (2.42)$$

and write the rate equation as

$$\dot{P}_n = -\gamma \frac{\Omega_D^2 \eta^2}{4} (n A_- P_n + (n+1) A_+ P_n - A_+ n P_{n-1} - A_- (n+1) P_{n+1}). \quad (2.43)$$

We can now solve for a steady state solution by setting  $\dot{P}_n = 0$  and obtain

$$n A_- P_n + (n+1) A_+ P_n - A_+ n P_{n-1} - A_- (n+1) P_{n+1} = 0, \quad (2.44)$$

where the solution is given by  $P_n \propto e^{-n\beta}$  with

$$e^{\beta} = \frac{A_-}{A_+}. \quad (2.45)$$

This exponential weighting of the probability suggests that the steady-state population is described by a thermal state where the temperature,  $T$ , appears as

$$\beta = \frac{\hbar\omega}{k_B T}. \quad (2.46)$$

The steady state temperature,  $T_d$  of the trapped particle at the steady state is then given by

$$T_d = \frac{\hbar\omega}{k_B \ln \left( \frac{A_-}{A_+} \right)}. \quad (2.47)$$

It is more convenient for experimentalists to quote a temperature in the unit of the



Figure 2-6: Crystal of 37 ions under Doppler cooling.

mean vibrational number  $\langle n \rangle$  of the ion:

$$\langle n \rangle_d = \frac{T_d k_B}{\hbar \omega} = \frac{1}{\ln\left(\frac{A_-}{A_+}\right)}. \quad (2.48)$$

To find the optimal detuning,  $\delta_D$ , such that  $\langle n \rangle_d$  is the lowest, we need to maximize the term  $A_-/A_+$ . The exact expression of  $\delta_D$  is long and complicated. However, there are two limiting cases which are important:

$\delta_D \rightarrow -\omega$  as  $\gamma \rightarrow 0$ : In the tight binding limit ( $\omega \gg \gamma$ ), which we achieve by performing cooling on dipole forbidden transitions, the lowest temperature is achieved by having the laser frequency detuning equal to the red sideband frequency. This is nothing but a standard sideband cooling technique used routinely in trapped ion experiments [40]. In this regime,  $\langle n \rangle_d$  can be very close to 0 and is typically limited by the background heating rate of the trap.

$\delta_D \rightarrow -\gamma/2$  as  $\omega \rightarrow 0$ : In the weak binding limit ( $\omega \ll \gamma$ ), which we achieve by cooling with dipole transitions, the optimal detuning is roughly half the natural linewidth. This is exactly the same as in the case for free ions. Experimentally, the term Doppler cooling usually means performing cooling in this regime, and the Doppler temperature is a steady state temperature of the ion in this limit. Though the Doppler temperature is higher than that of the sideband cooling, the fast cooling rate in the Doppler cooling makes it more efficient to cool ions with very high initial temperature. Experimentally, we first apply Doppler cooling to bring the ion close to the Doppler temperature and then apply sideband cooling to cool the ion further to the motional ground state.

### 2.3.2.3 Cooling of $^{40}\text{Ca}^+$

For  $^{40}\text{Ca}^+$  (the energy diagram is given in Fig. 2-4), Doppler cooling is carried out on the  $^2\text{S}_{1/2} \rightarrow ^2\text{P}_{1/2}$  transition using laser light at 397 nm. However, the excited state  $^2\text{P}_{1/2}$  can also decay to a metastable state  $^2\text{D}_{3/2}$ . We have to apply repumper laser light at 866 nm to depopulate this state and keep on the Doppler cooling cycle. We operate our trap usually at the radial trap frequency of  $\sim 2\pi \times 3$  MHz, and the temperature of the ion after Doppler cooling is roughly  $\langle n \rangle_d \sim 5 - 7$ . A picture taken by a CCD camera of a trapped and Doppler cooled crystal of 37 ions is shown in Fig. 2-6.

For sideband cooling, in order to be in a tight binding regime, the cooling is done on the  $^2\text{S}_{1/2} \rightarrow ^2\text{D}_{5/2}$  transition using laser light at 729 nm. Laser light at 854 nm, which couples the  $^2\text{D}_{5/2}$  to the  $^2\text{P}_{3/2}$  state, artificially broadens the quadrupole transition and increases the cooling rate. For our trap, the lowest temperature of

the ion achieved using sideband cooling is roughly  $\langle n \rangle_d \sim 0.2$  [22]. The heating rate of the ion due to unknown noise from the trap prevents the temperature from going closer to 0.



# Chapter 3

## Lasers and experimental setup

Modern atomic physics experiments rely heavily on light produced from lasers to trap and manipulate atoms. Though the basic principle of lasers are the same regardless of the type of gain media, in our experiments, we use only semiconductor diode lasers, which are relatively cheap and easy to operate. However, there are some tricks we can play to improve the performance of diode lasers. In this chapter, we describe the laser setup for our experiment and various tricks required to make all the measurements in this thesis possible. We also describe other experimental hardware such as the trap and the vacuum chamber at the end of this chapter.

### 3.1 Laser sources

#### 3.1.1 Diode lasers

The main constraint in choosing a light source is the frequency of the light required by the experiment. Here we summarize the required laser wavelengths Table 3.1. For calcium ions, it is fortunate that all required laser frequencies can be obtained by means of diode lasers. There are many good textbooks on the physics of lasers (see, for example, [41]) which describe mechanisms to achieve population inversions in the p-n junction of semiconductor diode lasers in details. For our purpose, we can treat any laser diode as a simple light-emitting diode (LED). We simply correctly connect the diode pins to a current source and there will be laser light coming out.

##### 3.1.1.1 Free-running diode laser (375 nm)

A free-running diode laser might have a short term spectral linewidth of around 10-100 MHz. However, an uncontrolled optical feedback and a variation in temperature usually make the frequency of the laser light unstable, resulting in a long-term spectral linewidth of up to 0.1 % of its center frequency. The stability of the frequency is adequate for photo-ionization of neutral calcium atoms since any photon wavelength shorter than 391 nm will ionize calcium atoms excited to the  $^1P_1$  state. In our experiment, we use a free-running and non-temperature controlled laser diode at 375 nm produced by Nichia (NDU4116).

$\lambda$ (nm)	Power ( $\mu\text{W}$ )	Function
422 (844)	200	to excite neutral calcium atoms
375	100	to ionize excited neutral calcium atoms
397	100	main Doppler cooling of calcium ions
866	1,000	repumper for Doppler cooling of calcium ions
854	300	repumper for qubit manipulation of calcium ions
729	20,000	to address the $S_{1/2}$ - $D_{5/2}$ transition of calcium ions

Table 3.1: Laser light wavelengths required to perform experiments. The energy diagrams for calcium ions and atoms are shown in Fig. 2-4 and 2-3, respectively. The power listed is what is typically measured before the viewport of the vacuum chamber. The laser light at 422 nm is frequency doubled from a diode laser source at 844 nm.

### 3.1.1.2 External cavity diode lasers (397 nm, 866 nm, 844 nm and 854 nm)

To make diode lasers more useful for the experiment, we have to reduce the spectral linewidth of the laser light and make the frequency stable. By putting an external grating to provide a controlled optical feedback back to the diode laser, the spectral linewidth can be reduced to sub-MHz. This so-called external cavity diode laser (ECDL) is widely used in modern atomic physics experiments. We use complete systems from Toptica® for laser wavelengths at 397 nm (DL 100), 866 nm (DL 100), 844 nm (DL Pro) and 854 nm (DL Pro).

One caution in using an ECDL comes from an intrinsic spontaneous background light. Although a diode laser has a strong laser light intensity at the center frequency, there is a broad background light (usually 30 dB less than the center frequency) in the range of  $\pm 5$  nm or more. This can cause an unwanted off-resonant excitation of any atomic transition. For example, laser light at 397 nm produced from the laser diode also contains background light at 393 nm. This background light can off-resonantly excite the ions to the  $^2\text{P}_{3/2}$  state. This state can decay to the metastable state  $^2\text{D}_{5/2}$  and halt the Doppler cooling process, which is clearly undesirable. We observed that, without filtering out this background light, the fluorescence from the ions is reduced by roughly 50%.

To spectrally filter out background light, we use a pair of dispersive prisms (Thorlabs® PS850) to deflect unwanted light from the main beam path. In principle, we can also use a ruled grating, which has substantially higher resolving power. However, there is usually an unavoidable loss in the laser power of about 25 %. Using prisms at the Brewster's angle maximizes light transmission and we achieve an optical loss of less than 5 % with correct light polarization.

### 3.1.2 Frequency doubling system (422 nm)

At the beginning of the setup of the experiments (early 2009), a direct diode source at 422 nm was not available.<sup>1</sup> We instead frequency double laser light at 844 nm to produce laser light at 422 nm.

#### 3.1.2.1 Non-linear crystal

The principle behind frequency doubling is a non-linear response of a crystal. In our case, we use a periodically-poled-potassium-titanyl-phosphate crystal (PPKTP) to convert light from 844 nm to 422 nm. In a non-linear crystal, the response of the polarization  $P(t)$  of the crystal lattice can be generally written as

$$P(t) = aE(t) + bE^2(t) + \dots, \quad (3.1)$$

where  $E(t)$  is the electric field of the incoming light and  $a, b$  are constants related to the property of the crystal. We assume that the monochromatic input light is a plane wave  $E(t) = E_0 \cos(\omega_{\text{laser}}t - kz)$ . The polarization response of the crystal then becomes

$$P(t, z) = aE_0 \cos(\omega_{\text{laser}}t - kz) + bE_0^2 (1 + \cos(2\omega_{\text{laser}}t - 2kz)) + \dots \quad (3.2)$$

We see that the last term oscillates with a frequency twice of that of the input laser frequency. A detailed analysis on phase matching and efficiency optimization can be found in [42].

#### 3.1.2.2 Bow-tie cavity

Eq. (3.2) suggests that the amplitude of the input light should be as high as possible to efficiently generate frequency doubled light. We use a bow-tie optical cavity around the doubling crystal to build up the laser power of the 844 nm laser light. The setup of the cavity is shown in Fig. 3-1 and 3-2. The length of the cavity is locked to the 844 nm laser frequency using the Pound-Drever-Hall technique. With an input 844 nm light power at around 120 mW, we generally obtain 2-3 mW of laser light at 422 nm. Note that the output coupler mirror is curved on both sides. This is to reduce the divergence of the 422 nm beam coming out from the bow-tie cavity.

We tune the temperature of the PPKTP crystal to achieve highest doubling efficiency. The crystal is wrapped with a nichrome wire and placed in a teflon holder to minimize any temperature drift. The optimal temperature is about 50°C which we control using a microcontroller.

### 3.1.3 Narrow linewidth diode laser (729 nm)

The laser light with the most stringent requirement in our experiment is the 729 nm laser light which we use to address the quadrupole transition of  $^{40}\text{Ca}^+$ . The linewidth

---

<sup>1</sup>Now the diode can be obtained from Nichia®. The part number is NDV4A16E.

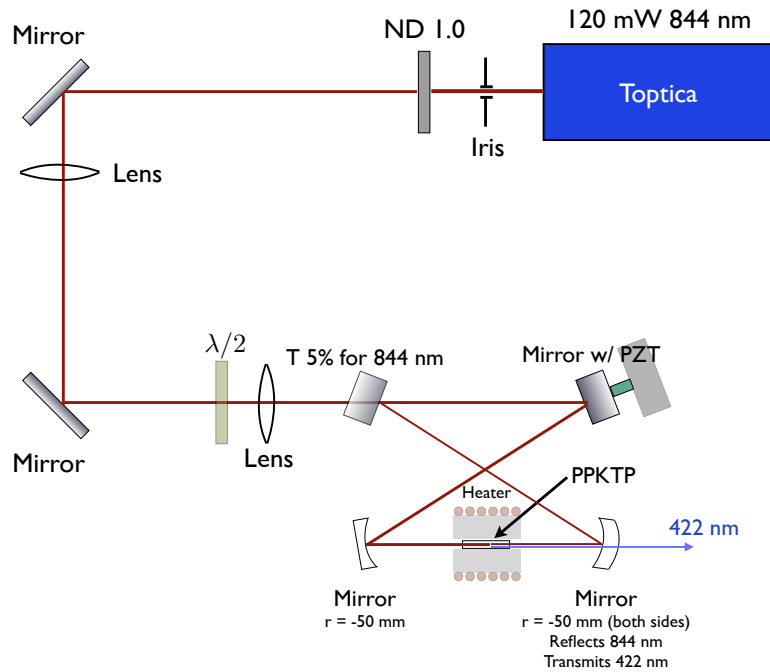


Figure 3-1: Frequency doubling cavity for generation of 422 nm light.

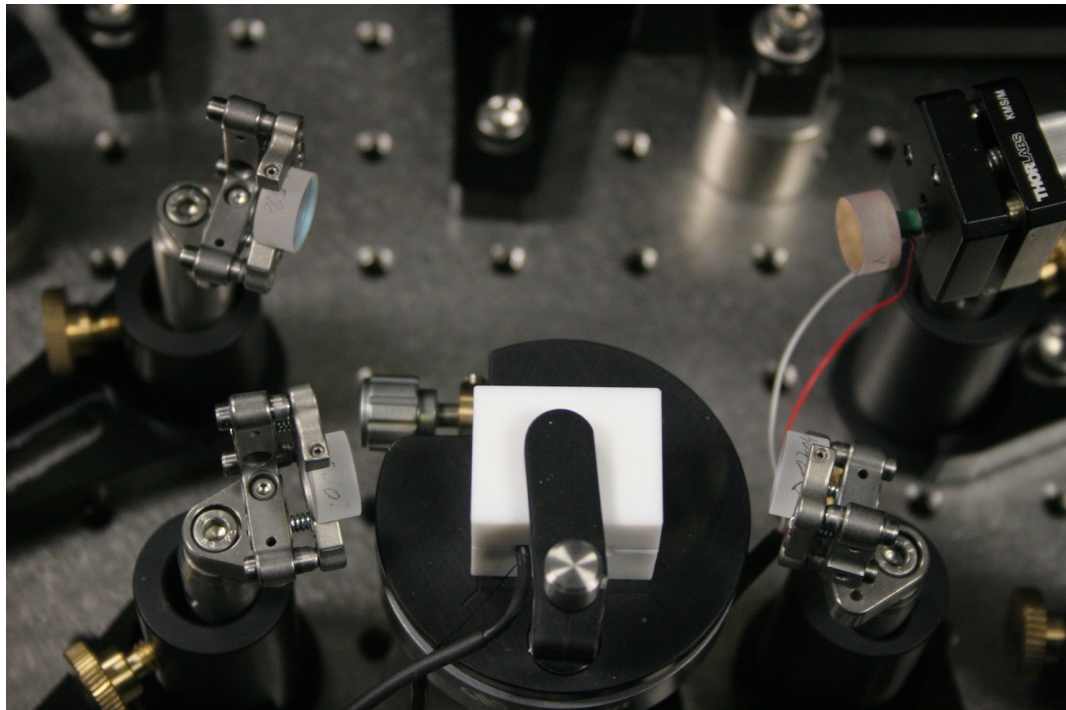


Figure 3-2: Bow-tie cavity currently used in our experiment. We house the PPKTP doubling crystal in a white teflon holder to minimize any temperature drift.

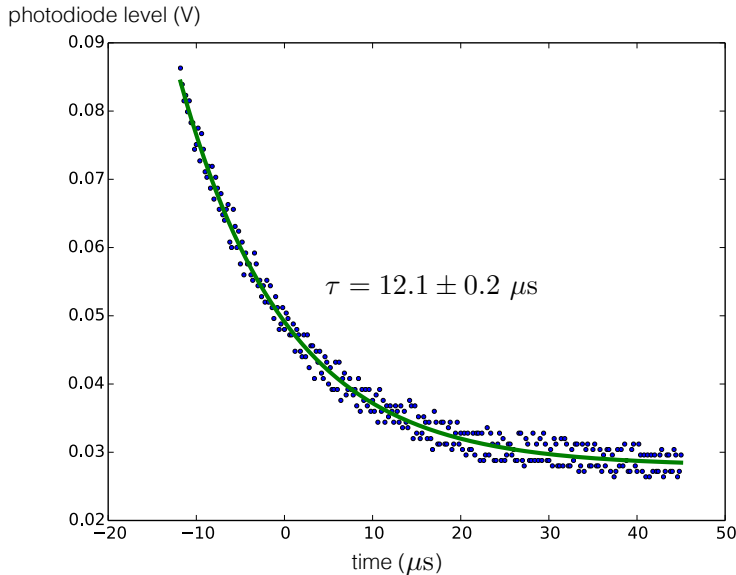


Figure 3-3: Cavity ring-down signal for the high finesse cavity.

of this laser frequency determines the fidelity of the qubit operation. For basic state manipulations, the linewidth of the laser should be sub-kHz, which requires locking a laser light to a stable and high finesse cavity.

The optical cavity used in our setup has been built by Stable Laser Systems<sup>®</sup>. It consists of a pair of mirrors that form a cavity with a free-spectral range of  $f_{\text{FSR}} = 3.25 \text{ GHz}$  and a finesse of  $\sim 245,000$ . We verified the finesse with a cavity ring-down technique. Fig. 3-3 shows the cavity transmission signal during the ring-down measurement. The time constant of the exponential decay is measured to be  $\tau = 12.1 \pm 0.2 \mu\text{s}$ . The cavity is placed in a (gold plated!) radiation shield under vacuum. The shield is temperature controlled to minimize cavity length drifts due to changes in the ambient temperature. We set the temperature of the shield close to  $0^\circ \text{ C}$ .<sup>2</sup> The cavity is inserted into the vacuum apparatus in a clean room to avoid dust accumulating on the mirrors. Bringing a camera into the clean room would have taken additional measures. We instead show a picture in Fig. 3-5 taken from Ref. [43]. The vacuum chamber is placed inside a box to reduce acoustical noise, as shown in Fig. 3-5.

Pumping down of the vacuum chamber with the high finesse cavity requires special care as air currents can lead to dust accumulating at the mirrors. To prevent strong air currents during pumping down, we use a blank copper gasket with a small hole to reduce the pumping cross-section and speed. With this gasket in place, we reduce the pressure in the vacuum chamber until it is safe to turn on an ion pump. We then disconnect the rough pump after that point. During this pumping process, it turned out that our hole was not small enough and the pressure dropped too quickly.<sup>3</sup>

---

<sup>2</sup>This corresponds to  $32.00 \text{ k}\Omega$  of the thermistor resistance.

<sup>3</sup>It is recommended that the pressure reaches 1 torr in about 10 minutes. During our pumping

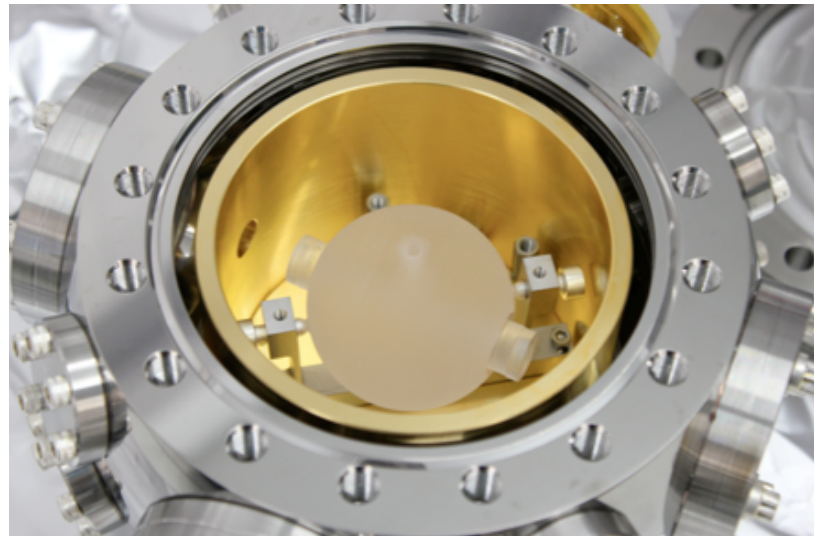


Figure 3-4: High finesse stable cavity for the 729 nm laser light. The picture is taken from [43].

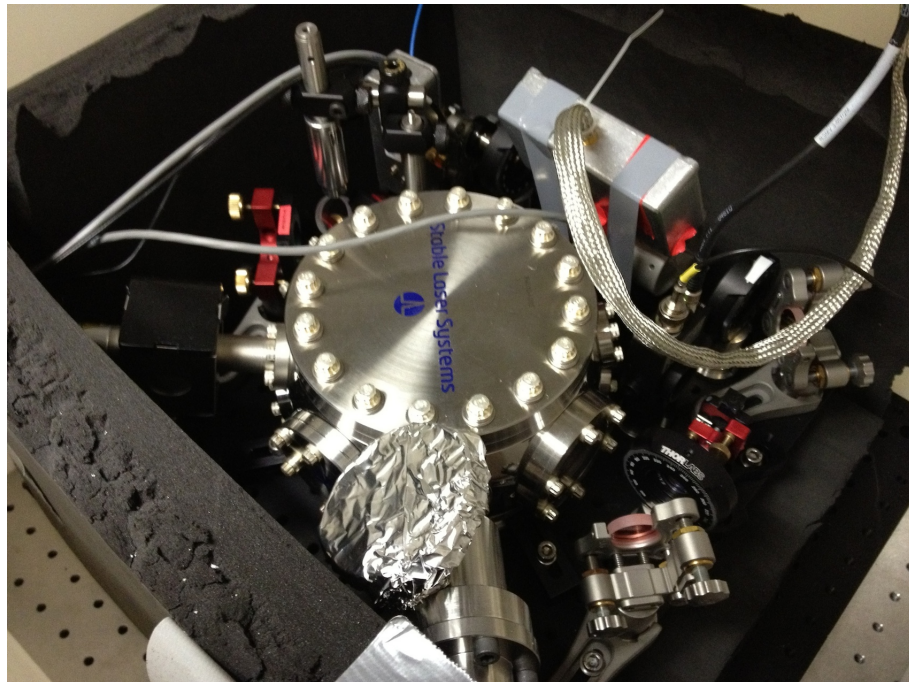


Figure 3-5: Setup for the high finesse cavity for the 729 nm laser light. The vacuum chamber, which houses the cavity, and the optics are mounted on a breadboard. The whole setup is put on rubber balls to damp out acoustic noise.

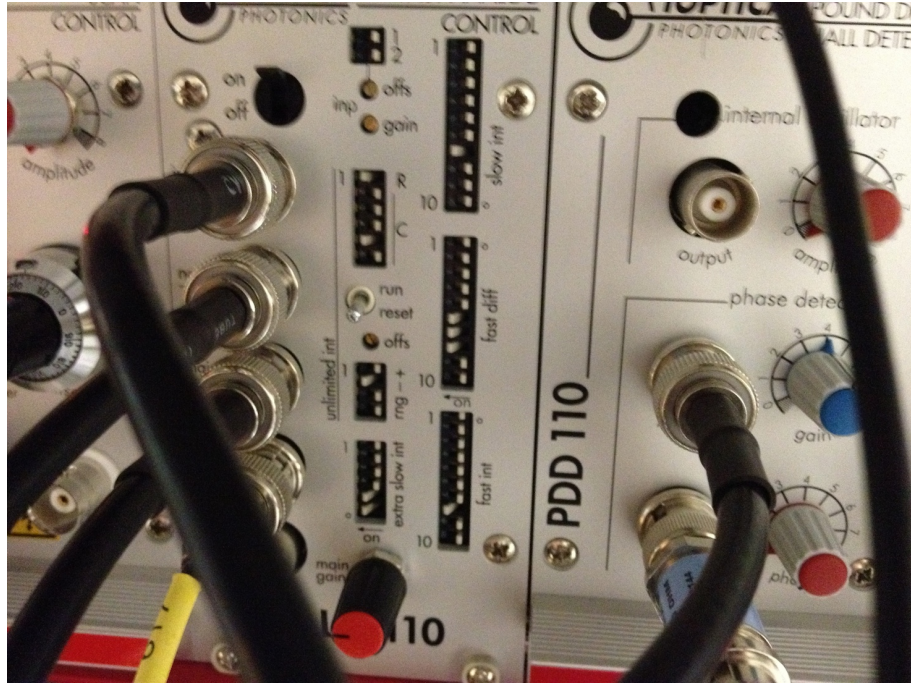


Figure 3-6: Setting of the locking parameters for the 729 nm diode laser using a FALC module.

Fortunately, the measured finesse is similar to the one measured at J. P. Home's group (about 270,000 in their case [43]).

Our 729 nm source is a DLpro ECDL module from Optica<sup>®</sup> with the Fast Analog Linewidth Control (FALC) locking circuit. The locking parameter settings are shown in Fig. 3-6. To find the optimal locking parameters, it is useful to look at the beat signal of 729 nm before and after a passing through an AOM at 220 MHz and a 22-meter-long optical fiber. The so-called servo bump, which is a frequency modulation of the laser light from the feedback circuit, is prominent in the trace labeled “locked” in Fig. 3-7. The locking parameters should be set such that the servo bump is minimized. However, we observe that minimizing the servo bump makes the laser lock less stable and rather unusable. We made a compromise such that the lock stability is acceptable and the laser stays locked for a few hours. The FALC unit is quite unconventional to use because there is no lock-unlock switch. To lock the laser, we simply tune the piezo of the laser slowly to the cavity frequency, and then the laser will be automatically locked (provided we set the locking parameters correctly).

To increase the power from the 729 nm laser system, we send the output of the 729 nm diode laser DLpro ( $\sim 35$  mW) to a tapered amplifier (TA) chip from Eagleyard<sup>®</sup>. The TA also needs to be temperature controlled. The net output from the TA is more than 500 mW. After a few beam shaping optical elements and optical isolators, the light power is about 330 mW. We have about 120 mW of 729 nm laser power

---

down, the pressure reached 1 torr in about 2-3 minutes.

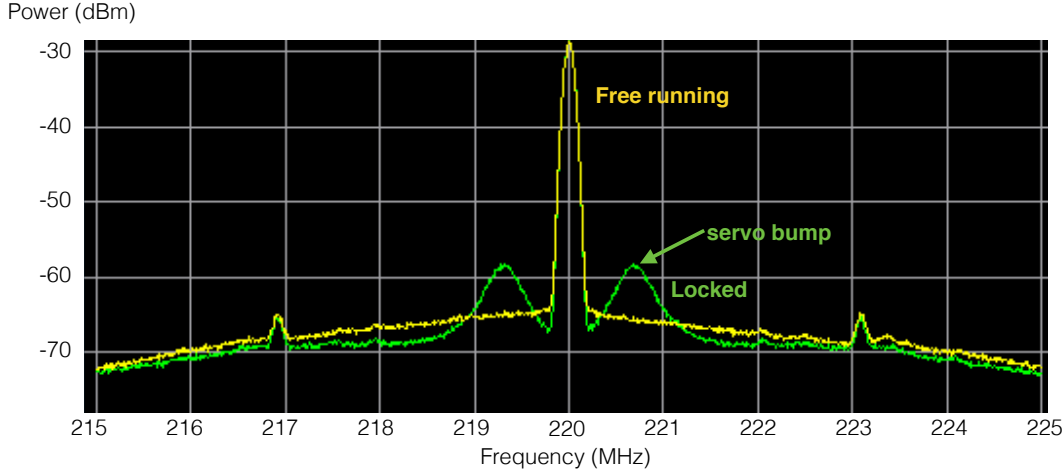


Figure 3-7: Beat signals between laser light shifted by 220 MHz using an AOM and the unshifted light for free-running and frequency stabilized (locked) laser light. In the frequency stabilized case, sidebands from the stabilization electronic circuit (servo bumps) at  $\sim 700$  kHz are clearly visible.

available on the experimental optical table.

In the experiments, we use two independently controlled laser beams at 729 nm. Both beam paths are shown in Fig. 3-8. We make use of the objective lens which is optimized for imaging of ions to achieve single ion addressing of the 729 nm laser light on the ions. The objective lens is also optimized to collect photons at 397 nm. A dichroic mirror overlaps both the red and the blue beam paths.

### 3.1.4 Switching and frequency shifting of lasers

We use acousto-optical modulators (AOMs) to switch on and off the laser light and shift its frequency. AOMs in a standard double-pass configuration allow us to shift the laser frequency without displacing the laser beam. For the main Doppler cooling beam at 397 nm, we make a slight modification such that the zeroth-order beam path of the AOM is also reflected and overlapped with the frequency shifted laser path. This allows us to switch to a far red-detuned beam for crystallization of a longer ion chain without using an additional AOM. Fig. 3-9 shows how we configure the AOM.

## 3.2 Experimental setup

### 3.2.1 General structure of the laboratory

All the laser sources are located in a separated room from the main experiment room, as shown in Fig. 3-10. This configuration of the laboratory makes it easy to share all the laser light among all experiments in the group. The light is delivered to each optical table through long optical fibers (22-meter long).

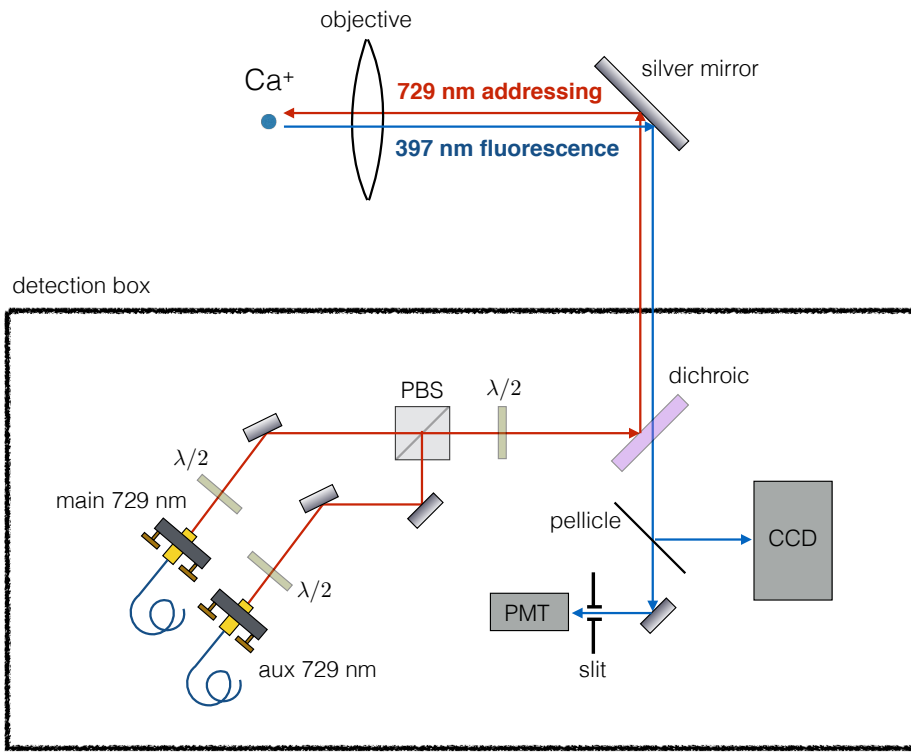


Figure 3-8: Beam paths for 729 nm and ions imaging. The 397 nm photons scattered from the ions in the trap collected using an objective lens are divided with 20% to the CCD camera and 80% to the PMT. The same beam path is used to deliver 729 nm laser light to the ions. The two 729 nm light paths are for addressing two ions in the trap independently, which is required by the experiment in Chapter 7.

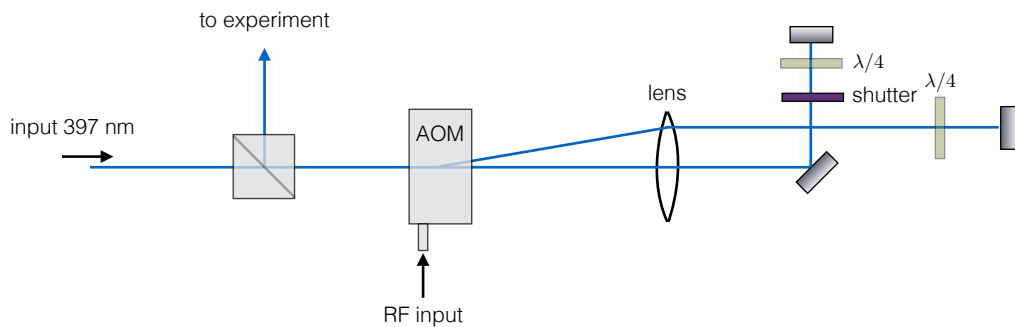


Figure 3-9: A modification to a standard double pass AOM setup to have the zeroth-order beam path overlapped with the frequency shifted beam path.

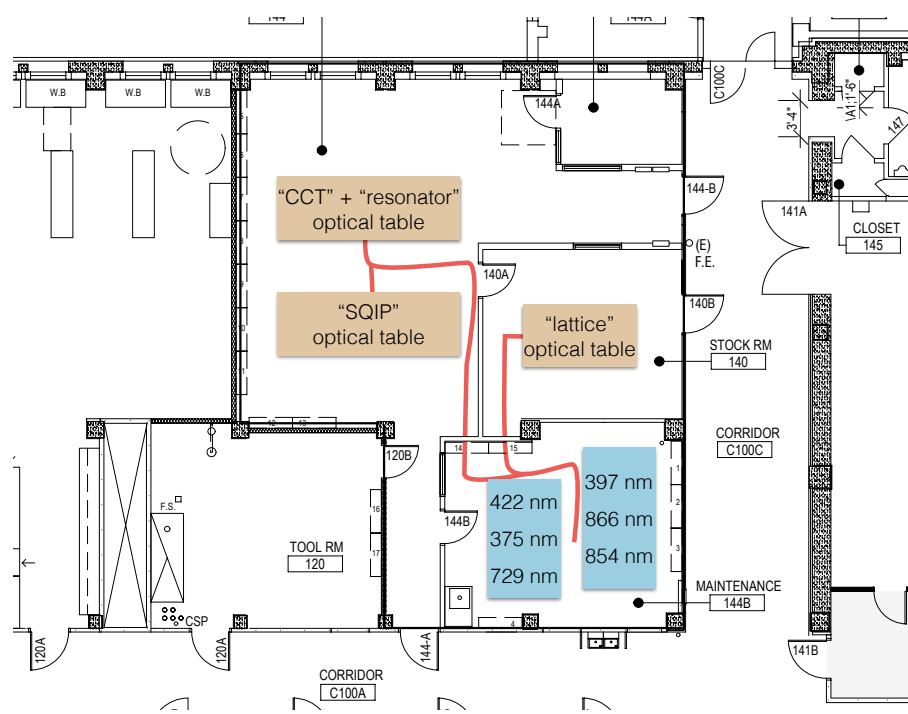


Figure 3-10: Layout of the laboratory. All the lasers are in a separated room from the main experiment room. Long optical fibers (shown in red paths) deliver all the light to the experimental tables. All long fibers are 22-meter long. This configuration allows easy sharing of laser light among all experiments in the group.

$\lambda$ (nm)	Frequency (THz)	Note
729	411.04250	used to calibrate the wave-meter
375	-	free-running
422	354.53917	laser frequency before doubling
397	755.22244	not including +220 MHz after AOMs
866	346.00002	not including +160 MHz after AOMs
854	350.86265	not including +160 MHz after AOMs

Table 3.2: Laser light frequencies measured by the wave-meter for trapping of  $^{40}\text{Ca}^+$ .

### 3.2.1.1 Using long optical fibers

The laser light polarization stability through long polarization-maintaining (PM) fibers (22 meters) suffers a lot from the temperature and mechanical instability of the fibers. Despite extensive efforts, we were not able to reduce the polarization drifts for the fibers transmitting the 397 nm and 375 nm laser light to an acceptable value. However, switching from PM fibers to non-PM fibers seems to have mitigated the polarization drifts. The current fibers we use for 397 nm and 375 nm are 405-HP fibers from Thorlabs<sup>®</sup>, where the polarizations of the laser light are stable for more than 2-3 days.

Other long PM fibers for 729 nm, 866 nm and 854 nm seem to perform well. However, the fiber for the 729 nm laser might introduce additional noise which effectively broaden the linewidth of the laser frequency. In the future, we plan to implement a scheme to cancel any laser noise introduced from a long optical fiber similar to the scheme used in [34].

### 3.2.1.2 Calibration of laser frequencies

Finding correct laser frequencies is relatively easy using a wave-meter (HighFinesse<sup>®</sup> model WS-7) which has an absolute accuracy of 60 MHz. However, the wave-meter needs to be calibrated with a known laser wavelength. Since the 729 nm laser is always locked to a stable optical cavity, we calibrate the wave-meter such that the reading for 729 nm is always 411.04250 THz.<sup>4</sup> Other laser frequencies can then be determined on the wave-meter and are summarized in Table 3.2.

We monitor the frequency of the high finesse cavity which the 729 nm laser is locked to by performing spectroscopy on the  $^{40}\text{Ca}^+$  ion. The results over a few months is shown in Fig. 3-11. The cavity also exhibits a short-term drift, as shown in Fig. 3-12. This is mainly due to temperature drifts during the day. Usually, the drift is on the order of 1 Hz/s.

---

<sup>4</sup>To calibrate the WS-7 wave-meter, the input fiber needs to be a FC/PC fiber.

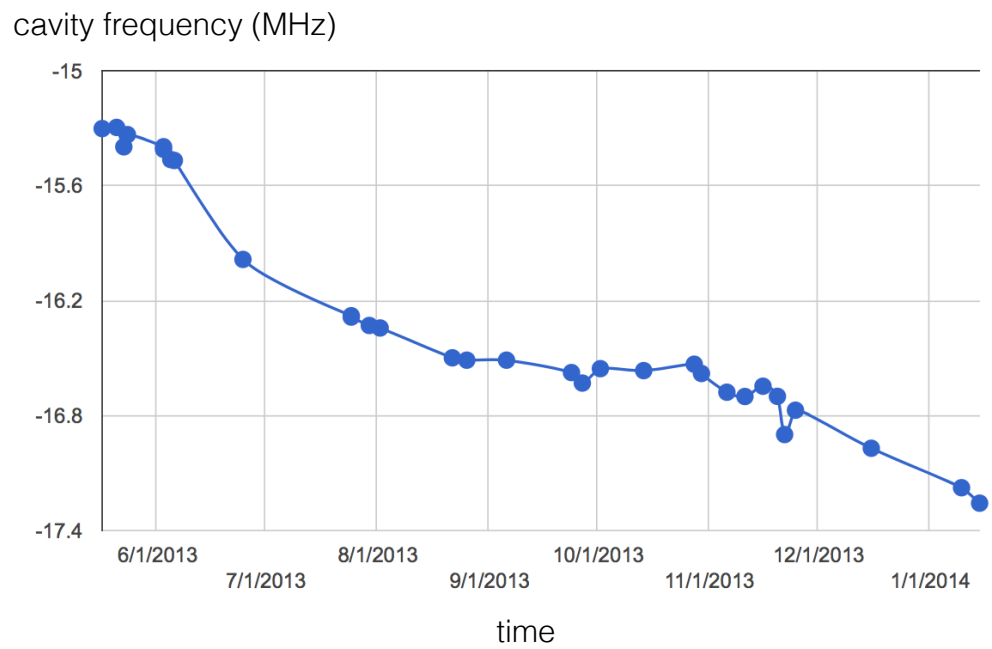


Figure 3-11: Cavity center frequency as measured relative to the center of the S-D transition in  $^{40}\text{Ca}^+$  over a period of 6 months. The frequency shown is relative to the AOM center frequency (220 MHz).

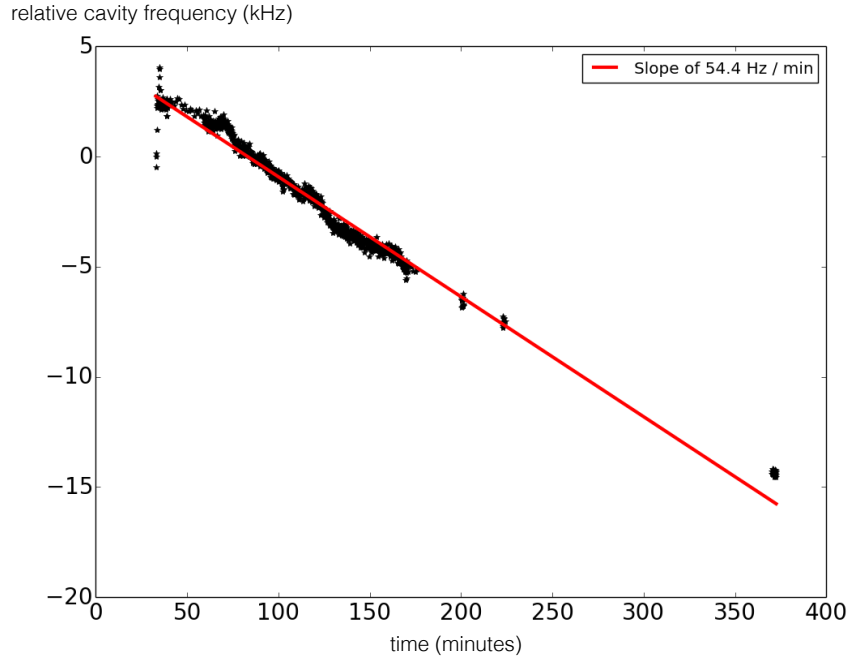


Figure 3-12: Short-term drift of the center frequency of the high finesse cavity. The drift is about 1 Hz/second.

### 3.2.2 Helical resonator

For trapping, we require voltages of 100-200 V<sub>pp</sub> at the RF electrodes. Using a commercial amplifier to reach this level is not practical since most of the amplifiers in the market are designed to drive 50 Ω loads. However, the trap electrodes represent mainly a capacitive load. A more practical way is to use a resonator circuit, such as a helical resonator.

Since we apply voltages 180° out of phase to the two pairs of the RF electrodes, we configure our helical resonator to be a half-wave resonator. The voltages on both ends of the resonator are automatically out of phase with respect to each other. For an ideal helical resonator, the voltage on the resonator is zero exactly at the middle (see Fig. 3-13, where we plot the voltage as a function of the position along the resonator). Since our resonator has uneven spacing and diameter, it is difficult to determine exactly the center of the resonator. Instead of explicitly grounding the center of the resonator, we leave the ground floated, which seems to work well.

### 3.2.3 Vacuum system and trap construction

The vacuum system and the trap construction are shown in Fig. 3-14 and 3-15, respectively. More details can be found in Michael Ramm's thesis.

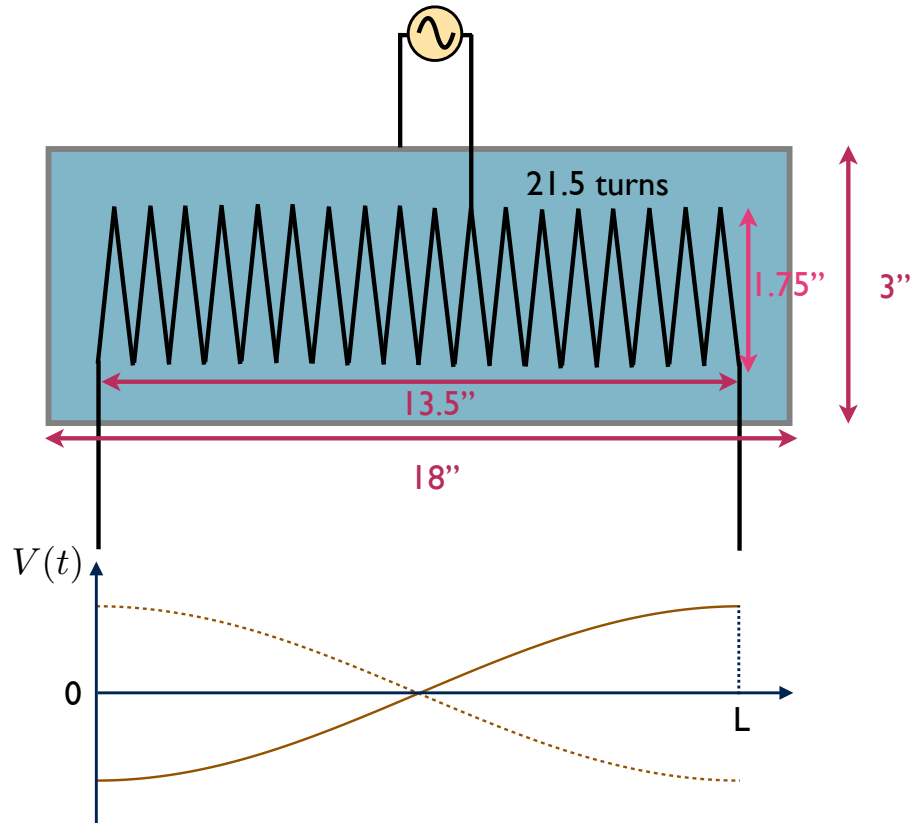


Figure 3-13: The half-wave resonator used to generate voltages out-of-phase from each other on the two ends of the resonator. The voltage of the resonator is plotted as a function of the position along the resonator coil. We excite the resonator by a direct drive close to the center. For an ideal resonator, the center of the resonator is where the potential is always zero and should be grounded. Since our resonator is uneven in the coil spacing and diameter, we leave the center floated (ungrounded).

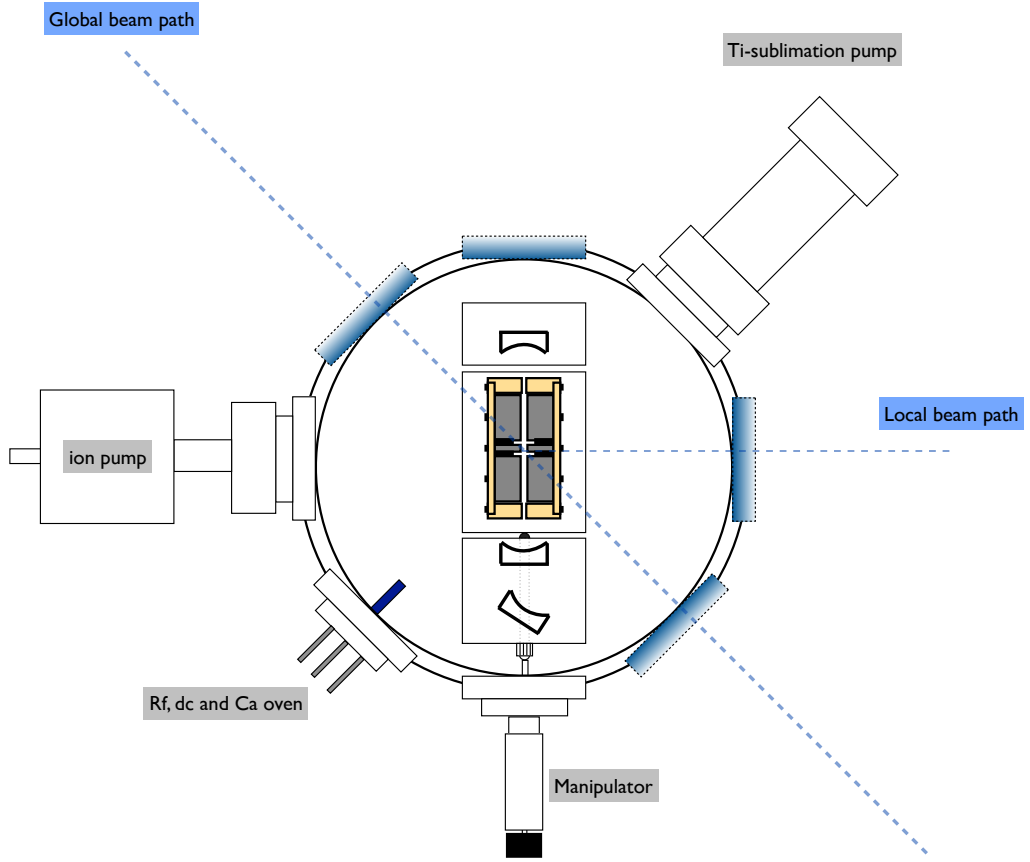


Figure 3-14: Vacuum setup for the experiment viewed from the top. We send the Doppler cooling and photoionization lasers through one of the side viewport (the global beam path). The local beam path is for additional laser beams used in experiments described in Michael Ramm's thesis. The three curved mirrors are for the optical cavity designed for the experiment in Chapter 8. The manipulator is designed to be able to fix the position of the optical cavity with respect to the trap. The RF input for the RF electrodes, DC input for the endcaps and neutral calcium oven are mounted on the same feedthrough. We found that grouping together all the electrical connections on the same feedthrough makes debugging extremely inconvenient. In the next generation of the trap, we plan to separate these electrical connections using different feedthrough flanges.

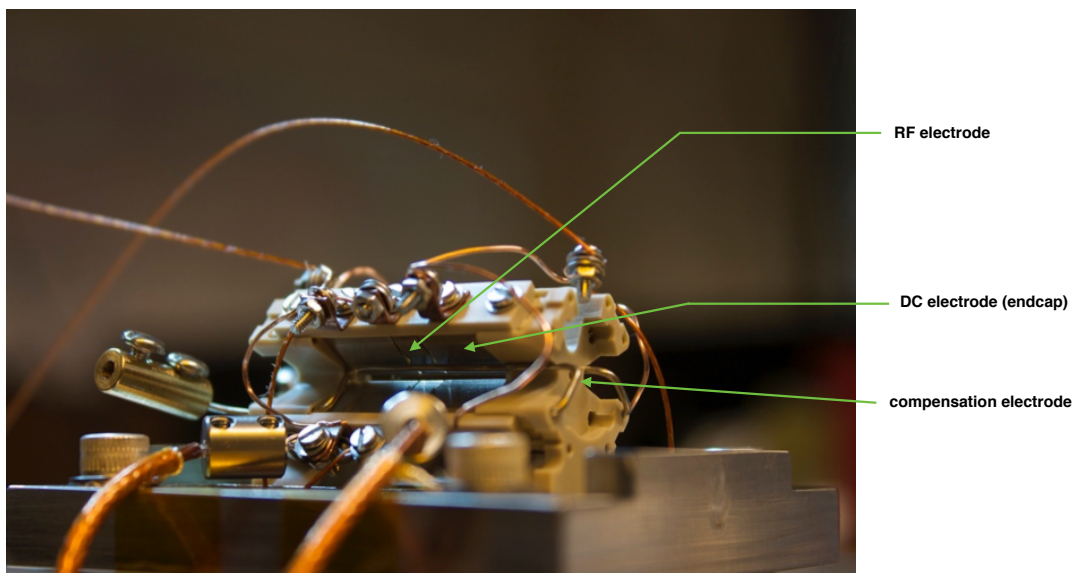


Figure 3-15: The Paul trap used in our experiment. All electrodes are mounted on insulating ceramic pieces. The RF electrodes are about 3 mm wide. The gap between opposite RF electrodes is 1 mm. More details in trap construction can be found in Michael Ramm's thesis.

# Chapter 4

## Spectroscopy of dipole transitions

To measure an energy splitting between energy levels in an atom, we usually perform spectroscopy by scanning the frequency of the laser light across the atomic transition and recording photons scattered from an atom. In trapped ions, this is not straightforward since the excited state of the transition used for Doppler cooling in many ion species usually has more than one decay channel. This requires us to use an additional repumper laser together with the main cooling laser. An interference between these two lasers gives rise to dark resonances, which are similar to the electromagnetically induced transparency (EIT) effect, which complicates the spectroscopy of these transitions since the presence of additional lasers greatly alters the line-shape of the atomic transition. In this chapter, we use fast laser switching to perform spectroscopy of dipole transitions in trapped  $^{40}\text{Ca}^+$ . We circumvent the usual problem due to dark resonances by rapidly alternating the probe laser and the repumper laser. Moreover, we reduce the laser pulse duration to minimize Doppler heating when scanning the probe laser across the atomic transition. We apply this experimental scheme to directly observe modulations of the fluorescence spectra due to micromotion in a Paul trap and experimentally confirm the dependence of the modulation index on the radial trap frequency.

### 4.1 Dark resonances and Doppler heating

Dark resonances are quantum interferences among different quantum states when more than one laser light is present. This situation frequently arises in atoms with the level structure shown in Fig. 4-1. While the resulting effects such as electromagnetically induced transparency (EIT) are generally interesting, the laser parameters for Doppler cooling have to be set more carefully to maximize the cooling efficiency. Moreover, with a finite magnetic field applied to the atom, dark resonances from every magnetic sub-level can substantially hinder the Doppler cooling efficiency if the frequencies of the two lasers accidentally match the EIT condition.

Dark resonances also complicate the spectroscopy of either the  $|g\rangle \rightarrow |e\rangle$  or  $|d\rangle \rightarrow |e\rangle$  transitions. For example, if we scan the frequency of the 397 nm laser in  $^{40}\text{Ca}^+$  across the atomic transition to find the line center, the shape of the resul-

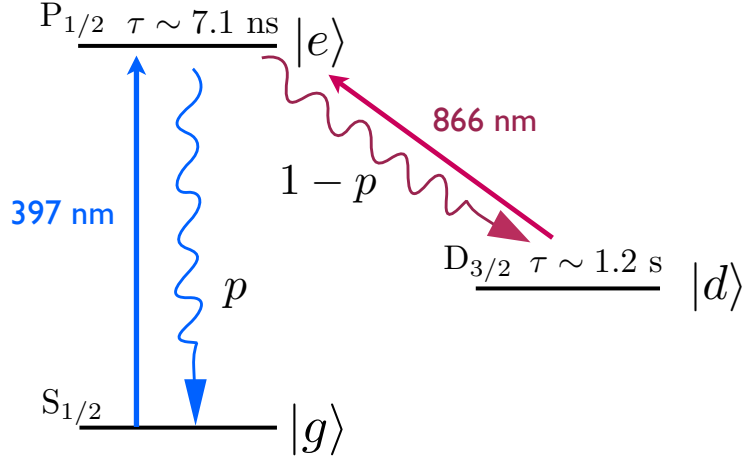


Figure 4-1: Typical lambda-level structure for an atom with a simple valence electron and a low lying D-state. The excited state  $|e\rangle$  can decay to the ground state  $|g\rangle$  or the metastable state  $|d\rangle$  with probabilities of  $p$  and  $1 - p$ , respectively. The laser wavelengths are for  $^{40}\text{Ca}^+$ .

tant fluorescence spectrum depends on the 866 nm laser parameters. While the line shape can be modeled using eight-level Bloch equations, the parameters we need to control include the intensities, polarizations, frequencies, directions of both lasers as well as the magnitude and direction of the magnetic field [44]. This large number of parameters contribute significant uncertainties in determining the line centers of both atomic transitions. Reaching a precision of less than a few MHz is particularly challenging [45].

Another complication is the fact that the transition which we want to perform spectroscopy on is the one we use for Doppler cooling. When we scan the probe 397 nm laser across the transition, the ions significantly heat up when the frequency of the probe laser is blue detuned from the center of the atomic transition. The energy acquired by the ion from this process can cause the ion to escape from the trap. A possible experimental scheme that circumvents this problem is to use sympathetic cooling, which adds at least one more laser beam path [46, 47]. Moreover, one has to make sure that the cooling rate is sufficient to maintain the whole ion crystal close to the Doppler temperature.

## 4.2 Spectroscopy with a single probe laser

To circumvent both the dark resonances and Doppler heating effect in trapped ions, we utilize fast laser switching to perform spectroscopy of both the  $|g\rangle \rightarrow |e\rangle$  and  $|d\rangle \rightarrow |e\rangle$  transitions. For  $^{40}\text{Ca}^+$ , the two dipole transitions are the  $^2\text{S}_{1/2} \rightarrow ^2\text{P}_{1/2}$  and  $^2\text{D}_{3/2} \rightarrow ^2\text{P}_{1/2}$  transitions. The idea is to have only one probe laser on during the probing time. If the probe pulse is sufficiently short and weak, the number of photons scattered is directly proportional to the coupling rate (or the scattering rate)

from the probe laser. Specifically, we first prepare the atoms in the ground state  $|g\rangle$ . Then we induce a transition to the excited state  $|e\rangle$  and detect photons scatter from the atoms. However, the atom might decay to the metastable state  $|d\rangle$ . A repumper laser is applied to depopulate the  $|d\rangle$  state. A similar procedure is used to probe the  $|d\rangle \rightarrow |e\rangle$  transition. In the following section, we present now the theory and experiments demonstrating this novel technique.

### 4.2.1 Time evolution of atomic populations

#### 4.2.1.1 Spectroscopy on the $|g\rangle \rightarrow |e\rangle$ transition.

To perform spectroscopy on the  $|g\rangle \rightarrow |e\rangle$  transition, we have a probe laser which couples these two states. The coupling rate is given by  $R_0$ . The excited state can decay to either the ground state  $|g\rangle$  or the metastable state  $|d\rangle$  with probabilities given by  $p$  and  $1-p$ , respectively (as shown in Fig. 4-1). With only one laser present, the atomic populations can be modeled using a set of rate equation given by [48]

$$\frac{d\rho_g(t)}{dt} = -R_0\rho_g(t) + (p\gamma + R_0)\rho_e(t) \quad (4.1)$$

$$\frac{d\rho_e(t)}{dt} = R_0\rho_g(t) - (\gamma + R_0)\rho_e(t) \quad (4.2)$$

$$\frac{d\rho_d(t)}{dt} = (1-p)\gamma\rho_e(t), \quad (4.3)$$

where  $\gamma$  is the decay rate of the excited state. With the initial conditions  $p_e(0) = p_d(0) = 0$  and  $p_g(0) = 1$ , we can solve for the time evolution of the excited state population exactly:

$$p_e(t) = \frac{2R_0 e^{-t(\gamma+2R_0)/2}}{\sqrt{(\gamma+2R_0)^2 - 4(1-p)\gamma R_0}} \sinh\left(\frac{t}{2}\sqrt{(\gamma+2R_0)^2 - 4(1-p)\gamma R_0}\right). \quad (4.4)$$

In the limit of low saturation,  $R_0 \ll 1$ , the expression is reduced to

$$\rho_e(t) = \frac{R_0}{\gamma} e^{-(1-p)R_0 t}. \quad (4.5)$$

The number of photons scattered after a duration  $T$  given by

$$N(T) = \int_0^T \rho_e(t)\gamma dt = \frac{1}{1-p} (1 - e^{-(1-p)R_0 T}). \quad (4.6)$$

If the detection duration  $T$  is short such that  $(1-p)R_0 T \ll 1$ , we can expand the exponent and obtain

$$N(T) \approx R_0 T \left(1 - (1-p)\frac{R_0 T}{2} + \dots\right). \quad (4.7)$$

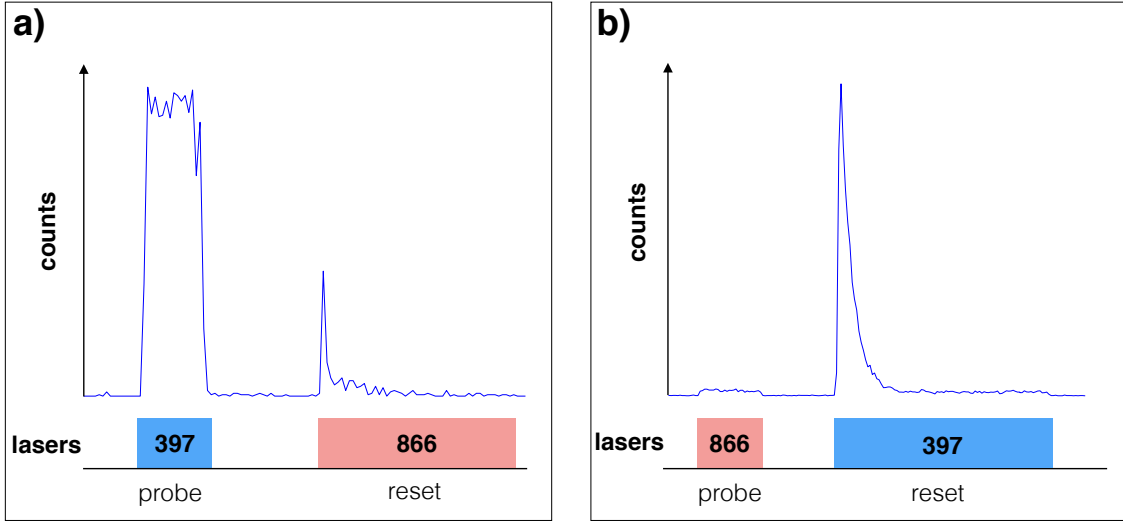


Figure 4-2: Typical averaged fluorescence dynamics collected for  $\sim 10^6$  measurement cycles. (a) Laser intensities are adjusted to perform spectroscopy on the  $|g\rangle \rightarrow |e\rangle$  transition. (b) The spectrum of the  $|g\rangle \rightarrow |e\rangle$  transition is observed by collecting photons at 397 nm scattered when the 866 nm probe laser is turned on.

This suggests that for  $R_0 \ll 1$  and  $(1 - p)R_0 T \ll 1$ , the number of photons scattered is directly proportional to the coupling rate of the laser  $R_0$ .

#### 4.2.1.2 Spectroscopy on the $|d\rangle \rightarrow |e\rangle$ transition.

Performing spectroscopy on the  $|d\rangle \rightarrow |e\rangle$  transition is slightly different from the previous case because experimentally we do not directly detect photons scattered from the  $|d\rangle \rightarrow |e\rangle$  transition. Instead, we extract the coupling rate,  $R'_0$ , of the laser addressing  $|d\rangle \rightarrow |e\rangle$  by measuring photons emitted from  $|e\rangle$  to  $|g\rangle$ .

The rate equations are given by

$$\frac{d\rho_g(t)}{dt} = p\gamma\rho_e(t) \quad (4.8)$$

$$\frac{d\rho_e(t)}{dt} = R'_0\rho_d(t) - (\gamma + R'_0)\rho_e(t) \quad (4.9)$$

$$\frac{d\rho_d(t)}{dt} = -R'_0\rho_d(t) + ((1 - p)\gamma + R'_0)\rho_e(t). \quad (4.10)$$

The time evolution of the excited state is given by

$$p_e(t) = \frac{2R'_0 e^{-t(\gamma+2R'_0)/2}}{\sqrt{(\gamma+2R'_0)^2 - 4p\gamma R'_0}} \sinh\left(\frac{t}{2}\sqrt{(\gamma+2R'_0)^2 - 4p\gamma R'_0}\right). \quad (4.11)$$

At low saturation  $R'_0 \ll 1$  we have

$$\rho_e(t) = \frac{R'_0}{\gamma} e^{-pR'_0 t}. \quad (4.12)$$

Eventually, the ion will be in the ground state  $|g\rangle$  as  $t \rightarrow \infty$ . The number of photons emitted from the transition  $|e\rangle \rightarrow |g\rangle$  is precisely the population in the ground state. Hence, the average number of photons emitted is given by

$$N'(T) = \rho_g(t = T) = p\gamma \int_0^T \rho_e(t) dt = 1 - e^{-pR'_0 T}. \quad (4.13)$$

At small detection duration  $T$ , we have

$$N'(T) \approx pR'_0 T \left(1 - \frac{pR'_0 T}{2} + \dots\right), \quad (4.14)$$

which suggests that the number of photons emitted from  $|e\rangle$  to  $|g\rangle$  is directly proportional to the coupling rate  $R'_0$  of the probe laser.

We would like to point out that while Eq. (4.7) and (4.14) result from using a low intensity approximation, both  $R_0$  and  $R'_0$  can be solved directly from Eq. (4.6) and (4.13). For example, from Eq. (4.6), we have

$$R_0 = -\frac{1}{(1-p)T} \ln(1 - N(T)(1-p)). \quad (4.15)$$

In this case we need to know the number of photons scattered  $N(T)$  which can be calculated from the detection efficiency  $\epsilon$ . As we will see in Chapter 5, we can measure the detection efficiency by the photons counting method when the ion population is transferred back from the dark state to the ground state through the excited state ( $|d\rangle \rightarrow |e\rangle \rightarrow |g\rangle$ ).

#### 4.2.2 Spectroscopy on dipole transitions with fast laser switching

We apply the scheme described above to perform spectroscopy of the  ${}^2S_{1/2} \rightarrow {}^2P_{1/2}$  and  ${}^2D_{3/2} \rightarrow {}^2P_{1/2}$  transitions for  ${}^{40}\text{Ca}^+$ . Experimentally, we have a probe laser beam which addresses the transition we want to measure. Then we have to transfer the ions back to the appropriate initial state using the so-called “reset” beam. For the  ${}^2S_{1/2} \rightarrow {}^2P_{1/2}$  transition, the probe beam is the laser light at 397 nm and the reset beam is the laser light at 866 nm. For the  ${}^2D_{3/2} \rightarrow {}^2P_{1/2}$  transition, the roles of the laser beams are reversed. Typical fluorescence counts collected from 7-8 ions after  $\sim 10^6$  iterations are shown in Fig. 4-2. We can see from Fig. 4-2 that the fluorescence during the probing duration is approximately constant due to a short probing duration. Experimentally, we use a probe duration of 2  $\mu\text{s}$  and the reset duration of 10  $\mu\text{s}$ .

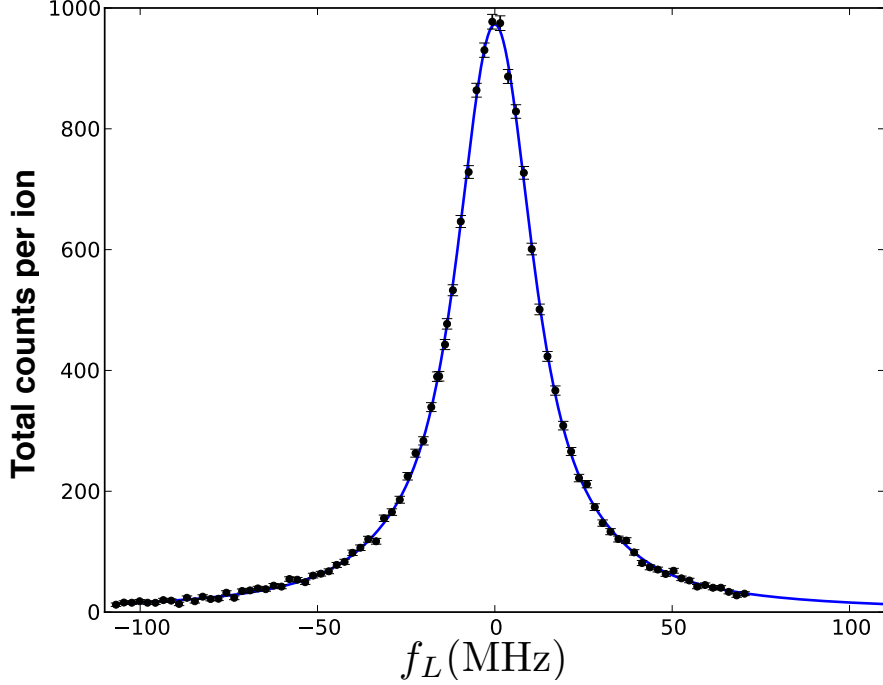


Figure 4-3: The fluorescence spectrum of the  $^2\text{S}_{1/2} \rightarrow ^2\text{P}_{1/2}$  transition for  ${}^{40}\text{Ca}^+$  as the frequency of the laser,  $f_L$ , is scanned across the transition. This data is collected from a crystal of 7 ions after  $10^6$  measurement cycles for each data point.

Since the probe laser can heat up the ions by the Doppler heating effect especially when the probe laser is blue-detuned from the atomic transition, we interleave a Doppler cooling period of about 1 ms once every 50 iterations of the probe cycle. The resulting spectra of the  $^2\text{S}_{1/2} \rightarrow ^2\text{P}_{1/2}$  and the  $^2\text{D}_{3/2} \rightarrow ^2\text{P}_{1/2}$  transitions are shown in Fig. 4-3 and 4-5, respectively. The solid lines are theoretical fits with the effect of micromotion included. (The model is described in details in the next section.) From the fit, the line-center can be determined with a precision of  $\sim 200$  kHz. Each data point is taken with  $10^6$  iterations of probing. The whole frequency scan takes about 10 minutes to complete. The error-bars include the Poissionian counting statistics and uncertainty in the laser power, which is approximately 1-2%.

## 4.3 Micromotion modulated spectra

We now apply the experimental scheme discuss in the precious section to observing the effects of micromotion on the spectra of dipole transitions in  ${}^{40}\text{Ca}^+$ .

### 4.3.1 Micromotion spectra at different trap frequencies

If there is a static stray electric field,  $\vec{E}_s$ , in the trapping region, the ions are displaced from the RF null of the potential generated by the trap electrodes. This causes the so-

called “excess” micromotion, which is micromotion in addition to the fundamentally unavoidable micromotion from the trapping mechanism described in Section 2.1.

We again follow [31] to analyze the effect of the stray electric field. With a static electric field  $\vec{E}_s$  applied to the ions, the equations of motion become

$$\ddot{u}_i + (a_i + 2q_i \sin(\Omega_D t)) \frac{\Omega_D^2}{4} u_i = \frac{Q \vec{E}_s \cdot \hat{u}_i}{m}, \quad (4.16)$$

where  $Q$  is the electrical charge of the ions. The lowest-order solution is given by

$$u_i \approx (u'_i + u_{0i} \cos(\omega_i t + \delta_i)) \left(1 + \frac{q_i}{2} \sin(\Omega_D t)\right), \quad (4.17)$$

where

$$u'_i = \frac{4Q \vec{E}_s \cdot \hat{u}_i}{m(a_i + q_i^2/2) \Omega_D^2}. \quad (4.18)$$

Compared to Eq. (2.16), the stray electric field induces an additional motion which oscillates at the drive frequency  $\Omega_D$ . The amplitude of this additional “excess” micromotion is directly proportional to the amplitude of the stray electric field.

Now we want see the effect of the excess micromotion on the fluorescence spectrum. Due to the Doppler shift, the electric field of the laser light seen by an ion in a trap is given by

$$E(t) = \text{Re} \left[ E_0 e^{i(\vec{k} \cdot (\vec{u}_0 + \vec{u}') - \omega_{\text{laser}} t)} \right], \quad (4.19)$$

where  $E_0$  is the amplitude of the laser field,  $\vec{k}$  is the wavevector of the laser and  $\omega_{\text{laser}}$  is the frequency of the laser. We can write

$$\vec{k} \cdot \vec{u}' = \beta \cos(\Omega_D t + \phi_m), \quad (4.20)$$

where  $\phi_m$  is the phase associated with the micromotion and  $\beta$  is the micromotion modulation index given by

$$\beta = \sqrt{\left( \frac{1}{2} (k_x u'_x q_x + k_y u'_y q_y) \right)^2 + C}, \quad (4.21)$$

where  $C$  accounts for any additional micromotion caused by a phase difference between the potentials on the trap RF electrodes or micromotion from the axial direction. With Eq. (4.20), we can write the electric field in Eq. (4.19) as

$$E(t) = \text{Re} \left[ E_0 e^{i\beta \cos(\Omega_D t + \phi_m)} e^{i(\vec{k} \cdot \vec{u}_0 - \omega_{\text{laser}} t)} \right]. \quad (4.22)$$

To completely see the effect of the this laser field on the fluorescence spectrum, we have to solve the optical Bloch equations. However, in a limit of a low saturation

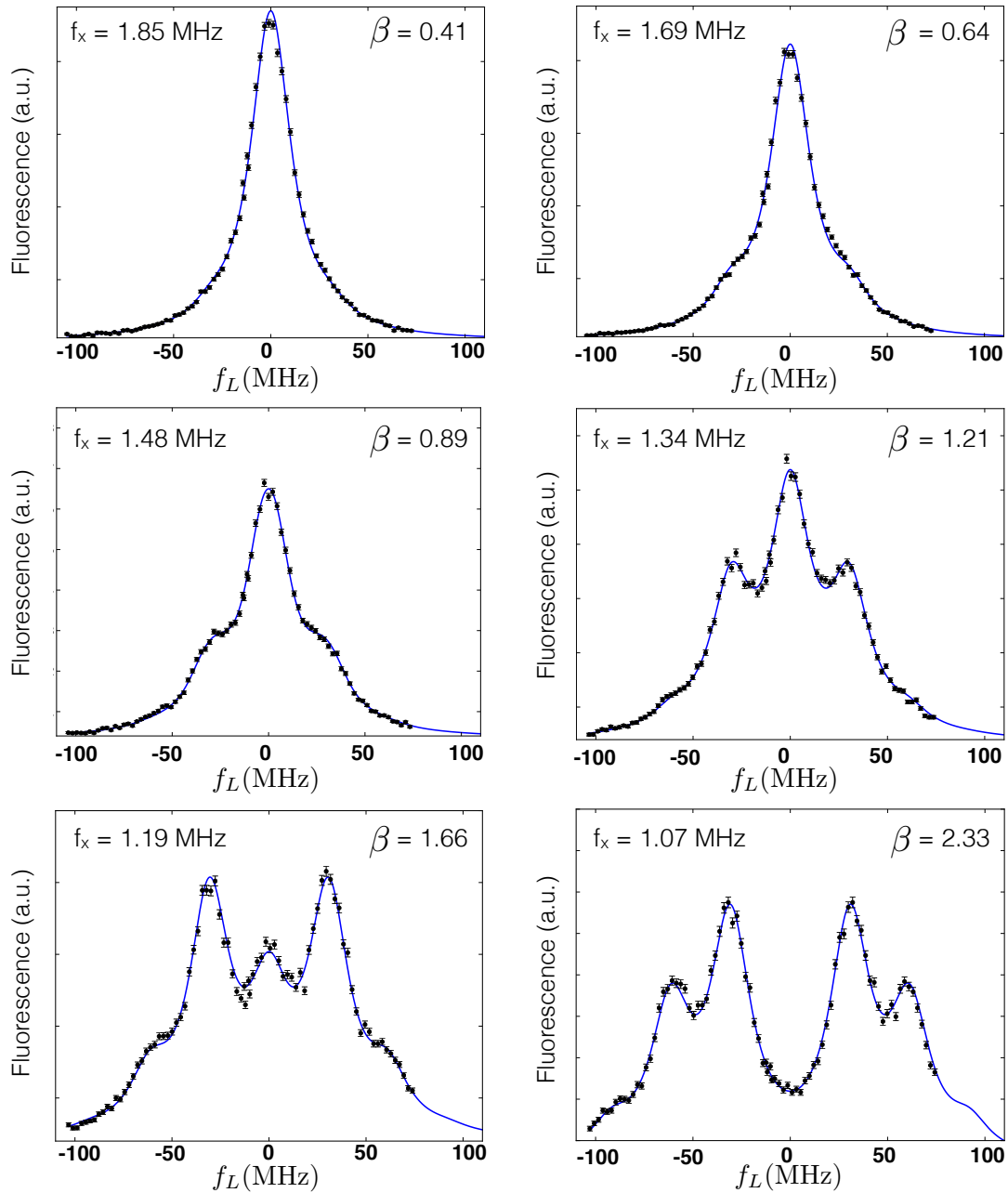


Figure 4-4: Micromotion modulated fluorescence spectra of the  $S_{1/2} \rightarrow P_{1/2}$  transition for  $^{40}\text{Ca}^+$  at different modulation indices,  $\beta$ , due to different trap frequencies.

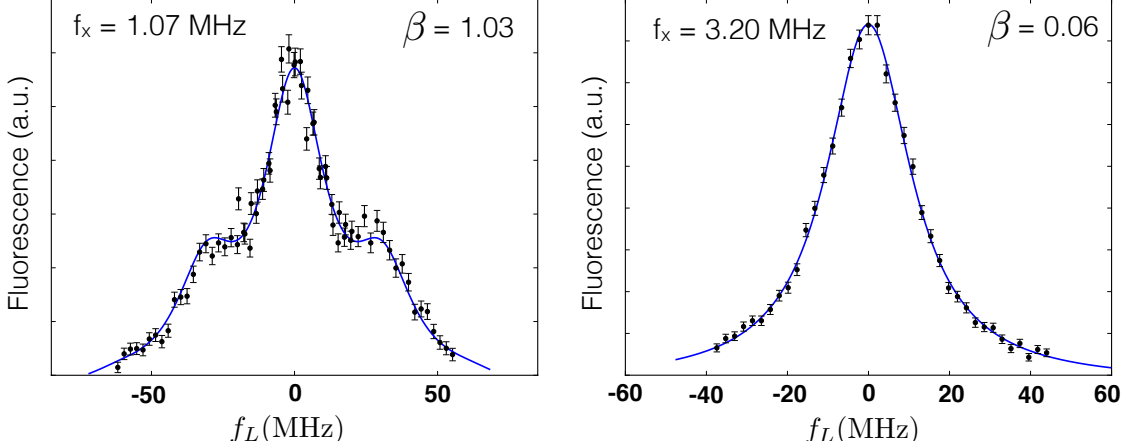


Figure 4-5: Micromotion modulated fluorescence spectra of the  $D_{3/2} \rightarrow P_{1/2}$  transition for  $^{40}\text{Ca}^+$  at high and low modulation index  $\beta$  due to different trap frequencies.

parameter, we can use the Bessel functions expansion

$$e^{i\beta \cos(\Omega_D t + \phi_m)} = \sum_{n=-\infty}^{\infty} J_n(\beta) e^{in(\Omega_D t + \phi_m + \pi/2)}, \quad (4.23)$$

where  $J_n$  is the  $n$ -th order Bessel function. We then solve the Bloch equations for each individual laser frequency of different micromotion sidebands. The resulting fluorescence spectrum is given by

$$P \propto |E_0|^2 \sum_{n=-\infty}^{\infty} \frac{J_n^2(\beta)}{(\delta + n\Omega_D)^2 + (\gamma/2)^2}, \quad (4.24)$$

where  $\delta$  is the detuning of the laser from the atomic transition frequency. We measure the fluorescence spectra of the  $^2S_{1/2}-^2P_{1/2}$  and  $^2D_{3/2}-^2P_{1/2}$  transitions for  $^{40}\text{Ca}^+$  at different trap frequencies, which are displayed in Fig. 4-4 and 4-5. We can see prominent peaks at the multiple of the drive frequency  $\Omega_D \sim 2\pi \times 30.7$  MHz for various values of  $\beta$ .

To see more clearly the dependence of  $\beta$  on the trap frequency, we rewrite Eq. (4.21) as

$$\beta = \sqrt{\frac{1}{\lambda_L^2 \Omega_D^4} \left( \frac{A}{f_x^2} + \frac{B}{f_y^2} \right)^2 + C}, \quad (4.25)$$

where  $f_x$  and  $f_y$  are the two radial trap frequencies and  $\lambda_L$  is the wavelength of the laser light. We change the value of the radial trap frequency by changing the RF power applied to the trap electrodes. However, we did not change  $f_x$  and  $f_y$  independently

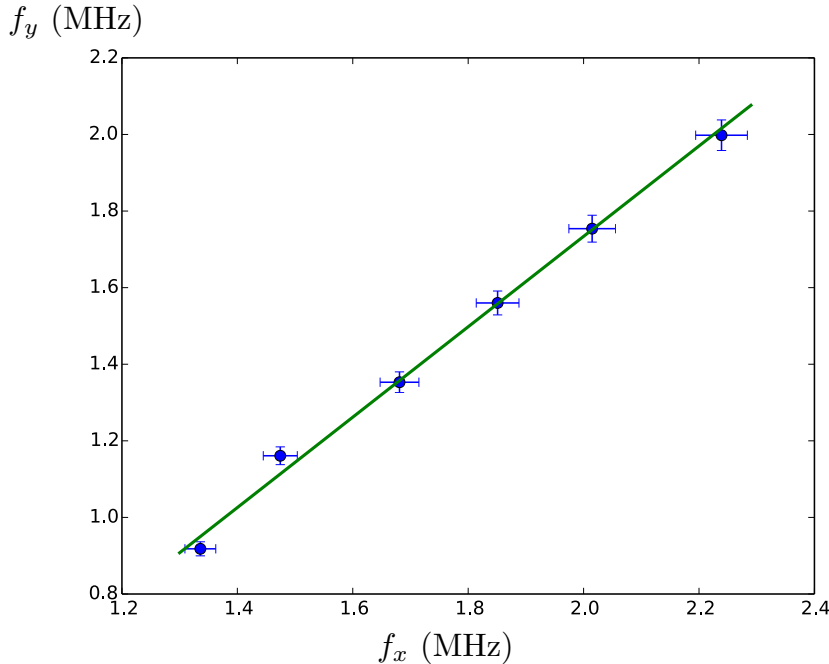


Figure 4-6: Relationship between the two radial trap frequencies,  $f_x$  and  $f_y$ . The linear fit gives  $f_y = 1.18(4) \cdot f_x - 0.63(8)$  (MHz).

from each other. The relationship between the two radial trap frequencies<sup>1</sup> as we change the RF power is shown in Fig. 4-6, with a resulting linear fit given by

$$f_y = 1.18(4) \cdot f_x - 0.63(8) \text{ (MHz).} \quad (4.26)$$

With this, we can plot the dependence of  $\beta$ , which is obtained by fitting the spectra in Fig. 4-4, on the trap frequency,  $f_x$ , as shown in Fig. 4-7. The solid line is a fit according to Eq. (4.25). The fit reveals that  $(A, B) = (1.1 \pm 0.6, 1.0 \pm 0.4) \times 10^7 \text{ nm} \cdot \text{MHz}^4$  and  $C = 0.00(3)$  with a reduced chi-squared of  $\chi_{\text{red}}^2 \approx 1.06$ . The value of  $C$  suggests that the effect from the phase difference of the potentials on the trap electrodes is small.

Another interesting observation can be made regarding the dependence of  $\beta$  on the laser wavelength. At the trap frequency of  $f_x = 1.07$  MHz, the spectra of the  ${}^2\text{D}_{3/2} \rightarrow {}^2\text{P}_{1/2}$  and  ${}^2\text{S}_{1/2} \rightarrow {}^2\text{P}_{1/2}$  transitions yield the modulation indices to be  $\beta_{866} = 1.04(5)$  and  $\beta_{397} = 2.31(5)$ . The ratio  $\beta_{397}/\beta_{866} = 2.22(12)$  is consistent with the ratio of the laser wavelengths  $\lambda_{866}/\lambda_{397} \approx 2.18$  according to Eq. (4.25). The modulation index is higher for shorter wavelength because of the relative amount of Doppler shift of the laser light seen by the ion. One can also view this dependence as a result of different Lamb-Dicke parameters.

---

<sup>1</sup>We measure the trap frequencies by the pulse excitation method similar to the one used in [23].

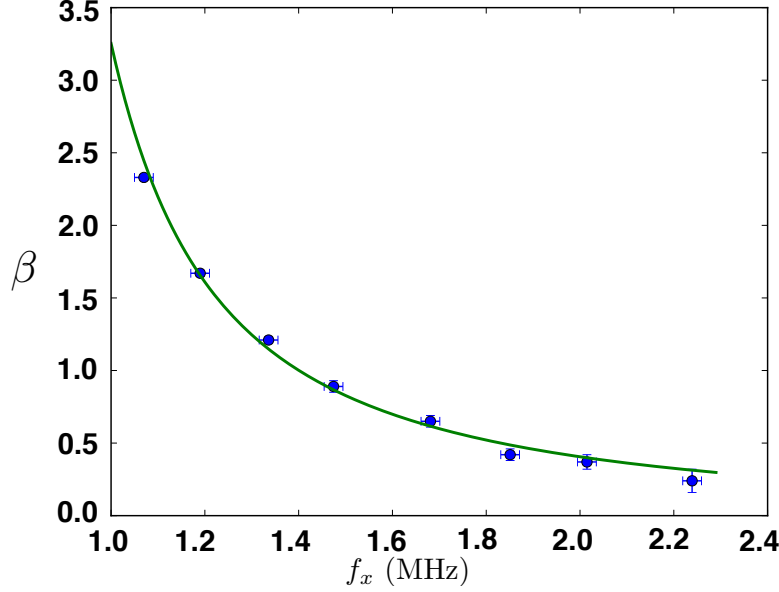


Figure 4-7: Micromotion modulation index,  $\beta$ , measured as a function of trap frequency,  $f_x$ .

### 4.3.2 Spectral modulation due to intensity gradient

If a tightly focused probe laser beam is displaced from the ions, micromotion leads to amplitude modulation of the laser light. This allows us to detect micromotion perpendicular to the laser axis.

For the mathematical description, we write the laser light intensity gradient as  $\vec{\nabla} \cdot E$ . Now the electric field of the laser seen by the ions is given by

$$E(t) = \text{Re} [E_0(1 + \beta' \cos(\Omega_D t + \phi'_m)) e^{i(\beta \cos(\Omega_D t + \phi_m) - \omega_L t + \phi_L)}], \quad (4.27)$$

with  $\beta' = \vec{u}' \cdot \vec{\nabla} E / E_0$ . Again, we use the Bessel functions expansion and obtain

$$\begin{aligned} E(t) = E_0(1 + \beta' \cos(\Omega_D t + \phi'_m)) \times \\ \sum_{n=-\infty}^{\infty} J_n(\beta) \cos \left( n(\Omega_D t + \phi_m + \frac{\pi}{2}) - \omega_L t + \phi_L \right). \end{aligned} \quad (4.28)$$

We explicitly evaluate this expression:

$$\begin{aligned} \frac{E(t)}{E_0} = & \sum_{n=-\infty}^{\infty} J_n(\beta) \cos \left( n(\Omega_D t + \phi_m + \frac{\pi}{2}) - \omega_L t + \phi_L \right) + \\ & \beta' \sum_{n=\infty}^{\infty} J_n(\beta) \left[ \cos(\Omega_D t + \phi'_m) \cos \left( n(\Omega_D t + \phi_m + \frac{\pi}{2}) - \omega_L t + \phi_L \right) \right]. \end{aligned} \quad (4.29)$$

Since  $\phi_m = \phi'_m$ , we use the trigonometric identity

$$\cos A \cos B = \frac{\cos(A - B) + \cos(A + B)}{2}, \quad (4.30)$$

and the second term of the RHS in Eq. (4.29) becomes

$$\begin{aligned} \beta' \sum_{n=-\infty}^{\infty} J_n(\beta) & \left[ \cos(\Omega_D t) \cos \left( n(\Omega_D t + \phi_m + \frac{\pi}{2}) - \omega_L t + \phi_L \right) \right] \\ &= \frac{\beta'}{2} \sum_{n=-\infty}^{\infty} J_n(\beta) \left[ \cos \left( n(\Omega_D t + \phi_m + \frac{\pi}{2}) - \omega_L t + \phi_L - \Omega_D t \right) \right] + \\ & \quad \frac{\beta'}{2} \sum_{n=-\infty}^{\infty} J_n(\beta) \left[ \cos \left( n(\Omega_D t + \phi_m + \frac{\pi}{2}) - \omega_L t + \phi_L + \Omega_D t \right) \right] \end{aligned} \quad (4.31)$$

$$= \frac{\beta'}{2} \sum_{n=-\infty}^{\infty} (J_{n+1}(\beta) - J_{n-1}(\beta)) \left[ \sin \left( n(\Omega_D t + \phi_m + \frac{\pi}{2}) - \omega_L t + \phi_L \right) \right]. \quad (4.32)$$

The electric field now becomes

$$\begin{aligned} \frac{E(t)}{E_0} &= \sum_{n=-\infty}^{\infty} J_n(\beta) \cos \left( n(\Omega_D t + \phi_m + \frac{\pi}{2}) - \omega_L t + \phi_L \right) + \\ & \quad \frac{\beta'}{2} \sum_{n=-\infty}^{\infty} (J_{n+1}(\beta) - J_{n-1}(\beta)) \left( \sin \left( n(\Omega_D t + \phi_m + \frac{\pi}{2}) - \omega_L t + \phi_L \right) \right) \end{aligned} \quad (4.33)$$

$$\begin{aligned} &= \sum_{n=-\infty}^{\infty} \sqrt{J_n^2(\beta) + \frac{\beta'^2}{4} (J_{n+1}(\beta) - J_{n-1}(\beta))^2} \times \\ & \quad \left( \sin \left( n(\Omega_D t + \phi_m + \frac{\pi}{2}) - \omega_L t + \phi_L + \psi(n) \right) \right), \end{aligned} \quad (4.34)$$

where  $\psi(n)$  is the phase given by

$$\psi(n) = \tan^{-1} \left( \frac{2J_n(\beta)}{\beta'(J_{n+1}(\beta) - J_{n-1}(\beta))} \right) \quad (4.35)$$

Analogous to Eq. (4.24), the fluorescence spectrum of the ions is given by

$$P \propto \|E_0\|^2 \sum_{n=-\infty}^{\infty} \frac{J_n^2(\beta) + \frac{\beta'^2}{4} (J_{n+1}(\beta) - J_{n-1}(\beta))^2}{(\delta + n\Omega_D)^2 + (\gamma/2)^2}. \quad (4.36)$$

Using an identity for the Bessel functions,

$$J'_n(\beta) = \frac{\partial J_n(\beta)}{\partial \beta} = \frac{J_{n-1}(\beta) - J_{n+1}(\beta)}{2}, \quad (4.37)$$

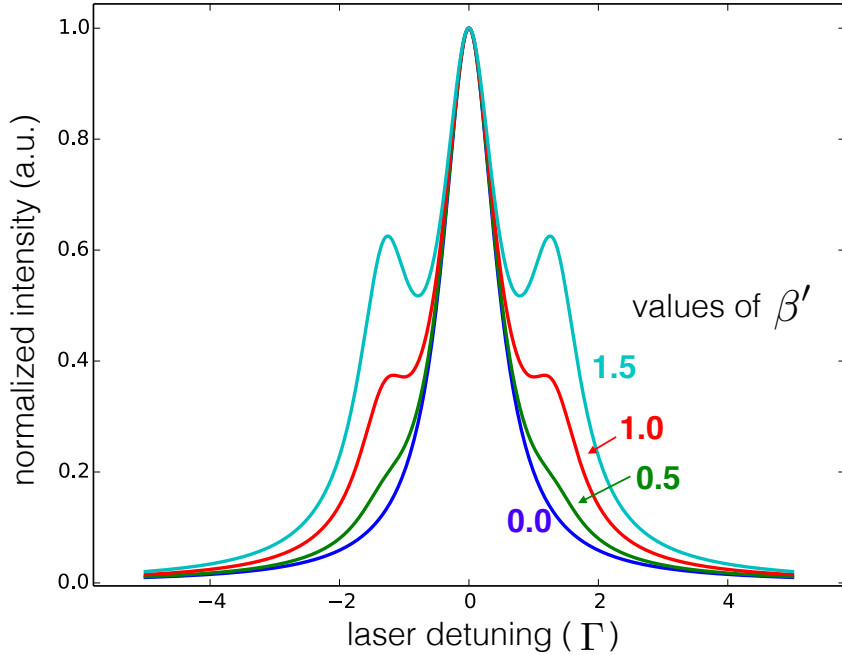


Figure 4-8: Effect of laser light intensity gradient,  $\beta'$ , on the simulated fluorescence spectra with  $\beta = 0$ . The micromotion sideband at  $\Omega_D = 1.3\Gamma$  is clearly visible for larger values of  $\beta'$ . Note that only first-order sidebands are present because the modulation is only from the intensity of the laser.

we have

$$P \propto \|E_0\|^2 \sum_{n=-\infty}^{\infty} \frac{J_n^2(\beta) + \beta'^2(J'_n(\beta))^2}{(\delta + n\Omega_D)^2 + (\gamma/2)^2}. \quad (4.38)$$

To see how the intensity gradient influences the fluorescence spectrum, consider a situation where there is no micromotion in the direction of the laser light ( $\beta = 0$ ). If there is no intensity modulation, the spectrum has no sideband since  $J_n(0) = 0$  for  $n \neq 0$ . However, if there is a finite intensity gradient ( $\beta' \neq 0$ ), there will be sidebands at  $n = \pm 1$  since  $J'_{n=\pm 1}(0) = \pm 1/2$  but no sideband at higher orders. Figure 4-8 shows simulated spectra with this effect at different values of  $\beta'$  for  $\beta = 0$ , which shows no sideband of order higher than the first order. On the other hand, if there is micromotion in the direction of the laser light, higher order sidebands become visible, as shown in Figure 4-9 for  $\beta = 1.0$ . The distinction between these two line-shapes allow us to experimentally compensate micromotion in the direction both perpendicular to the laser light direction (from intensity gradient) and along the laser light direction.

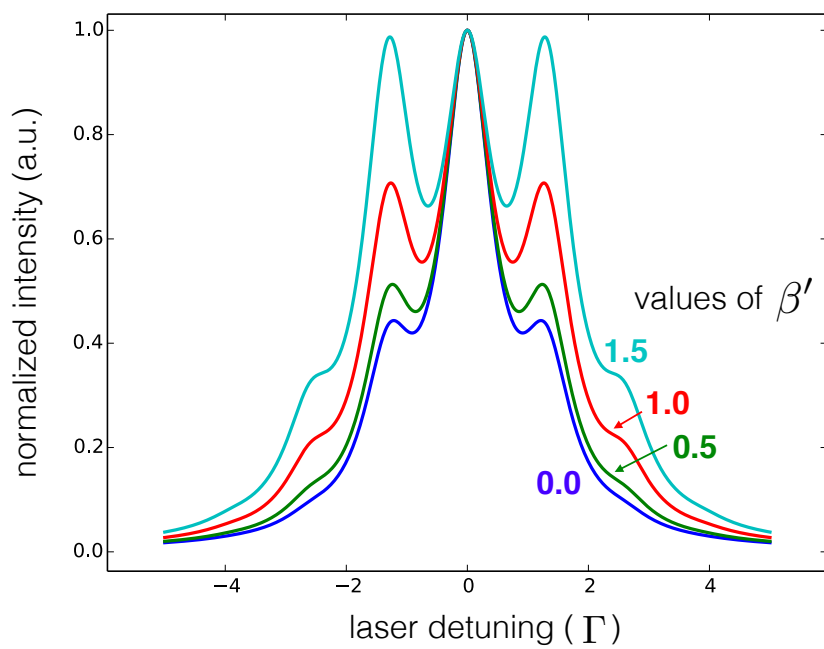


Figure 4-9: Effect of laser light intensity gradient,  $\beta'$ , on the simulated fluorescence spectra with  $\beta = 1.0$ . Higher order sidebands are from the micromotion in the laser direction. They are due to the Doppler effect and not the intensity gradient.

# Chapter 5

## Measurement of branching fraction

An excited atomic state usually has multiple decay channels. For example the excited  $^2P_{1/2}$  state of  $^{40}\text{Ca}^+$  can decay to either the ground  $^2S_{1/2}$  state or the metastable  $^2D_{3/2}$ . Each decay channel has a fixed probability, called the branching fraction of this channel. Branching fractions of atomic states depend on the atomic structure and how each transition couples to the background vacuum field. Theoretical calculations of the branching fractions for complex atoms are demanding and theorists usually have to resort to many kinds of approximations [49, 50, 51, 52]. Comparing these calculated values to precisely measurements provides a good estimate on the accuracy of the models used in the calculations.

There have been a few measurements of the branching fractions of trapped ions. The method by Gerritsma *et al.* [53], which is applied to measuring the branching fractions of  $^{40}\text{Ca}^+$  for the excited  $^2P_{3/2}$  state, utilizes a narrowband laser at 729 nm for state readouts and preparations. However, this method is not applicable to the decay of the  $^2P_{1/2}$  state since it requires at least three decay channels. The scheme by Kurz *et al.* [54], which uses an ultra-fast laser pulse to measure the branching fraction of the  $^2P_{3/2}$  state for  $\text{Ba}^+$ , is applicable to the  $^2P_{1/2}$  state for  $^{40}\text{Ca}^+$ . However, the requirement of an ultra-fast laser complicates the experimental setup and introduces additional systematic errors. In this chapter, we present a simple experimental scheme to measure the branching fractions of the two decay channels of the excited state of  $^{40}\text{Ca}^+$  in the  $J = 1/2$  manifold. We then compare the measurement result to the theoretical calculations in the literature.

### 5.1 Measurement of branching fractions based on photon counting

#### 5.1.1 Theoretical considerations for measurement of branching fractions

We look again at atoms or ions with an energy level structure similar to the one shown in Fig. 4-1. The excited state  $|e\rangle$  can decay to either the ground state  $|g\rangle$  or the metastable state  $|d\rangle$  with probabilities of  $p$  and  $1 - p$ , respectively. Assume that

we have a single laser which couples the state  $|g\rangle$  to  $|e\rangle$ . We measure this parameter  $p$  by counting the number of photons emitted on the  $|e\rangle \rightarrow |g\rangle$  transition by the ions until the ions are trapped in the dark state  $|d\rangle$ . We then repump the ions from the  $|d\rangle$  state and the ion will emit exactly one photon on the  $|e\rangle \rightarrow |g\rangle$  transition, therefore allowing us to calibrate the detection efficiency.

The time evolution of the atomic populations can be calibrated by solving a set of rate equations similar to Eq. (4.1) to (4.3). However, those rate equations do not include the coherence between the ground state and the excited state induced by the laser. To fully capture this coherent effect, we use optical Bloch equations [48]. Those are given by

$$\dot{\rho}_{ee}(t) = \frac{i\Omega_L(t)}{2}(\rho_{eg}(t) - \rho_{ge}(t)) - \gamma\rho_{ee}(t) \quad (5.1)$$

$$\dot{\rho}_{gg}(t) = \frac{i\Omega_L(t)}{2}(\rho_{ge}(t) - \rho_{eg}(t)) + p\gamma\rho_{ee}(t) \quad (5.2)$$

$$\dot{\rho}_{eg}(t) = (i\delta(t) - \frac{\gamma}{2})\rho_{eg}(t) + \frac{i\Omega_L(t)}{2}(\rho_{ee}(t) - \rho_{gg}(t)) \quad (5.3)$$

$$\dot{\rho}_{dd}(t) = (1-p)\gamma\rho_{ee}(t), \quad (5.4)$$

where  $\Omega_L(t)$  is the Rabi frequency associated with the laser. Here we include explicitly the time dependence of both the laser intensity and detuning. In the rate equations in the previous chapter (Eq. (4.1) to (4.3)), we treat these parameters as fixed.

The mean number of photons scattered from the ions is given by

$$\langle n \rangle = \int_0^\infty \gamma\rho_{ee}(t)dt. \quad (5.5)$$

Substituting the expression for  $\rho_{ee}(t)$  from Eq. (5.4), we get

$$\langle n \rangle = \frac{1}{1-p} \int_0^\infty \dot{\rho}_{dd}(t)dt = \frac{1}{1-p}(\rho_{dd}(t \rightarrow \infty) - \rho_{dd}(t = 0)). \quad (5.6)$$

We know that as  $t \rightarrow \infty$  all the ions will be in  $|d\rangle$  and initially all the ions are in  $|g\rangle$ , substituting these boundary values yields

$$\langle n \rangle = \frac{1}{1-p}. \quad (5.7)$$

We see that  $\langle n \rangle$  does not depend on any time-variation in laser intensity and detuning.<sup>1</sup>

Before we proceed further, it is interesting to derive Eq. (5.7) from a probabilistic point of view. Since the excited state of the ion decays to the dark state with a probability  $1-p$ , the probability of the ion to be dark after one photon absorption is

---

<sup>1</sup>Note that this result still holds even if we consider all Zeeman sub-levels in the Bloch equations, as long as the laser is linearly polarized or we do not analyze the circular polarization of the emitted light. We prove this statement in Chapter 6.

$1 - p$ . The probability of the ion to be dark after  $n$  photon absorptions is  $p^{n-1}(1 - p)$ . The average number of photon absorptions is simply

$$\langle n \rangle = \sum_{n=0}^{\infty} = np^{n-1}(1 - p) = \frac{1}{1 - p}, \quad (5.8)$$

which agrees with the result derived from the Bloch equations above.

The last photon is emitted from the  $|e\rangle \rightarrow |d\rangle$  transition. The frequency of the photon from this transition is usually very different from the  $|e\rangle \rightarrow |g\rangle$  transition. Experimentally, we usually filter out the photons from the  $|e\rangle \rightarrow |d\rangle$  transition and detect only photons from the  $|e\rangle \rightarrow |g\rangle$  transition. (For  ${}^{40}\text{Ca}^+$ , we detect photons at 397 nm but not at 866 nm.) Then the number of photons detected is simply

$$\langle N \rangle = \langle n \rangle - 1 = \frac{p}{1 - p}. \quad (5.9)$$

Due to a finite detection efficiency,  $\epsilon$ , experimentally, we detect only a small fraction of the photon number,  $\epsilon\langle N \rangle$ . Once the ion is in the state  $|d\rangle$ , we can apply laser light that couples between  $|d\rangle$  and  $|e\rangle$  state (866 nm for  ${}^{40}\text{Ca}^+$ ) to bring the ion back to the ground state  $|g\rangle$ . During this process, the ion emits exactly one photon from the  $|e\rangle$  to  $|g\rangle$  transition before going back to  $|g\rangle$ , allowing us to measure  $\epsilon$  and calculate the branching fraction  $p$ .

### 5.1.2 Experimental procedure for measuring the branching fraction

In this section, we describe the experimental procedure to measure the branching fraction,  $p$ , for  ${}^{40}\text{Ca}^+$ . We start by preparing all ions in the ground state  $|g\rangle$ . Then we turn on the laser at 397 nm (called a pump pulse) and collect all the photons at 397 nm until all the ions are in  $|d\rangle$ . Since there is a finite detection efficiency,  $\epsilon$ , from losses in optical elements and a finite solid angle of the detector, the mean number of photons detected per ion is given by  $\epsilon\langle N \rangle$ . Once all the ions are in  $|d\rangle$ , the laser light at 397 nm is switched off. Next we switch on the laser light at 866 nm (called a reset pulse) to bring the ions back to the ground state. During this time, the mean number of photon at 397 nm detected is given by  $\epsilon$ . The pulse sequence described here is shown in Fig. 5-1.

We repeat this procedure for  $T$  times. The total number of photon at 397 nm detected during the pump pulse is given by  $N_b = \epsilon T \langle N \rangle$ . The total number of photon at 397 nm detected during the reset pulse is given by  $N_r = \epsilon T$ . Together with Eq. (5.9), we can write

$$p = \frac{N_b}{N_b + N_r}, \quad (5.10)$$

where the efficiency  $\epsilon$  drops out.

The timing of the pulse sequence we use is also shown in Fig. 5-1. Typically, after

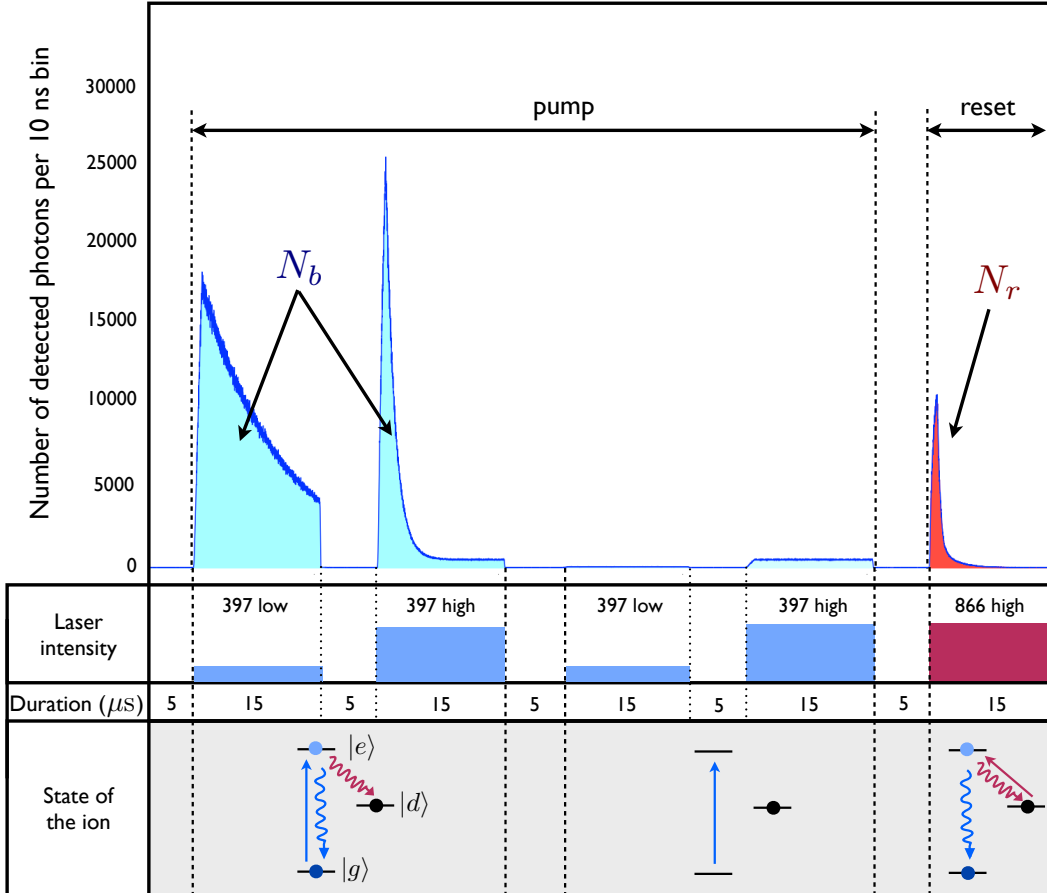


Figure 5-1: Pulse sequence for measuring the branching fraction. During the “pump” duration, the laser light at 397 nm is switched on to transfer the ion population to the state  $|d\rangle$ . The photons scattered from the ions during this duration is given by  $N_b$ . After the ions are in the state  $|d\rangle$ , we switch on the laser light at 866 nm to transfer the population back to the ground state  $|g\rangle$ . The 397 nm photons scattered during this “reset” is given by  $N_r$ . The branching fraction  $p$  can be calculated from  $p = N_b/N_b + N_r$ . For the “pump” duration, we switch on the laser light first with low intensity to keep the count rate low. The last two pulses are for determination of the background.

a few measurement cycles, we have to perform Doppler cooling to the ion crystal (which consists of 13 ions for this particular measurement) to keep the temperature close to the Doppler temperature. We perform roughly  $\sim 10^8$  probing cycles in 10 hours. The result we obtained is  $p = 0.93565(7)$ . The error is a combination of statistical and systematic errors as shown in Table 5.1.

## 5.2 Sources of uncertainties

**The Hanle effect and polarization dependence scattering rate.** The Hanle effect is the dependence of the polarization of the scattered photons on the polarization of the excitation laser and the magnetic field strength and orientation. If the Hanle effect is present in our system, the measured branching fraction using our method will be affected if the detection path has a bias toward any photon polarization.

However, the Hanle effect for the  $J = 1/2$  excited state is absent as long as the excitation laser light is linearly polarized and the detector does not distinguish photons with different circular polarizations [55]. The result is that the scattering rate of the ions from the 397 nm laser light is independent of both the magnitude and orientation of the applied magnetic field. However, the detection optics might be more efficient for a certain circular polarization than the other circular polarization due to birefringence in the optical elements. We check this experimentally by measuring  $p$  for different magnetic strengths and orientation, as shown in Fig. 5-2. We found no dependence of  $p$  on the magnetic field orientation within our measurement uncertainty. From this, we conclude that the Hanle effect will affect our branching fraction measurement by at most  $5 \times 10^{-5}$ .

**Finite AOMs extinction ratio.** Even when the AOM is off, there will be laser light leaking into the optical fiber and arrives at the ion. We measure the ratio of the light intensity that arrives at the ions between the AOM being on and off in our setup to be better than  $5 \times 10^{-6}$ . Any laser light at 866 nm present during the “probe” duration brings the ions back to the  $|g\rangle$  state. The ions then start to scatter the 397 nm light again. We estimate that this effect increases  $N_b$  by  $2 \times 10^{-5}$  for our laser power. The leakage of the 397 nm light during the “pump” 866 nm also increases  $N_r$  by  $7 \times 10^{-5}$ . These two uncertainties contribute less than  $5 \times 10^{-6}$  to the uncertainty of the branching fraction.

**Off-resonant excitation from the ground state to the  ${}^2\text{P}_{3/2}$  state.** Because the laser diode that produce the light at 397 nm for our experiment also contains a small amount of light at 393 nm, an ion at the ground state can get excited to the  ${}^2\text{P}_{3/2}$  state instead of the  ${}^2\text{P}_{1/2}$  state. We estimate an error due to this effect by observing how often the ions become dark during Doppler cooling. The estimated uncertainty of the branching fraction due to this effect is less than  $1 \times 10^{-6}$ .

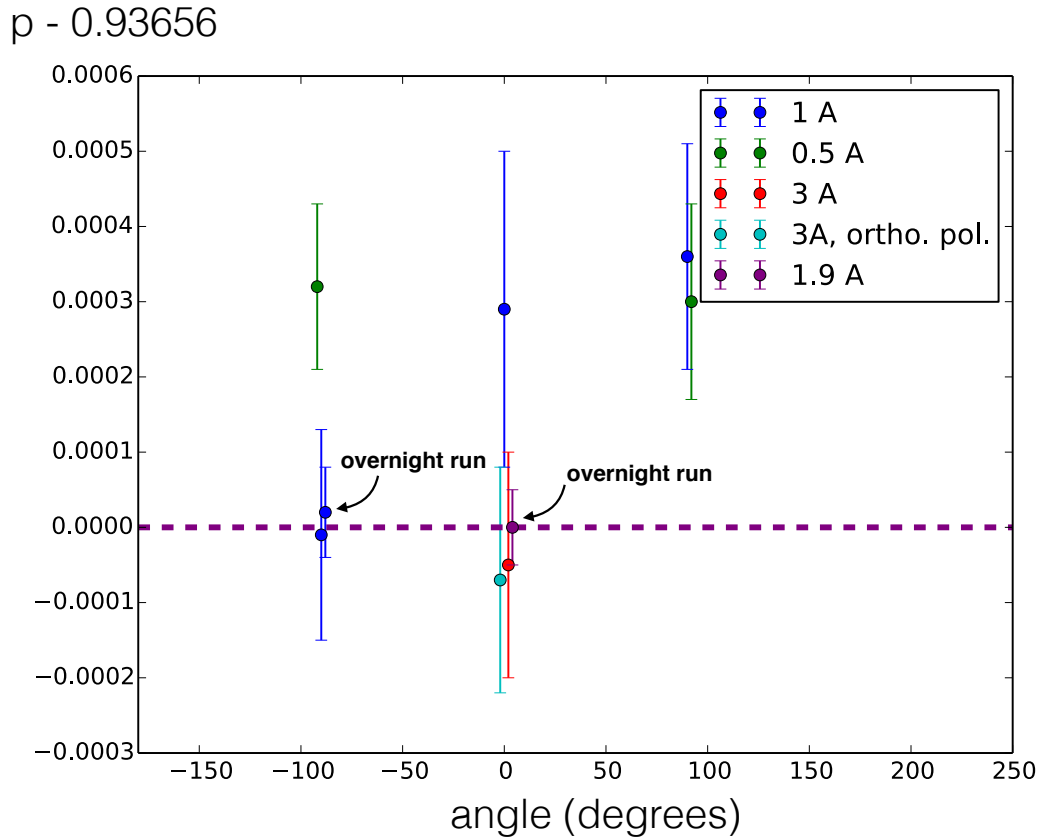


Figure 5-2: Branching fraction  $p$  measured for different magnetic field strengths and orientations. The legend shows the current applied to the magnetic coil with  $\sim 1$  G/A. The orientation is the angle of the magnetic field measured from the vertical axis of the experiment. The blue data point is taken with the polarization of the 397 nm laser rotated by  $90^\circ$ . The purple data point is our final measurement. The two overnight runs for magnetic field at different orientations confirm that the value of  $p$  does not change within our statistical uncertainty.

Effect	Shift	Error
Photon counting statistical error	-	$5 \times 10^{-5}$
Detection optics birefringence	-	$5 \times 10^{-5}$
PMT dead time	$7 \times 10^{-6}$	$3 \times 10^{-6}$
Lifetime of $3^2D_{3/2}$ State		$2 \times 10^{-6}$
Extinction ratio of AOMs	-	$5 \times 10^{-6}$
Off-resonant excitation to $4^2P_{3/2}$ state	$< 1 \times 10^{-6}$	-
Finite measurement duration	$15 \times 10^{-6}$	$6 \times 10^{-6}$
Total	$22 \times 10^{-6}$	$7 \times 10^{-5}$

Table 5.1: List of measurement uncertainties for the branching fraction of  ${}^{40}\text{Ca}^+$ .

**Finite dark time of the photo-multiplier tube (PMT).** There is a finite recovery time (or dead time) for the PMT after detecting a photon. Hence, if the count rate is too high, the PMT underestimates the count rate. To minimize this error, we have to keep the count rate as low as possible. This done by first turning on the 397 nm pump light at low intensity and then at high intensity, as shown in Fig. 5-1. Our PMT (Sens Tech® model P25PC) has a dead time of 16.5 ns. We estimate that the PMT dead time contributes  $7 \times 10^{-6}$  fractional shift with  $3 \times 10^{-6}$  fractional uncertainty to the uncertainty budget of the branching fraction.

**Finite lifetime of the dark state.** The  $D_{3/2}$  state of  ${}^{40}\text{Ca}^+$  (the state  $|d\rangle$  in the measurement scheme) has a natural lifetime of  $\sim 1.2$  seconds [33]. If the duration of the pump pulse is too long, the ion can decay from  $|d\rangle$  back to  $|g\rangle$  by spontaneous emission and starts to scatter again. We minimize this effect by shortening the pulse duration of the lasers. The pulse duration of 5-10  $\mu\text{s}$  is relatively short compared to the lifetime of the  $D_{3/2}$  state. We estimate that the finite lifetime of the  $D_{3/2}$  state contributes to the final result about  $2 \times 10^{-6}$  fractional error. On the other hand, we also rely on having the laser pulse long enough such that we are confident that all the ions are in  $|d\rangle$  at the end of the pump duration. Our pulse duration of 5-10  $\mu\text{s}$  contributes  $1.5 \times 10^{-5}$  fractional shift with  $6 \times 10^{-6}$  fractional error to the branching fraction.

**Counting statistical errors.** The measured values of both  $N_b$  and  $N_r$  are both described by the Poisson statistics. A simple error propagation of Eq. (5.10) gives

$$\frac{\delta p}{p} = \frac{N_r}{N_r + N_b} \sqrt{\left(\frac{\delta N_r}{N_r}\right)^2 + \left(\frac{\delta N_b}{N_b}\right)^2}. \quad (5.11)$$

After  $10^8$  experimental cycles, our measurement yields  $N_r \sim 2 \times 10^6$  and  $N_b \sim 3 \times 10^7$ . This results in  $\delta p/p \sim 5 \times 10^{-5}$ . The summary of all the uncertainties is given in Table 5.1.

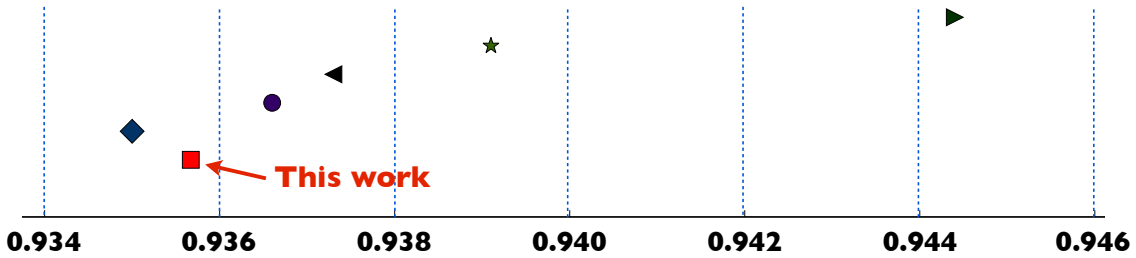


Figure 5-3: Measurement of the branching fraction compared to various theoretical calculations in the literature. Legend: (•, ▶) Liaw *et al.* [51], (★) Guet *et al.* [50], (◀) Sahoo *et al.* [49], (◆) Arora *et al.* [52]. The error bar of our experimental data is smaller than the size of the data point.

### 5.3 Measurement result and discussion

Our measurement yields  $p = 0.93565(7)$  for  ${}^{40}\text{Ca}^+$ . A comparison between this measured value and various theoretical values is shown in Fig. 5-3. Since the uncertainty of our measurement is small enough to distinguish between calculation models, our measured value can be used as a guideline for improvement of future theoretical works.

Because our experimental method only requires that the excited state decays to either a ground state or other metastable state, the measurement scheme can be readily applied to various atomic and ion species. In Au, there is work on both theory and experiment related to its atomic structure [56, 57, 58]. Other ions such as Sc $^{++}$  [59], Sr $^+$  [60, 61], Yb $^+$ , Ba $^+$ , Ra $^+$  [8, 62, 63, 64] and Hg $^+$  have excited states with  $J = 1/2$ . Some of these heavy ions are especially relevant in probing the parity non-conservation effect.

Our method is also applicable to excited states with  $J \neq 1/2$ , although the Hanle effect will affect the measurement more strongly than the case for  $J = 1/2$ . For example, the branching fractions of the excited  ${}^2\text{P}_{3/2}$  state of  ${}^{40}\text{Ca}^+$  (with the energy level shown in Fig. 5-4) can be measured this way if we do not have a narrow linewidth 729 nm laser. Analogous to the scheme presented in the previous section, the idea is to have additional repumping lasers to selectively turn off any decay channel. Specifically, the experimental procedure is the following:

1. We measure the number of blue photons,  $N_{393}$ , (at 393 nm) with only the 393 nm laser on. As in Eq. (5.9), we have

$$N_{393} = \frac{\epsilon e T}{1 - p}, \quad (5.12)$$

where  $\epsilon$  is the detection efficiency and  $T$  is the number of the probe cycles.

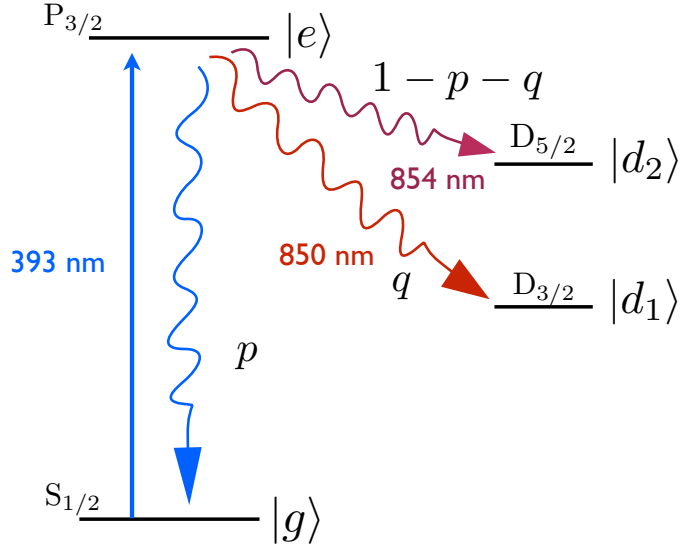


Figure 5-4: Energy diagram involving the excited  $^2P_{3/2}$  state which has three decay channels.

2. We measure the number of the blue photons with both the 393 nm and 850 nm lasers on. To avoid the complication of dark resonances, we alternate the 393 nm and 850 nm laser for the “pump” pulses until ions are in the  $|d_2\rangle$  state. The number of photons measured is given by

$$N_{393,850} = \frac{(p+q)\epsilon T}{1-p-q}. \quad (5.13)$$

3. Instead of the previous step, we can instead measure the number of the blue photons with both the 393 nm and 850 nm lasers on. In this case, we have

$$N_{393,854} = \frac{(1-q)\epsilon T}{q}. \quad (5.14)$$

4. For each probe cycle, the “reset” pulses consist of having both 866 nm and 850 nm lasers on. The number of blue photons during the “reset” pulses is given by

$$N_{850,854} = \epsilon T. \quad (5.15)$$

5. The value of the branching fractions are then given by

$$p = \frac{N_{393}}{N_{393} + N_{850,854}} \quad \text{and} \quad q = \frac{N_{850,854}}{N_{850,854} + N_{393,854}}. \quad (5.16)$$

It is important to note that for the excited  $^2P_{3/2}$  state, we are more sensitive to the Hanle effect compared to the case of excited  $^2P_{1/2}$  state. There will be a dependence of the measured photon number on the direction of the linear polarization of the excitation lasers and the orientation of the optics along the detection path.<sup>2</sup> However, a careful characterization of the optics and laser polarization should allow us to measure both  $p$  and  $q$  at the same level of precision as shown for the  $^2P_{1/2}$  state.<sup>3</sup>

---

<sup>2</sup>Most dielectric mirrors have different reflectivity between the  $s$  and  $p$  polarizations of the incident beam.

<sup>3</sup>The level of control over the laser polarization required to achieve  $10^{-5}$  precision in the branching fraction for the  $^2P_{3/2}$  state depends on the strength of the magnetic field. For  $^{40}\text{Ca}^+$ , at magnetic field strength around 1 G, the laser polarization must be controlled to better than  $10^{-3}$  level.

# Chapter 6

## Observation of the Hanle effect with trapped ions

Measuring the linewidth of the atomic dipole transition (or equivalently the lifetime of the excited state) with high precision is one of the most challenging task in atomic physics. This is because the atomic excited state is extremely sensitive to the environment. Any small perturbation is likely to induce the decay of the excited state to the ground state, effectively shortening the measured lifetime. There are also many line broadening mechanisms (such as Doppler and power broadenings) that contribute to the systematic uncertainty when performing spectroscopy on trapped atoms and ions. For  $^{40}\text{Ca}^+$ , the best measurement of the lifetime of the excited  ${}^2\text{P}_{1/2}$  state is  $7.10 \pm 0.02$  ns by Jin *et al.* using the method of collinear ion-beam spectroscopy [26]. This measured value currently disagrees with the calculated value of  $6.88 \pm 0.06$  ns by Safranova *et al.* by almost 4 standard deviations [27]. It is then beneficial to provide additional measurements to resolve this discrepancy.

One experimental technique that experimentalists have been using to measure the lifetimes of the atomic excited states for many decades is the Hanle effect. A precession of an atomic dipole moment in a magnetic field provide a fluorescence signal that depends on the strength of the magnetic field and the atomic lifetime. Since we can use the ion itself as a magnetic field probe, it seems feasible to use this scheme to improve the precision of the measured lifetime of the  ${}^2\text{P}_{1/2}$  state for  $^{40}\text{Ca}^+$ . In this chapter we survey an experimental scheme to measure the lifetime of the excited state of  $^{40}\text{Ca}^+$  using the Hanle effect. We present a detailed theoretical analysis for various experimental configurations.

### 6.1 Introduction to the Hanle effect

The observation of the Hanle effect, which was a main part of Wilhelm Hanle's Ph. D. thesis in 1922, is one of the very first atomic physics experiments that helped develop the structure and understanding of quantum physics. Hanle studied the dependence of the light intensity and polarization emitted from excited atoms in the presence of a strong static magnetic field. He found that by detecting only a certain

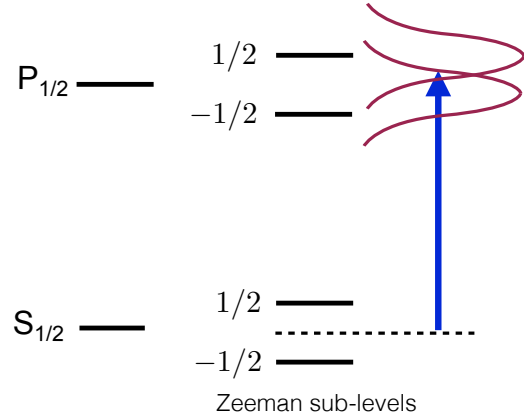


Figure 6-1: Condition for creating coherence in the excited states. The energy splitting of the excited states should be comparable to the linewidth of the transition.

polarization of the light emitted from the atoms, the measured light intensity depends strongly on the magnitude and direction of the applied magnetic field [65]. Classically, we can describe the Hanle effect as a precession of the atomic dipole moment in a magnetic field. Since the orientation of the dipole determines the polarization of the light emitted, as the dipole precesses, the polarization of the light also changes as a function of time. However, the excited state eventually decays back to the ground state. It turns out that the intensity of the light of certain polarization is maximized when the precession period coincides with the lifetime of the excited state. Relying on this fact, experimentalists have been using the Hanle effect to measure the lifetime of the excited states for many decades [66, 67, 68].

### 6.1.1 Coherence in the excited state

In the point of view of quantum mechanics, the Hanle effect (or level-crossing spectroscopy) arises from the coherence in the excited states [69, 70, 71]. If the spacing between different excited states is comparable to the linewidth of the transition, then the coherence in the excited states can be created by simultaneously exciting them using optical radiation, as shown in Fig. 6-1. This condition is usually met by means of the Zeeman splitting of the excited state (which is about 1-2 MHz per 1 Gauss of applied magnetic field). This is comparable to the linewidth of dipole allowed transition, which is usually in the order of a few MHz. After the excitation, the coherence or the superposition of the excited states evolves according to the difference between the populated energy eigenstates. This can be done by performing measurements in the basis different from the eigenbasis of the system.

To analyze the Hanle effect in more detail, consider a superposition of states created in a way illustrated in Fig. 6-1. An excitation to both excited states simulta-

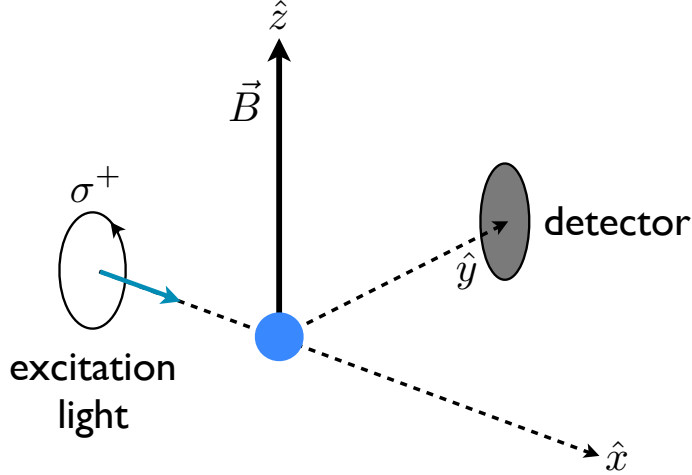


Figure 6-2: Typical experimental setup to observe the Hanle effect. Excitation light propagates perpendicular to the magnetic field. Circularly polarized light can excite both excited state simultaneously, creating a superposition state. The detector is placed in the direction perpendicular to both the magnetic field direction and the excitation light direction. The detector only detects a certain circular polarization.

neously can be realized by having circularly polarized light propagating perpendicular to the quantization axis set by the magnetic field, as shown in Fig. 6-2. The state right after the excitation is given by

$$|\Psi\rangle = a |\uparrow\rangle + b |\downarrow\rangle, \quad (6.1)$$

where  $|\uparrow\rangle$  and  $|\downarrow\rangle$  are the two magnetic sub-levels of the excited state. The state then evolves according to the energy of each component:

$$|\Psi(t)\rangle = ae^{-iE_{\uparrow}t} |\uparrow\rangle + be^{-iE_{\downarrow}t} |\downarrow\rangle, \quad (6.2)$$

where we set  $\hbar = 1$ . If we perform a measurement after the state has evolved for time  $t$  in the eigenbasis, then the result does not depend on the time:

$$|\langle \uparrow | \Psi(t) \rangle|^2 = \frac{a^2}{a^2 + b^2} \quad \text{and} \quad |\langle \downarrow | \Psi(t) \rangle|^2 = \frac{b^2}{a^2 + b^2}. \quad (6.3)$$

To extract the phase difference between  $|\uparrow\rangle$  and  $|\downarrow\rangle$ , we have to measure in a different basis  $|V\rangle = |\uparrow\rangle - |\downarrow\rangle$  and  $|H\rangle = |\uparrow\rangle + |\downarrow\rangle$ . We then have

$$|\langle V | \Psi(t) \rangle|^2 \propto a^2 + b^2 - 2ba \cos(\Delta Et), \quad (6.4)$$

where  $\Delta E = E_{\uparrow} - E_{\downarrow}$  is the Zeeman splitting of the excited state. Detecting in  $\{|V\rangle, |H\rangle\}$  basis can be done by placing a detector in a direction perpendicular to both the quantization axis and the direction of the excitation light, as shown in Fig.

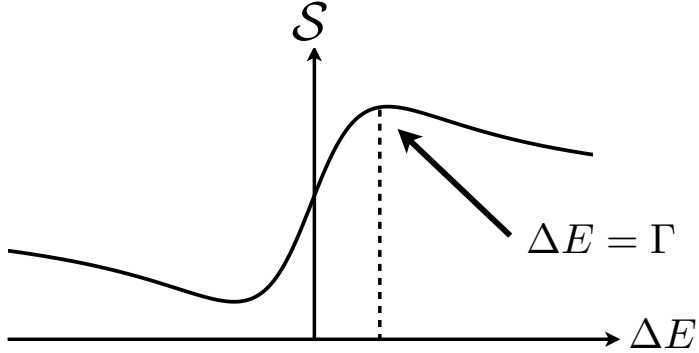


Figure 6-3: Typical Hanle signal.  $S$  is the light intensity at the detector (which detects only a certain circular polarization). The horizontal axis is the energy splitting between the two Zeeman levels of the excited state.  $S$  is maximum when  $\Delta E = \Gamma$ .

**6-2.** The detector must detect only a certain circular polarization.

Next we include the finite lifetime of the excited states, which we model as an exponential decay with a decay rate of  $\Gamma$ . The signal is then

$$S(t) \propto e^{-\Gamma t} (a^2 + b^2 - 2ba \cos(\Delta Et)). \quad (6.5)$$

We find the total signal by integrating the signal with respect to time:

$$S \propto \int_0^\infty S(t) dt \propto \frac{1}{\Gamma} + \frac{\Delta E}{\Delta E^2 + \Gamma^2}. \quad (6.6)$$

A typical Hanle signal is plotted in Fig. 6-3. The term  $\Delta E$  is directly proportional to the magnitude of the magnetic field. Hence, to extract the lifetime of the excited state, we have to measure the detector signal as a function of the magnitude of the magnetic field. The maximum signal occurs when the Zeeman splitting of the excited states matches the decay rate (or the lifetime of the excited state).

It is important to note that before the invention of lasers, all observations of the Hanle effect were carried out with discharge lamps as light sources [66, 67, 68]. In this sense, the light that interacts with atoms (usually confined in a vapor cell) has a broad spectral linewidth and does not induce any coherence between the ground and excited states of the atoms [72]. In the analysis above (and in other textbooks such as [73]), we assume that this is the case. However, if we perform the experiment with

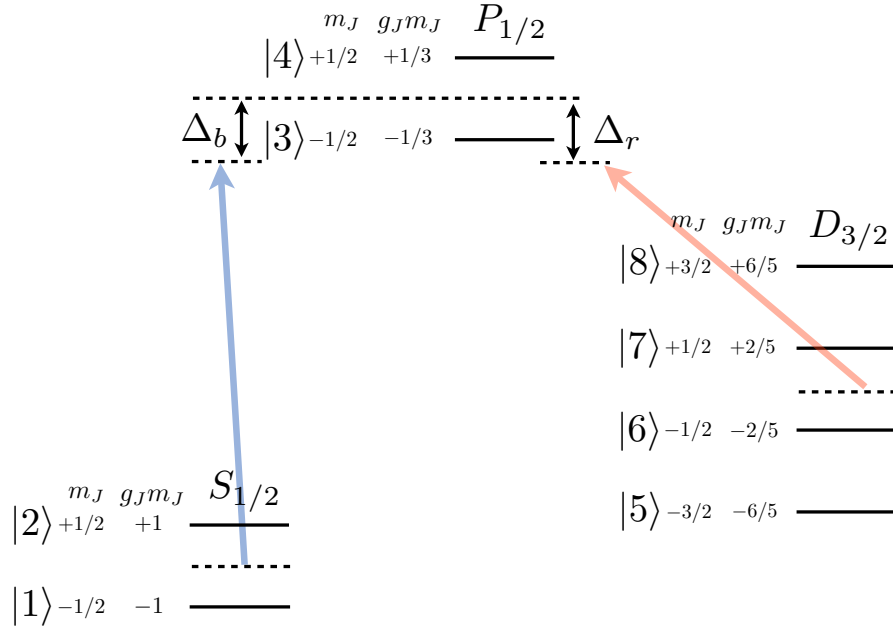


Figure 6-4: Diagram of the parameters of the 8-level Bloch equations.

lasers (which have narrow spectral linewidth), we cannot neglect this coherence and have to use full optical Bloch equations to analyze the problem [74, 65, 75]. In the next section, we will study this effect carefully.

### 6.1.2 Optical Bloch equations with all magnetic sub-levels

To include all the coherences in the system, we have to use the optical Bloch equations (OBE) which include the full light-atom interactions and sources of decoherence from spontaneous emissions and a finite laser linewidth. The basis of the OBE is again the quantum Liouville equation as in Eq. (2.31) with the Liouvillian given by Eq. (2.32). To analyze the Hanle effect in atoms which have an energy level structure similar to  $^{40}\text{Ca}^+$ , we setup the problem as in Fig. 6-4. Since solving the OBE for the full system is lengthy and tedious, we show here only the analysis of the experiment involving the  $|1\rangle$ ,  $|2\rangle$ ,  $|3\rangle$  and  $|4\rangle$  levels in Fig. 6-4. For  $^{40}\text{Ca}^+$ , this corresponds to a situation where only circularly polarized light at 397 nm illuminates the ions with the geometry given in Fig. 6-2.

The Hamiltonian in the interaction picture is given by

$$H = \begin{pmatrix} \Delta_b - \epsilon & 0 & \Omega_L/2 & -\Omega_L/2 \\ 0 & \Delta_b + \epsilon & \Omega_L/2 & -\Omega_L/2 \\ \Omega_L/2 & \Omega_L/2 & -\epsilon/3 & 0 \\ -\Omega_L/2 & -\Omega_L/2 & 0 & \epsilon/3 \end{pmatrix}, \quad (6.7)$$

where  $\Omega_L$  is the Rabi frequency associated with the intensity of the laser light,

$\epsilon = \mu_B B$  and  $\Delta_b$  is the detuning of the “blue” laser light (397 nm for  $^{40}\text{Ca}^+$ ) from the atomic transition. For arbitrary light polarization and direction, the entry that contains atom-light interaction can be calculated using the matrix elements given in Appendix A.2.

Using the AtomicDensityMatrix package in Mathematica<sup>®</sup>, the OBE can be generated conveniently.<sup>1</sup> We have a set of differential equations:

$$\dot{\rho}_{11}(t) = -\frac{i}{\hbar} \left( \frac{\Omega_L}{2} (\rho_{14} - \rho_{41} + \rho_{31} - \rho_{13}) \right) + \frac{p\Gamma}{3} \rho_{33} + \frac{2p\Gamma}{3} \rho_{44} \quad (6.8)$$

$$\dot{\rho}_{12}(t) = -\frac{i}{\hbar} \left( \frac{\Omega_L}{2} (\rho_{14} - \rho_{42} + \rho_{32} - \rho_{13}) - 2\epsilon\rho_{12} \right) - \frac{\Gamma}{3} \rho_{34} \quad (6.9)$$

$$\dot{\rho}_{13}(t) = -\frac{i}{\hbar} \left( \frac{\Omega_L}{2} (\rho_{33} - \rho_{43} - \rho_{11} - \rho_{12}) - (\Delta_b - \frac{2}{3}\epsilon)\rho_{13} \right) - \frac{\Gamma}{2} \rho_{13} - \gamma\rho_{13} \quad (6.10)$$

$$\dot{\rho}_{14}(t) = -\frac{i}{\hbar} \left( \frac{\Omega_L}{2} (\rho_{12} + \rho_{34} + \rho_{11} - \rho_{44}) - (\Delta_b - \frac{4}{3}\epsilon)\rho_{14} \right) - \frac{\Gamma}{2} \rho_{14} - \gamma\rho_{14} \quad (6.11)$$

$$\dot{\rho}_{21}(t) = \frac{i}{\hbar} \left( \frac{\Omega_L}{2} (\rho_{41} - \rho_{24} + \rho_{23} - \rho_{31}) - 2\epsilon\rho_{21} \right) - \frac{\Gamma}{3} \rho_{43} \quad (6.12)$$

$$\dot{\rho}_{22}(t) = -\frac{i}{\hbar} \left( \frac{\Omega_L}{2} (\rho_{24} - \rho_{42} + \rho_{32} - \rho_{23}) \right) + \frac{p\Gamma}{3} \rho_{44} + \frac{2p\Gamma}{3} \rho_{33} \quad (6.13)$$

$$\dot{\rho}_{23}(t) = -\frac{i}{\hbar} \left( \frac{\Omega_L}{2} (\rho_{33} - \rho_{43} - \rho_{21} - \rho_{22}) + (\Delta_b + \frac{4}{3}\epsilon)\rho_{23} \right) - \frac{\Gamma}{2} \rho_{23} - \gamma\rho_{23} \quad (6.14)$$

$$\dot{\rho}_{24}(t) = -\frac{i}{\hbar} \left( \frac{\Omega_L}{2} (\rho_{21} + \rho_{22} + \rho_{34} - \rho_{44}) + (\Delta_b + \frac{2}{3}\epsilon)\rho_{24} \right) - \frac{\Gamma}{2} \rho_{24} - \gamma\rho_{24} \quad (6.15)$$

$$\dot{\rho}_{31}(t) = \frac{i}{\hbar} \left( \frac{\Omega_L}{2} (\rho_{33} - \rho_{34} - \rho_{11} - \rho_{21}) - (\Delta_b - \frac{2}{3}\epsilon)\rho_{31} \right) - \frac{\Gamma}{2} \rho_{31} - \gamma\rho_{31} \quad (6.16)$$

$$\dot{\rho}_{32}(t) = \frac{i}{\hbar} \left( \frac{\Omega_L}{2} (\rho_{33} - \rho_{34} - \rho_{12} - \rho_{22}) + (\Delta_b + \frac{4}{3}\epsilon)\rho_{32} \right) - \frac{\Gamma}{2} \rho_{32} - \gamma\rho_{32} \quad (6.17)$$

$$\dot{\rho}_{33}(t) = -\frac{i}{\hbar} \left( \frac{\Omega_L}{2} (\rho_{13} + \rho_{23} - \rho_{31} - \rho_{32}) \right) - \Gamma \rho_{33} \quad (6.18)$$

$$\dot{\rho}_{34}(t) = -\frac{i}{\hbar} \left( \frac{\Omega_L}{2} (\rho_{14} + \rho_{24} + \rho_{31} + \rho_{32}) - \frac{2}{3}\epsilon\rho_{34} \right) - \Gamma \rho_{34} \quad (6.19)$$

$$\dot{\rho}_{41}(t) = \frac{i}{\hbar} \left( \frac{\Omega_L}{2} (\rho_{21} + \rho_{43} + \rho_{11} - \rho_{44}) - (\Delta_b - \frac{4}{3}\epsilon)\rho_{41} \right) - \frac{\Gamma}{2} \rho_{41} - \gamma\rho_{41} \quad (6.20)$$

$$\dot{\rho}_{42}(t) = \frac{i}{\hbar} \left( \frac{\Omega_L}{2} (\rho_{12} + \rho_{22} + \rho_{43} - \rho_{44}) + (\Delta_b + \frac{2}{3}\epsilon)\rho_{42} \right) - \frac{\Gamma}{2} \rho_{42} - \gamma\rho_{42} \quad (6.21)$$

$$\dot{\rho}_{43}(t) = \frac{i}{\hbar} \left( \frac{\Omega_L}{2} (\rho_{41} + \rho_{42} + \rho_{13} + \rho_{23}) - \frac{2}{3}\epsilon\rho_{43} \right) - \Gamma \rho_{43} \quad (6.22)$$

$$\dot{\rho}_{44}(t) = -\frac{i}{\hbar} \left( \frac{\Omega_L}{2} (\rho_{41} - \rho_{14} + \rho_{42} - \rho_{24}) \right) - \Gamma \rho_{44} \quad (6.23)$$

---

<sup>1</sup>See Appendix B for more details about how to use this wonderful package.

$$\dot{\rho}_{55}(t) = (1-p)\Gamma(\rho_{44} + \rho_{33}), \quad (6.24)$$

where  $p$  is the branching fraction of the excited state,  $\Gamma$  is the decay rate of the excited state and  $\gamma$  is the linewidth of the laser [72]. Here we collectively label every state in the  $D_{3/2}$  level to be  $|5\rangle$ .

We cannot simply observe a steady state fluorescence of the ions because the excited states eventually decays to the dark state  $|5\rangle$ . Instead, we use an experimental scheme similar to that presented in Chapter 5 and measure the total number photons emitted from the ions before all the ions are in the dark state, i.e.  $|5\rangle$ . This means we have to integrate Eq. (6.8) to (6.24) with respect to time. Let the boundary conditions for the atomic populations be all zero except  $\rho_{11}(0) = 1$  and  $\rho_{55}(t \rightarrow \infty) = 1$ . By writing  $P_{ij} = \int_0^\infty \rho_{ij}(t)dt$ , we have

$$-1 = -\frac{i}{\hbar} \left( \frac{\Omega_L}{2} (P_{14} - P_{41} + P_{31} - P_{13}) \right) + \frac{p\Gamma}{3} P_{33} + \frac{2p\Gamma}{3} P_{44} \quad (6.25)$$

$$0 = -\frac{i}{\hbar} \left( \frac{\Omega_L}{2} (P_{14} - P_{42} + P_{32} - P_{13}) - 2\epsilon P_{12} \right) - \frac{\Gamma}{3} P_{34} \quad (6.26)$$

$$0 = -\frac{i}{\hbar} \left( \frac{\Omega_L}{2} (P_{33} - P_{43} - P_{11} - P_{12}) - (\Delta_b - \frac{2}{3}\epsilon) P_{13} \right) - \frac{\Gamma}{2} P_{13} - \gamma P_{13} \quad (6.27)$$

$$0 = -\frac{i}{\hbar} \left( \frac{\Omega_L}{2} (P_{12} + P_{34} + P_{11} - P_{44}) - (\Delta_b - \frac{4}{3}\epsilon) P_{14} \right) - \frac{\Gamma}{2} P_{14} - \gamma P_{14} \quad (6.28)$$

$$0 = \frac{i}{\hbar} \left( \frac{\Omega_L}{2} (P_{41} - P_{24} + P_{23} - P_{31}) - 2\epsilon P_{21} \right) - \frac{\Gamma}{3} P_{43} \quad (6.29)$$

$$0 = -\frac{i}{\hbar} \left( \frac{\Omega_L}{2} (P_{24} - P_{42} + P_{32} - P_{23}) \right) + \frac{p\Gamma}{3} P_{44} + \frac{2p\Gamma}{3} P_{33} \quad (6.30)$$

$$0 = -\frac{i}{\hbar} \left( \frac{\Omega_L}{2} (P_{33} - P_{43} - P_{21} - P_{22}) + (\Delta_b + \frac{4}{3}\epsilon) P_{23} \right) - \frac{\Gamma}{2} P_{23} - \gamma P_{23} \quad (6.31)$$

$$0 = -\frac{i}{\hbar} \left( \frac{\Omega_L}{2} (P_{21} + P_{22} + P_{34} - P_{44}) + (\Delta_b + \frac{2}{3}\epsilon) P_{24} \right) - \frac{\Gamma}{2} P_{24} - \gamma P_{24} \quad (6.32)$$

$$0 = \frac{i}{\hbar} \left( \frac{\Omega_L}{2} (P_{33} - P_{34} - P_{11} - P_{21}) - (\Delta_b - \frac{2}{3}\epsilon) P_{31} \right) - \frac{\Gamma}{2} P_{31} - \gamma P_{31} \quad (6.33)$$

$$0 = \frac{i}{\hbar} \left( \frac{\Omega_L}{2} (P_{33} - P_{34} - P_{12} - P_{22}) + (\Delta_b + \frac{4}{3}\epsilon) P_{32} \right) - \frac{\Gamma}{2} P_{32} - \gamma P_{32} \quad (6.34)$$

$$0 = -\frac{i}{\hbar} \left( \frac{\Omega_L}{2} (P_{13} + P_{23} - P_{31} - P_{32}) \right) - \Gamma P_{33} \quad (6.35)$$

$$0 = -\frac{i}{\hbar} \left( \frac{\Omega_L}{2} (P_{14} + P_{24} + P_{31} + P_{32}) - \frac{2}{3}\epsilon P_{34} \right) - \Gamma P_{34} \quad (6.36)$$

$$0 = \frac{i}{\hbar} \left( \frac{\Omega_L}{2} (P_{21} + P_{43} + P_{11} - P_{44}) - (\Delta_b - \frac{4}{3}\epsilon) P_{41} \right) - \frac{\Gamma}{2} P_{41} - \gamma P_{41} \quad (6.37)$$

$$0 = \frac{i}{\hbar} \left( \frac{\Omega_L}{2} (P_{12} + P_{22} + P_{43} - P_{44}) + (\Delta_b + \frac{2}{3}\epsilon) P_{42} \right) - \frac{\Gamma}{2} P_{42} - \gamma P_{42} \quad (6.38)$$

$$0 = \frac{i}{\hbar} \left( \frac{\Omega_L}{2} (P_{41} + P_{42} + P_{13} + P_{23}) - \frac{2}{3} \epsilon P_{43} \right) - \Gamma P_{43} \quad (6.39)$$

$$0 = -\frac{i}{\hbar} \left( \frac{\Omega_L}{2} (P_{41} - P_{14} + P_{42} - P_{24}) \right) - \Gamma P_{44} \quad (6.40)$$

$$1 = (1-p)\Gamma(P_{44} + P_{33}), \quad (6.41)$$

where we assume that  $\Omega_L$  is constant. These equations become a set of linear equations and the value of  $P_{ij}$  can be solved exactly. Depending on the detector configuration, we can extract the signal using the fluorescence operator [65]. For example, if the detector does not distinguish the polarization of the light, we have

$$\mathcal{F} = |3\rangle\langle 3| + |4\rangle\langle 4|. \quad (6.42)$$

To extract the observable from the any operator, we calculate the trace of the product between the density matrix and the operator. The observed scattering rate is given by

$$S = \Gamma(\text{tr}(\rho\mathcal{F})) = \Gamma(\rho_{33} + \rho_{44}). \quad (6.43)$$

Since we are interested in the total number of photons, the signal is

$$\mathcal{S} = \Gamma \int_0^\infty \text{tr}(\rho\mathcal{F})dt = \Gamma(P_{33} + P_{44}). \quad (6.44)$$

Note that the using last equation in the set, Eq. (6.41), we get

$$\mathcal{S} = \langle n \rangle = \frac{1}{1-p}. \quad (6.45)$$

This confirms the fact in the previous chapter that we do not observe the Hanle effect for the  $J = 1/2$  excited state if the detector does not distinguish the circular polarization of the photons even when we consider all the Zeeman sub-levels.

For the observation of the Hanle effect, we are interested in detecting the light in the circular polarization basis. The corresponding fluorescence operator is given by

$$\mathcal{F}^\pm = \frac{1}{2} (|3\rangle\langle 3| + |4\rangle\langle 4| \pm i(|3\rangle\langle 4| - |4\rangle\langle 3|)), \quad (6.46)$$

where the  $\pm$  sign indicates whether the detector detects left or right circular polarization. The scattering rate is then given by

$$S^\pm = \Gamma \text{tr}(\rho\mathcal{F}) = \frac{1}{2} (\rho_{33} + \rho_{44} \pm i(\rho_{34} - \rho_{43})). \quad (6.47)$$

The total number of photons of each circular polarization detected is

$$\mathcal{S}^\pm = \Gamma \int_0^\infty \text{tr}(\rho\mathcal{F})dt = \frac{\Gamma}{2} (P_{33} + P_{44} \pm i(P_{34} - P_{43})). \quad (6.48)$$

We note that the Hanle signal is contained exclusively in the last term:  $i(P_{34} - P_{43})$ . It turns out that Eq. (6.48) always takes the following form:

$$\mathcal{S}^\pm = \frac{1}{2(1-p)} (1 \pm f(\epsilon)). \quad (6.49)$$

The sum of the number of photons for each circular polarization is the total number of photons scatter given by Eq. (6.45):

$$\mathcal{S}^+ + \mathcal{S}^- = \frac{1}{1-p}. \quad (6.50)$$

The analysis presented above can be applied to the case where we use the laser which couples the  $D_{3/2}$  state to the  $P_{1/2}$  state instead. Experimentally, this means we excite the  $^{40}\text{Ca}^+$  ions with the circularly polarized 866 nm laser light and detect circularly polarized 397 nm photons emitted from the ions.

## 6.2 The Hanle effect in trapped calcium ion

In this section, we summarize the results of the calculation using the analysis presented in the previous section applied to  $^{40}\text{Ca}^+$ . We consider the two main experimental schemes: excitation with 397 nm light ( $^2\text{S}_{1/2}$  to  $^2\text{P}_{1/2}$ ) and excitation with 866 nm light ( $^2\text{D}_{3/2}$  to  $^2\text{P}_{1/2}$ ). In both cases, the average number of photons at 397 nm detected with a particular circular polarization is given by the expression in Eq. (6.48). For convenience, we rewrite the Zeeman splitting  $\epsilon$  in terms of the energy difference between the two magnetic sub-levels of the excited state,  $\omega = 2\epsilon/3$ .  $\omega$  also serves us as a measure of the strength of the applied magnetic field. The Hanle signal is now contained in the term  $f(\omega)$ . All frequencies are written in the unit of the decay rate  $\Gamma$  of the excited state  $^2\text{S}_{1/2}$ .

### 6.2.1 $^2\text{S}_{1/2} \rightarrow ^2\text{P}_{1/2}$ transition

In this case, the Hamiltonian is again given by Eq. (6.7). Although we can obtain the Hanle signal according to Eq. (6.48) exactly, it is very complicated. Therefore, it is more illuminating to look at a few limiting cases.

At zero laser light detuning ( $\Delta_b = 0$ ) and in the broadband excitation limit ( $\gamma \rightarrow \infty$ ), we have

$$f(\omega) = \frac{\omega}{1 + \omega^2}, \quad (6.51)$$

which agrees with calculations in the literature [55]. The extrema of the Hanle signal are at  $\omega = \pm 1$ . For arbitrary angle  $\theta$  between the magnetic field and the direction of the laser light, we have

$$f(\omega) = \frac{\omega}{1 + \omega^2} \sin \theta. \quad (6.52)$$

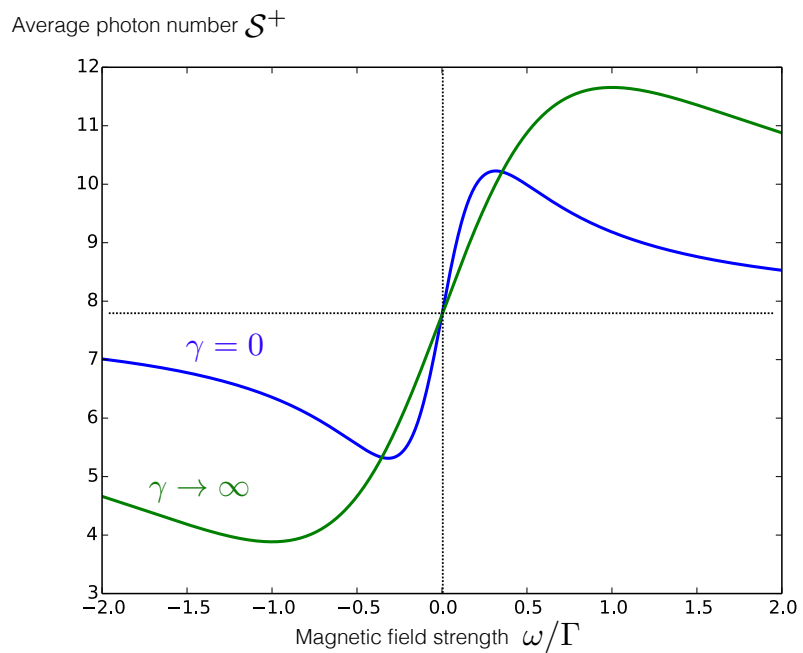


Figure 6-5: The Hanle effect for  ${}^2\text{S}_{1/2} \rightarrow {}^2\text{P}_{1/2}$  excitation. We plot the average number of photons scatter,  $\langle n \rangle$ , as a function of the magnetic field strength applied to the ion. We show the two cases with a narrowband excitation ( $\gamma = 0$ ) and a broadband excitation ( $\gamma \rightarrow \infty$ ).

Usually, experiments on the Hanle effect are carried out with discharge lamps, for which the broadband limit is well justified. It is also possible to artificially broaden the linewidth of a diode laser source using current modulation.

In the narrowband excitation limit ( $\gamma \rightarrow 0$ ), we expand in terms of the laser light intensity,  $\Omega_L$ ,

$$f(\omega) = \frac{2\omega}{1+10\omega^2} + \frac{2\omega(p-3+24\omega^2+8p\omega^2)\Omega_L^2}{3(1+\omega^2)(1+10\omega^2)^2} + O[\Omega_L^4], \quad (6.53)$$

which, for low intensity, gives the extrema of the Hanle signal at  $\omega = \pm\Gamma/\sqrt{10}$ . If we have a small deviation  $\delta\theta$  of the laser direction from the axis perpendicular to the magnetic field, we have

$$f(\omega) = \frac{2\omega}{1+10\omega^2} + \frac{12(p-1)\omega^3\delta\theta}{(1+10\omega^2)(1+10\omega^2+2p\omega^2)} + O[\delta\theta^2]. \quad (6.54)$$

The simulated Hanle signals for both cases (in the limit of low intensity  $\Omega_L \rightarrow 0$ ) are plotted in Fig. 6-5. Both curves are centered at half the mean average number of photons scattered,  $1/2(1-p)$ . For  $^{40}\text{Ca}^+$ , with  $p \sim 0.9357$  we have  $1/2(1-p) \sim 7.77$ . In the narrow band limit, we can see that the modulation of the photon number due to the Hanle effect can be as much as 50% for the broadband excitation.

### 6.2.2 $^2\text{D}_{3/2} \rightarrow ^2\text{P}_{1/2}$ transition

We now analyze the experiment where the excitation laser is the 866 nm laser. Since we detect only the 397 nm photons emitted from the ions, the total number of the 397 nm photons detected is 1. The Hanle signal then takes the form

$$\mathcal{S}^\pm = \frac{1}{2}(1 \pm f(\omega)). \quad (6.55)$$

For the excitation from  $^2\text{D}_{3/2}$  to  $^2\text{P}_{1/2}$ , the light-ion interaction Hamiltonian is given by

$$H = \begin{pmatrix} -\frac{\epsilon}{3} & 0 & \frac{\sqrt{3}\Omega_L}{2} & -\Omega_L & \frac{\Omega_L}{2} & 0 \\ 0 & \frac{\epsilon}{3} & 0 & \frac{\Omega_L}{2} & -\Omega_L & \frac{\sqrt{3}\Omega_L}{2} \\ \frac{\sqrt{3}\Omega_L}{2} & 0 & \Delta_r - \frac{6\epsilon}{5} & 0 & 0 & 0 \\ -\Omega_L & \frac{\Omega_L}{2} & 0 & \Delta_r - \frac{2\epsilon}{5} & 0 & 0 \\ \frac{\Omega_L}{2} & -\Omega_L & 0 & 0 & \Delta_r + \frac{2\epsilon}{5} & 0 \\ 0 & \frac{\sqrt{3}\Omega_L}{2} & 0 & 0 & 0 & \Delta_r + \frac{6\epsilon}{5} \end{pmatrix}. \quad (6.56)$$

Solving the Bloch equations, we obtain the signal in the broadband limit ( $\gamma \rightarrow \infty$ ) and zero detuning ( $\Delta_r = 0$ ) to be

$$f(\omega) = \frac{2}{5} \frac{\omega}{1+\omega^2} + \frac{(25p' - 2(96+5p')\omega^2)\Omega_L^2}{75\gamma\omega(1+\omega^2)^2} + O[\Omega_L^4], \quad (6.57)$$

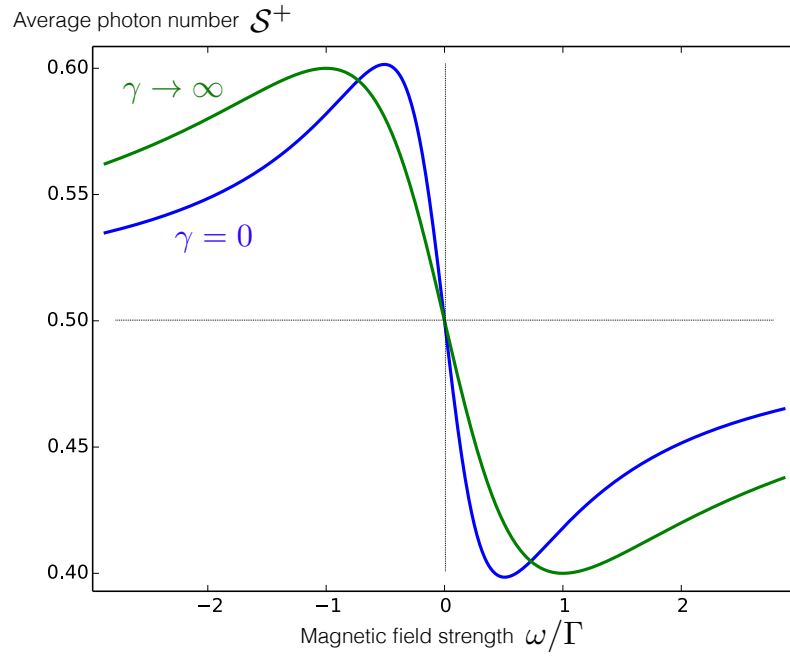


Figure 6-6: The Hanle effect for  $^2\text{D}_{3/2} \rightarrow ^2\text{P}_{1/2}$  excitation. We plot the average number of photons scatter,  $\mathcal{S}^+$ , as a function of the magnetic field strength applied to the ion. We show the two cases with a narrowband excitation ( $\gamma = 0$ ) and a broadband excitation ( $\gamma \rightarrow \infty$ ).

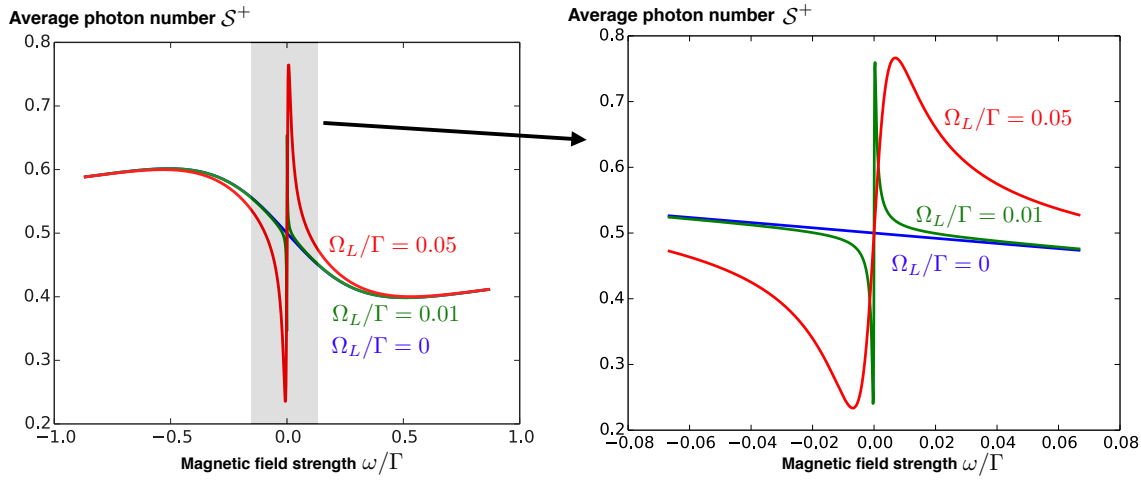


Figure 6-7: Sharp resonances at low magnetic field strength for the narrowband excitation ( $\gamma = 0$ ) shown for different values of  $\Omega_L$ . The plot on the right is a magnification of the shaded region of the plot on the left.

for initially unpolarized ions ( $\rho_{55}(0) = \rho_{66}(0) = \rho_{77}(0) = \rho_{88}(0) = 1/4$ ). Note that  $p' = 1 - p$  is the probability that the excited states decay back to the  ${}^2D_{3/2}$  manifold. If we have  $\rho_{55}(0) = 1$  or  $\rho_{88}(0) = 1$ , then the signal is given by

$$f(\omega) = \frac{2}{5} \frac{p'\omega}{1 + \omega^2} - \frac{(-25p'^2 + 192p'\omega^2 + 10p'^2\omega^2)\Omega_L^2}{75\gamma\omega(1 + \omega^2)^2} + O[\Omega_L^4]. \quad (6.58)$$

If we have  $\rho_{66}(0) = 1$  or  $\rho_{77}(0) = 1$ , then the signal is given by

$$f(\omega) = \frac{2}{5} \frac{(2 - p')\omega}{1 + \omega^2} - \frac{(2 - p')(-25p' + 192\omega^2 + 10p'\omega^2)\Omega_L^2}{75\gamma\omega(1 + \omega^2)^2} + O[\Omega_L^4]. \quad (6.59)$$

For a narrowband excitation ( $\gamma = 0$ ) and unpolarized ions, the Hanle signal is given by

$$\begin{aligned} f(\omega) = & \frac{20\omega}{25 + 97\omega^2} + \frac{2(15623p' - (375000 - 179375p')\omega^2)\Omega_L^2}{3\omega(1 + \omega^2)(25 + 97\omega^2)^2(25 + 529\omega^2)} + \\ & + \frac{2(-(4040400 + 747725p')\omega^4 + (979464 - 125235p')\omega^6)\Omega_L^2}{3\omega(1 + \omega^2)(25 + 97\omega^2)^2(25 + 529\omega^2)} + O[\Omega_L^2]. \end{aligned} \quad (6.60)$$

The expected Hanle signals for both cases (in the limit of low intensity  $\Omega_L \rightarrow 0$  and initially unpolarized ions) are plotted in Fig. 6-6. For finite  $\Omega_L$ , the Hanle curve exhibit an additional sharp resonance at low magnetic field. This resonance is contained in the term proportional to  $1/\omega$  in the expansions of  $f(\omega)$ . So far we do not have any intuitive explanation for the origin of this sharp resonance. We note that this resonance is completely absent in the case of the  ${}^2S_{1/2}$  to  ${}^2P_{1/2}$  excitation.

### 6.3 Experimental considerations

In this section, we analyze a few potential systematic uncertainties in the measurement of the lifetime of  ${}^{40}\text{Ca}^+$ . We consider the case of a narrowband excitation of  ${}^2S_{1/2}$  to  ${}^2P_{1/2}$  transition and see how imperfections in the laser linewidth, laser intensity and geometry of the setup influence the errors in the measurement of the lifetime.

We focus here on the narrow band case as it turned out to be difficult to broaden our laser source enough to be in the broadband limit. Ideally, the Hanle signal for the narrowband excitation of  ${}^2S_{1/2}$  to  ${}^2P_{1/2}$  transition in the limit of low probe intensity ( $\Omega_L = 0$ ) is given by

$$\mathcal{S}^+ = S_0 \left( 1 + \frac{2\omega}{1 + 10\omega^2} \right), \quad (6.61)$$

where the maximum of the signal is at  $\omega = 1/\sqrt{10}$ . If the intensity of the probe light is not low enough and has a small finite value of  $\Omega_L = 0.1$ , the position of the signal maximum shifts according to Eq. (6.53) at the  $6 \times 10^{-3}$  level. Experimentally, we can measure  $\Omega_L$  rather accurately by measuring the decay constant of the fluorescence

during the detection as given by Eq. (4.5). Another source of uncertainty is the direction of the laser beam with respect to the magnetic field direction as given in Eq. (6.54). We found that a  $5^\circ$  deviation from an ideal  $90^\circ$  shifts the maximum of the Hanle signal at the  $4 \times 10^{-4}$  level.<sup>2</sup>

We can confidently set the detuning of the laser to zero using a spectroscopic method presented in Chapter 4 which works for both the 397 nm and 866 nm excitations. The center frequency of the atomic transition can be measured with a precision in the order of 200 kHz. This uncertainty in the laser detuning shifts the maximum of the Hanle signal less than  $3 \times 10^{-4}$ .

The most significant source of the uncertainty seems to be the linewidth of the laser. For  $\gamma = 0.01$ , which corresponds to the laser linewidth of  $2\pi \times 220$  kHz,<sup>3</sup> the maximum of the Hanle effect is shifted by  $3 \times 10^{-2}$ . Since measuring the linewidth of the laser is a non-trivial experimental task, it might be more desirable to artificially broaden the linewidth of the laser and to measure the Hanle signal in the broadband limit. This can be done by a current modulation of laser diodes or tapered-amplifiers [76].

---

<sup>2</sup>A  $10^\circ$  deviation from  $90^\circ$  shifts the maximum of the Hanle signal at the  $5 \times 10^{-3}$  level.

<sup>3</sup>For  ${}^{40}\text{Ca}^+$ , the linewidth of the  ${}^2\text{P}_{1/2}$  state is  $\Gamma = 2\pi \times 22.4$  MHz so  $\gamma = 0.01 \times \Gamma$  is equal to approximately  $2\pi \times 220$  kHz [26].

# Chapter 7

## Spectroscopy with correlated atoms

In this chapter, we demonstrate a generalized Ramsey-type spectroscopic technique using two ions. By preparing a correlated state of the ions to be insensitive to common magnetic field fluctuation, we can extract the energy difference between ions very precisely. This experimental technique allows us to use a pair of correlated ions to probe external fields such as the magnetic field gradient and electric field gradient with high accuracy. This level of precision allows us to utilize  $^{40}\text{Ca}^+$  ions to test for local Lorentz symmetry by monitoring the energy level of the ions during a period of 12 hours. Assuming a hydrogen-like structure of  $^{40}\text{Ca}^+$ , our experimental result provides a bound for the violation of local Lorentz invariance at the level of  $1.7 \pm 2.2 \times 10^{-17}$ .

### 7.1 Introduction

An interaction between an atom and external fields gives rise to energy shifts of atomic states. To use an atom as a probe for external field, we need to precisely measure changes in the atomic energy levels. For example, we can use an atom as a magnetometer and measure the magnitude of the magnetic field by measuring the energy between different Zeeman sub-levels. A typical Ramsey spectroscopy allows us to extract the energy difference  $\Delta E$  between two states  $|S\rangle$  and  $|D\rangle$ <sup>1</sup> of a single atom by monitoring the phase evolution  $\phi(t)$  of the super-position state

$$|\Psi(t)\rangle = |S\rangle + e^{i\phi(t)}|D\rangle, \quad (7.1)$$

where  $\phi(t) = \Delta Et/\hbar$ . We can rewrite this state in the singlet-triplet basis,  $|\pm\rangle = |S\rangle \pm |D\rangle$ , as

$$|\Psi(t)\rangle = (1 + e^{i\phi(t)})|+\rangle + (1 - e^{i\phi(t)})|-\rangle. \quad (7.2)$$

---

<sup>1</sup>To be more specific, the state  $|S\rangle$  is a short hand for one of the Zeeman sub-level of the ground state of  $^{40}\text{Ca}^+$ . the state  $|D\rangle$  is short hand for one of the Zeeman sub-level of  $^2\text{D}_{5/2}$  state of  $^{40}\text{Ca}^+$ .

Applying a  $\pi/2$  pulse to this state maps the state  $|+\rangle \rightarrow |S\rangle$  and  $|-\rangle \rightarrow |D\rangle$ . Then, we measure a probabilities  $P_s$  or  $P_d$  for the atom to be in either  $|S\rangle$  or  $|D\rangle$ , respectively. The oscillation frequency of the probability  $P_s(t)$  is directly related to  $\Delta E$ .

This Ramsey-type scheme can be generalized to the case of an entangled state of two atoms. Consider the state

$$|\Psi(t)\rangle = |SD'\rangle + e^{i\phi(t)} |DS'\rangle, \quad (7.3)$$

where the states  $\{|S\rangle, |D\rangle\}$  belong to the first ion and  $\{|S'\rangle, |D'\rangle\}$  belong to the second ion. In this case, the phase  $\phi(t)$  contains the energy difference between the  $|SD'\rangle$  and  $|DS'\rangle$  states. As shown in Ref. [7, 77], we can similarly rewrite the state in the singlet-triplet basis,  $|\pm'\rangle = |SD'\rangle \pm |DS'\rangle$ , as

$$|\Psi(t)\rangle = (1 + e^{i\phi(t)}) |+\rangle' + (1 - e^{i\phi(t)}) |-\rangle'. \quad (7.4)$$

To extract the phase  $\phi(t)$ , we apply  $\pi/2$  pulses to both atoms. The  $\pi/2$  pulses map the state  $|+\rangle' \rightarrow (|SS'\rangle - |DD'\rangle)$  and  $|-\rangle' \rightarrow (|SD'\rangle - |DS'\rangle)$ . It is interesting that the state  $|+\rangle'$  get mapped to a state where a projective measurement will yield similar outcomes for the two atoms: both in  $|S\rangle$  or both in  $|D\rangle$ . We call this case an outcome with an “even” parity. On the other hand, the state  $|-\rangle'$  get mapped to a state where the outcomes are the opposite: one in  $|S\rangle$  and the other one in  $|D\rangle$ . We call this case an “odd” parity. The oscillation frequency of the phase  $\phi(t)$  is contained in the oscillation frequency of these even and odd parity probability signals. Specifically, we define a parity operator to be

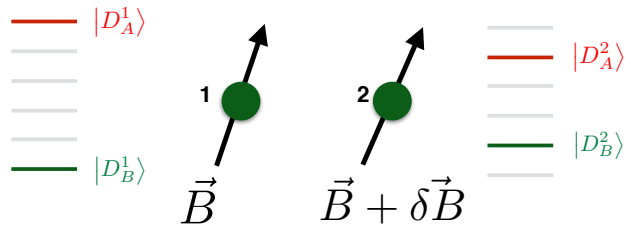
$$P_p = P_{DD'} + P_{SS'} - P_{SD'} - P_{DS'}, \quad (7.5)$$

where  $P_{DD'}$  is a probability of finding the first ion to be in  $|D\rangle$  and the second ion to be in  $|D'\rangle$  and similar for other possible outcomes. Applying a parity operator to the state in Eq. (7.4) after the two  $\pi/2$  pulses gives  $P_p = \cos(\phi(t))$ .

Why do we want to use two ions instead of a single ion? For a single  ${}^{40}\text{Ca}^+$  ion Ramsey experiment, the energy between the  $|S\rangle$  and  $|D\rangle$  states depends linearly on the magnitude of the background magnetic field. Any electronic equipment in the laboratory generates magnetic field radiation randomly and will quickly dephase the super-position state of the ion. The coherence time of the state shown in Eq. (7.1) is typically less than a few milliseconds. On the other hand, the state shown in Eq. (7.3) can be prepared such that both  $|SD'\rangle$  and  $|DS'\rangle$  states have the same linear dependence of the energy on the magnetic field. The phase fluctuation due to magnetic field noise is then a common phase and drops out. In this case, the coherence time is fundamentally limited by the spontaneous emission of the  $|D\rangle$ . This long coherence time allows us to precisely extract the phase  $\phi(t)$  in Eq. (7.3) and measure the energy difference between the  $|SD'\rangle$  and  $|DS'\rangle$  states.

Additionally, we can apply  $\pi$ -pulses to the state in Eq. (7.3) to create a state that involves only different Zeeman components of the D-state, as shown in Fig. 7-1:

$$|\Psi\rangle = |D_A^1 D_A^2\rangle + e^{i\phi(t)} |D_B^1 D_B^2\rangle. \quad (7.6)$$



$$|\Psi\rangle = \frac{1}{\sqrt{2}} \left( |D_A^1 D_A^2\rangle + e^{i\phi(t)} |D_B^1 D_B^2\rangle \right)$$

Figure 7-1: Bell state created from different Zeeman levels of the D-state of two ions.

In this case the phase  $\phi(t)$  is given by

$$\phi(t) = \frac{E_{|D_A^1 D_A^2\rangle} - E_{|D_B^1 D_B^2\rangle}}{\hbar} t. \quad (7.7)$$

This state has an advantage that there is no direct reference from the atomic state to the 729 nm laser since there is no  $|S\rangle$  state involved. Hence the laser phase noise has no influence during the time evolution of the state.

In the following sections, we discuss in details the experimental procedure to create such a state in Eq. (7.6). (Although, we will not create a pure state but rather a mixed state that contains a state in Eq. (7.6)). Then, we utilize this state to measure Zeeman shifts due to a magnetic field gradient and electric quadrupole shifts due to an electric field gradient. In the last section, we apply our experimental method to perform a precise test of local Lorentz symmetry by monitoring the energy shifts of the atomic levels.

## 7.2 Spectroscopy with correlated ions

Preparing a pure entangled state usually requires ions in their motional ground states, which is experimentally challenging with a trap with a high heating rate.<sup>2</sup> However, we can prepare a pure state which dephases to a mixed state that still contains the entangled state.<sup>3</sup> We call this a correlated state since the ions are not in a pure entangled state but rather a mixed state that contains a quantum correlation. In this section we show explicitly how spectroscopy with correlated ions works.

---

<sup>2</sup>It is also possible to create an entangled state from a thermal state using a method shown in Ref. [78]. However, our high heating rate hinders the fidelity of the method.

<sup>3</sup>In our experiment, we rely on a fluctuating magnetic field to dephase our pure state. We can also artificially apply a random common phase noise to the 729 nm laser pulses.

### 7.2.1 State preparation

Our goal is to prepare a mixed state that contains the Bell state

$$|\Psi_B\rangle = \frac{1}{\sqrt{2}} (|D_A^1 D_A^2\rangle + |D_B^1 D_B^2\rangle), \quad (7.8)$$

which is an entangled state illustrated in Fig. 7-1. We start where ion 1 and ion 2 are at their ground states,  $|S^1\rangle$  and  $|S^2\rangle$ , respectively. We then apply four pulses to these ions:

$$|S^1 S^2\rangle \xrightarrow{R_A^1(\frac{\pi}{2},0)} \frac{1}{\sqrt{2}} (|S^1\rangle + i|D_A^1\rangle) \otimes |S^2\rangle \quad (7.9)$$

$$\xrightarrow{R_B^1(\pi,0)} \frac{1}{\sqrt{2}} (|D_B^1\rangle + |D_A^1\rangle) \otimes |S^2\rangle \quad (7.10)$$

$$\xrightarrow{R_A^2(\frac{\pi}{2},0)} \frac{1}{2} (|D_B^1\rangle + |D_A^1\rangle) \otimes (|S^2\rangle + i|D_A^2\rangle) \quad (7.11)$$

$$\xrightarrow{R_B^2(\pi,0)} \frac{1}{2} (|D_B^1\rangle + |D_A^1\rangle) \otimes (|D_B^2\rangle + |D_A^2\rangle) \quad (7.12)$$

The resulting state is a pure product state. Each state then evolves according to its energy. The largest contribution to the phase evolution  $\delta$  of each state due to the linear Zeeman effect:

$$\delta_A^1 = \frac{E|D_A^1\rangle}{\hbar} t = \frac{g_{5/2}\mu_B m_{J=A} |\vec{B}_1|}{\hbar} t \quad (7.13)$$

where the  $m_{J=A}$  is the value of  $m_J$  for state  $|D_A^1\rangle$  and  $\vec{B}_1$  is the magnetic field at the position of ion 1. We insert all the relevant phases into Eq. (7.12):

$$|\Psi(t)\rangle = \frac{1}{2} (e^{-i\delta_B^1} |D_B^1\rangle + e^{-i\delta_A^1} |D_A^1\rangle) \otimes (e^{-i\delta_B^2} |D_B^2\rangle + e^{-i\delta_A^2} |D_A^2\rangle) \quad (7.14)$$

$$= \frac{1}{2} e^{-i(\delta_A^1 + \delta_A^2)} (|D_A^1 D_A^2\rangle + e^{-i(\delta_B^1 + \delta_B^2 - \delta_A^1 - \delta_A^2)} |D_B^1 D_B^2\rangle) + \\ + \frac{1}{2} (e^{-i(\delta_B^1 + \delta_B^2)} |D_B^1 D_A^2\rangle + e^{-i(\delta_A^1 + \delta_B^2)} |D_A^1 D_B^2\rangle). \quad (7.15)$$

Although the magnetic field at the two ion positions is in general different in magnitude, usually they are related by a fixed and stable magnetic field gradient. The fluctuating magnetic field is mostly from the 60 Hz AC power line radiation which affects both ions equally. To the lowest order, we consider only this fast fluctuating field and assume that  $\vec{B} \sim \vec{B}_1 \sim \vec{B}_2$ . In order for the Bell state in Eq. (7.8) to survive this random  $\vec{B}$  fluctuation, we must have  $\delta_B^1 + \delta_B^2 - \delta_A^1 - \delta_A^2 = 0$  or  $\delta_B^1 + \delta_B^2 = \delta_A^1 + \delta_A^2$ . This means that the two components of the Bell state must have the same energy: the sum of the  $m_J$  for each component of the Bell state must be the same. For example, we can have  $|\Psi\rangle = |1/2, -1/2\rangle + |5/2, -5/2\rangle$  or  $|1/2, -3/2\rangle + |-5/2, 3/2\rangle$ . Note that here we use a notation  $|1/2, -1/2\rangle$  to represent a state  $|D; m_J = 1/2, D; m_J - 1/2\rangle$ .

With the condition that either  $\delta_B^1 + \delta_B^2 - \delta_A^1 - \delta_A^2 = 0$  or  $\delta_B^1 + \delta_B^2 = \delta_A^1 + \delta_A^2$ , we then write the state as

$$|\Psi(t)\rangle = \frac{1}{\sqrt{2}}e^{-i(\delta_A^1+\delta_A^2)}|\Psi_B\rangle + \frac{1}{2}\left(e^{-i(\delta_B^1+\delta_A^2)}|D_B^1 D_A^2\rangle + e^{-i(\delta_A^1+\delta_B^2)}|D_A^1 D_B^2\rangle\right). \quad (7.16)$$

After averaging over a randomly fluctuating  $\vec{B}$ , we are left with a mixed state:

$$|\Psi\rangle\langle\Psi| = \frac{1}{4}|D_A^1 D_B^2\rangle\langle D_A^1 D_B^2| + \frac{1}{4}|D_B^1 D_A^2\rangle\langle D_B^1 D_A^2| + \frac{1}{2}|\Psi_B\rangle\langle\Psi_B|. \quad (7.17)$$

We can see that we have a desired Bell state in the resulting mixed state with 50% probability.

### 7.2.2 State readout

After the preparation, we let the state in Eq. (7.17) evolves freely in time. The Bell state component will evolve according to

$$|\Psi_B(t)\rangle \frac{1}{\sqrt{2}}(|D_A^1 D_A^2\rangle + e^{i\phi(t)}|D_B^1 D_B^2\rangle). \quad (7.18)$$

In this section, we discuss the readout process that extracts the phase  $\phi(t)$ .

The analysis pulses are essentially those applied in the preparation process applied in a reversed order. To see how each component contributes to the final parity oscillation signal, we analyze each component of the mixed state separately.

For the first component in Eq. (7.17),

$$|D_A^1 D_B^2\rangle \xrightarrow{R_B^2(\pi,0)} i|D_A^1 S^2\rangle \quad (7.19)$$

$$\xrightarrow{R_A^2(\frac{\pi}{2},0)} \frac{1}{\sqrt{2}}(i|D_A^1 S^2\rangle - |D_A^1 D_A^2\rangle) \quad (7.20)$$

$$\xrightarrow{R_B^1(\pi,0)} \frac{1}{\sqrt{2}}(i|D_A^1 S^2\rangle - |D_A^1 D_A^2\rangle) \quad (7.21)$$

$$\xrightarrow{R_A^1(\frac{\pi}{2},0)} \frac{1}{2}(i|D_A^1 S^2\rangle - |S^1 S^2\rangle - |D_A^1 D_A^2\rangle - i|S^1 D_A^2\rangle) \quad (7.22)$$

For the second component in Eq. (7.17),

$$|D_B^1 D_A^2\rangle \xrightarrow{R_B^2(\pi,0)} |D_B^1 D_A^2\rangle \quad (7.23)$$

$$\xrightarrow{R_A^2(\frac{\pi}{2},0)} \frac{1}{\sqrt{2}}(|D_B^1 D_A^2\rangle + i|D_B^1 S^2\rangle) \quad (7.24)$$

$$\xrightarrow{R_B^1(\pi,0)} \frac{1}{\sqrt{2}}(i|S^1 D_A^2\rangle - |S^1 S^2\rangle) \quad (7.25)$$

$$\xrightarrow{R_A^1(\frac{\pi}{2},0)} \frac{1}{2}(i|S^1 D_A^2\rangle - |D_A^1 D_A^2\rangle - |S^1 S^2\rangle - i|D_A^1 S^2\rangle) \quad (7.26)$$

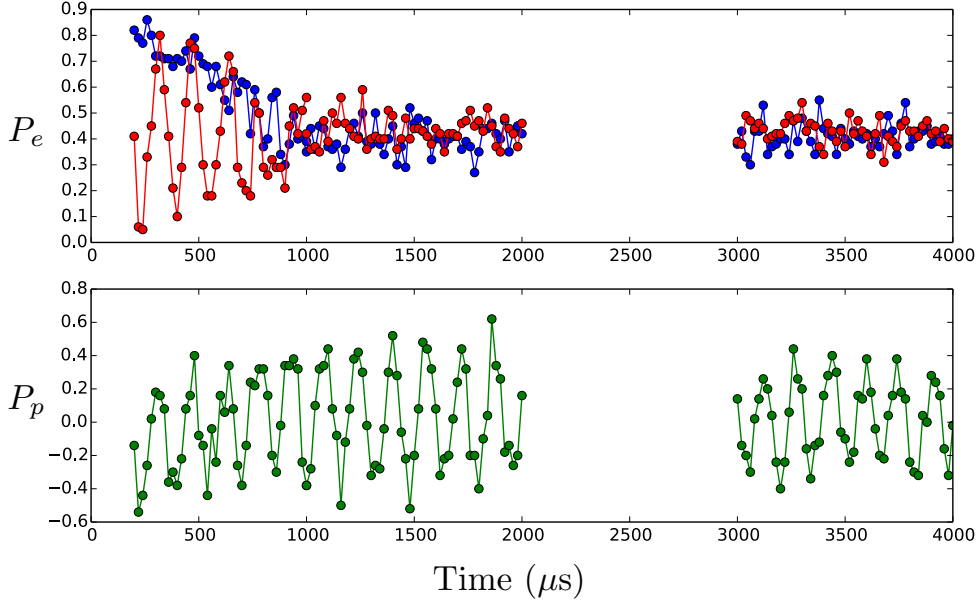


Figure 7-2: Top: Ramsey oscillations for individual ions. Bottom: Parity oscillations of the two ions. We can see that the parity oscillations persists even when the Ramsey oscillations of the individual ions are long washed-out. In this case, the Bell state is  $|\Psi_B\rangle = \frac{1}{\sqrt{2}}(|SD\rangle + |DS\rangle)$ .

As expected, we can see that the first two components do not contribute to the parity signal other than populating the diagonal elements of the density matrix equally.

For the third (Bell state) component in Eq. (7.17),

$$\frac{1}{\sqrt{2}}(|D_A^1 D_A^2\rangle + e^{i\phi} |D_B^1 D_B^2\rangle) \quad (7.27)$$

$$\xrightarrow{R_B^2(\pi,0)} \frac{1}{\sqrt{2}}(|D_A^1 D_A^2\rangle + ie^{i\phi} |D_B^1 S^2\rangle) \quad (7.28)$$

$$\xrightarrow{R_A^2(\frac{\pi}{2},0)} \frac{1}{2}(|D_A^1 D_A^2\rangle + i|D_A^1 S^2\rangle + ie^{i\phi} |D_B^1 S^2\rangle - e^{i\phi} |D_B^1 D_A^2\rangle) \quad (7.29)$$

$$\xrightarrow{R_B^1(\pi,0)} \frac{1}{2}(|D_A^1 D_A^2\rangle + i|D_A^1 S^2\rangle - e^{i\phi} |S^1 S^2\rangle - ie^{i\phi} |S^1 D_A^2\rangle) \quad (7.30)$$

$$\begin{aligned} \xrightarrow{R_A^1(\frac{\pi}{2},0)} & \frac{1}{2\sqrt{2}} \left( (1 + e^{i\phi}) |D_A^1 D_A^2\rangle + i(1 - e^{i\phi}) |S^1 D_A^2\rangle \right) + \\ & + \frac{1}{2\sqrt{2}} \left( i(1 - e^{i\phi}) |D_A^1 S^2\rangle - (1 + e^{i\phi}) |S^1 S^2\rangle \right) \end{aligned} \quad (7.31)$$

In our experimental setup, each ion is addressed by a different 729 nm light beam. We have to take into account that the phase of each laser light (given by  $\phi_{L1}$  and

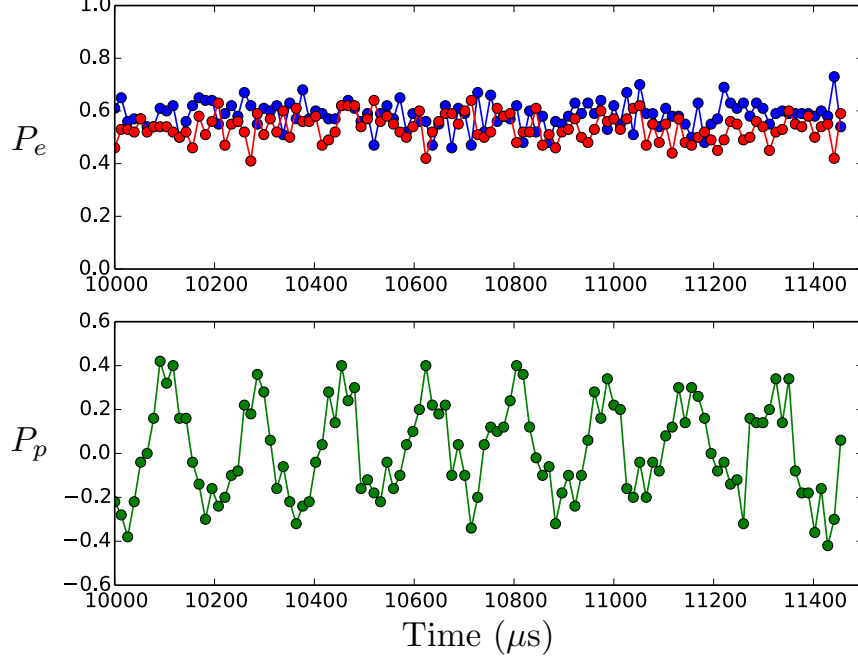


Figure 7-3: Top: Ramsey oscillations for individual ions. Bottom: Parity oscillations of the two ions with the state  $|\Psi_B\rangle = \frac{1}{2}(|D; m_J = -\frac{1}{2}\rangle + |D; m_J = \frac{1}{2}\rangle) \otimes (|D; m_J = \frac{1}{2}\rangle + |D; m_J = -\frac{1}{2}\rangle)$ .

$\phi_{L2}$ ) might be different after a free time evolution of the Bell state.<sup>4</sup> We have

$$\frac{1}{\sqrt{2}}(|D_A^1 D_A^2\rangle + e^{i\phi} |D_B^1 D_B^2\rangle) \quad (7.32)$$

$$\xrightarrow{R_A^2(\pi, \phi_{L2})} \frac{1}{\sqrt{2}}(|D_A^1 D_A^2\rangle + ie^{i(\phi-\phi_{L2})} |D_B^1 S^2\rangle) \quad (7.33)$$

$$\begin{aligned} \xrightarrow{R_A^2(\frac{\pi}{2}, \phi_{L2})} & \frac{1}{2}(|D_A^1 D_A^2\rangle + ie^{-i\phi_{L2}} |D_A^1 S^2\rangle) + \\ & + \frac{1}{2}(ie^{i(\phi-\phi_{L2})} |D_B^1 S^2\rangle - e^{i\phi} |D_B^1 D_A^2\rangle) \end{aligned} \quad (7.34)$$

$$\begin{aligned} \xrightarrow{R_B^1(\pi, \phi_{L1})} & \frac{1}{2}(|D_A^1 D_A^2\rangle + ie^{-i\phi_{L2}} |D_A^1 S^2\rangle) + \\ & - \frac{1}{2}(e^{i(\phi-\phi_{L2}-\phi_{L1})} |S^1 S^2\rangle - ie^{i(\phi-\phi_{L1})} |S^1 D_A^2\rangle) \end{aligned} \quad (7.35)$$

$$\begin{aligned} \xrightarrow{R_A^1(\frac{\pi}{2}, \phi_{L1})} & \frac{1}{2\sqrt{2}}((1 + e^{i\phi}) |D_A^1 D_A^2\rangle + ie^{-i\phi_{L1}}(1 - e^{i\phi}) |S^1 D_A^2\rangle) + \\ & + \frac{1}{2\sqrt{2}}(ie^{-i\phi_{L2}}(1 - e^{i\phi}) |D_A^1 S^2\rangle - e^{-i\phi_{L1}-i\phi_{L2}}(1 + e^{i\phi}) |S^1 S^2\rangle) \end{aligned} \quad (7.36)$$

---

<sup>4</sup>This might be from fluctuating beam paths or a difference in the phases of the two optical fibers for the two 729 nm laser beams.

In any case, after the state readout pulses, the diagonal elements of the density matrix are

$$|\Psi\rangle\langle\Psi| = \left(\frac{1}{4} - \frac{1}{8}\cos\phi\right)|D_A^1 S^2\rangle\langle D_A^1 S^2| + \left(\frac{1}{4} - \frac{1}{8}\cos\phi\right)|S^1 D_A^2\rangle\langle S^1 D_A^2| + \\ + \left(\frac{1}{4} + \frac{1}{8}\cos\phi\right)|S^1 S^2\rangle\langle S^1 S^2| + \left(\frac{1}{4} + \frac{1}{8}\cos\phi\right)|D_A^1 D_A^2\rangle\langle D_A^1 D_A^2| + \dots \quad (7.37)$$

This provides us with the parity signal given by

$$P_p = P_{SS} + P_{DD} - P_{DS} - P_{SD} = \frac{1}{2}\cos\phi, \quad (7.38)$$

where the contrast is half of that given for the entangled state.

### 7.2.3 Detection of the parity oscillation signal

To extract the phase of the parity oscillation, we perform a readout pulse that consists of both the 397 nm and 866 nm lasers. These lasers project the ions to the  $\{|S\rangle, |D\rangle\}$  basis. If the ion is in the  $|S\rangle$  ( $|D\rangle$ ) state, it will appear bright (dark).<sup>5</sup> For the parity operator defined in Eq. (7.38), we need to distinguish the even parity case (both ions are the same) from the even parity case (the ions have opposite outcome). The number of 397 nm photons collected in a 3 ms interval lets us clearly distinguish these cases. We show in Fig. 7-4 the histogram of the photons from our experiment separated by the two threshold (red lines).

We here derive the statistical uncertainty of the parity oscillation signal. Let the outcomes of the  $i$ -th readout of each individual ion be  $x_i$  and  $y_i$ . Both  $x_i$  and  $y_i$ , which are described by the Bernoulli distribution, can take a value of either 1 or 0 with probabilities of  $p_x$  and  $p_y$ , respectively. We can then write the parity signal for the  $i$ -th readout to be

$$\eta_i = x_i y_i + (1 - x_i)(1 - y_i) - x_i(1 - y_i) - y_i(1 - x_i) \quad (7.39)$$

$$= 1 + 4x_i y_i - 2x_i - 2y_i. \quad (7.40)$$

Since  $x_i$  and  $y_i$  can take a value of either 1 or 0,  $\eta_i$  can take a value of  $\pm 1$ . Let's define  $\eta'_i = (\eta_i + 1)/2$  so that  $\eta'_i$  can take a value of either 1 or 0. We can write

$$\eta'_i = \frac{\eta_i + 1}{2} = 1 + 2x_i y_i - x_i - y_i. \quad (7.41)$$

By using  $x_i^2 = x_i$  and  $y_i^2 = y_i$ , we can write

$$\eta'^2_i = 1 + 2x_i y_i - x_i - y_i. \quad (7.42)$$

We can see that  $\eta'^2_i = \eta'_i$ . This fact alone allows us to conclude that  $\eta'_i$  is also described by the Bernoulli distribution. After a large number of trials  $N$ , we can write the best

---

<sup>5</sup>More details can be found in Michael Ramm's thesis.

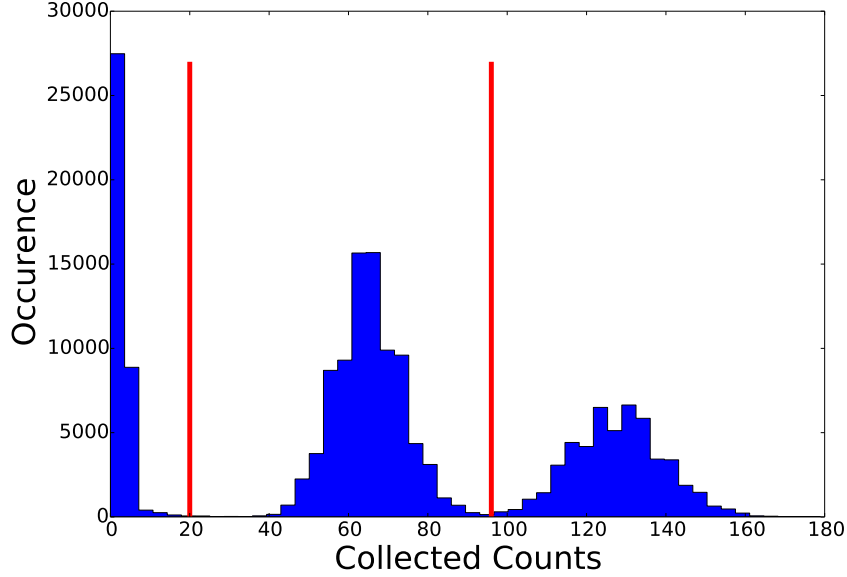


Figure 7-4: Histogram of the readout for two ions. The three peaks clearly distinguish the cases where both ions are bright ( $|SS\rangle$ ), both ions are dark ( $|DD\rangle$ ) and only one ion is bright ( $|SD\rangle$  and  $|DS\rangle$ ).

estimate for the expectation value of  $\eta'_i$  to be

$$\langle \eta' \rangle = \frac{1}{N} \sum_{i=1}^N \eta'_i \pm \sqrt{\frac{\langle \eta' \rangle (1 - \langle \eta' \rangle)}{N}}. \quad (7.43)$$

Then the best estimate for  $\eta_i$  is given by

$$\langle \eta \rangle = \frac{1}{N} \sum_{i=1}^N \eta_i \pm \sqrt{\frac{1 - \langle \eta \rangle^2}{4N}}. \quad (7.44)$$

For a parity signal close to 0, the error is given by  $1/2\sqrt{N}$ .

With this detection method, we show the parity oscillation signals for mixed states that contain  $|\Psi\rangle = |SD\rangle + |DS\rangle$  (as shown in Fig. 7-2) or  $|\Psi\rangle = |D^1 = 1/2, D^2 = -1/2\rangle + |D^1 = -1/2, D^2 = 1/2\rangle$  (as shown in Fig. 7-3). In both cases, we can see that while the Ramsey signal of each individual ion is completely washed-out by the fluctuating magnetic field, the parity oscillations survive for a much longer time.

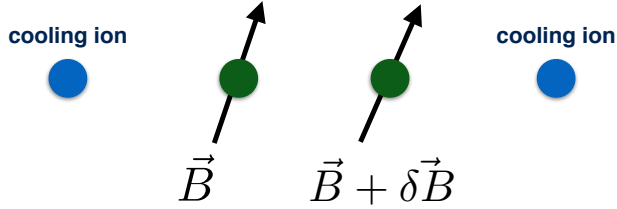


Figure 7-5: Four-ion configuration. The outer two ions are for sympathetic cooling of the inner two ions which we use for spectroscopy. The diagram shows a possibility of having a magnetic field gradient between the two spectroscopic ions.

#### 7.2.4 Correlated ions with additional sympathetically cooling ions

Our trap has intrinsic noise that heats up the ions in the trap. The heating rate is measured to be on the order of  $\sim 0.4 - 1.0$  phonons/ms. Hence, after a evolution period (Ramsey time) in the Ramsey spectroscopy of 200 ms, the ion heats up to a temperature significantly higher than the Doppler temperature. This increase in the ions temperature directly affects the quality of Rabi oscillations and effectively reduces the contrast of the Ramsey fringe. To circumvent this problem, we can use additional ions to perform sympathetic cooling of the two spectroscopy ions. One possible configuration is shown in Fig. 7-5. Note that the Doppler cooling light at 397 nm and 866 nm does not directly destroy the coherence of the two inner spectroscopic ions since they are in the D-state manifold.

Figure 7-6 shows an effect of having additional sympathetic cooling. The lower plot is without any cooling, and the decay constant of the fringe is  $\tau \sim 0.17(3)$  seconds. With sympathetic cooling, the upper plot shows a significant improvement for the decay constant. The decay constant increases to  $\tau \sim 0.65(40)$  seconds. Eventually, the decoherence from the finite D-state lifetime (about 1.2 seconds) kicks in.

### 7.3 Measurement of magnetic field gradient

A magnetic field gradient along the ion can be measured by preparing a product state that contains a Bell state  $|\Psi_B\rangle = |1/2, -1/2\rangle + |-1/2, 1/2\rangle$ . Each component has the same quadrupole shift which depends on  $m_J^2$  as given in Eq. (2.17). Thus the frequency of the parity oscillations only depends on the magnetic field gradient. For a configuration shown in Fig. 7-1, the parity oscillations frequency is given by the energy  $\Delta E = g_{5/2}\mu_B|\delta\vec{B}|$ . The quadratic Zeeman shift, as given in Eq. (2.20), is

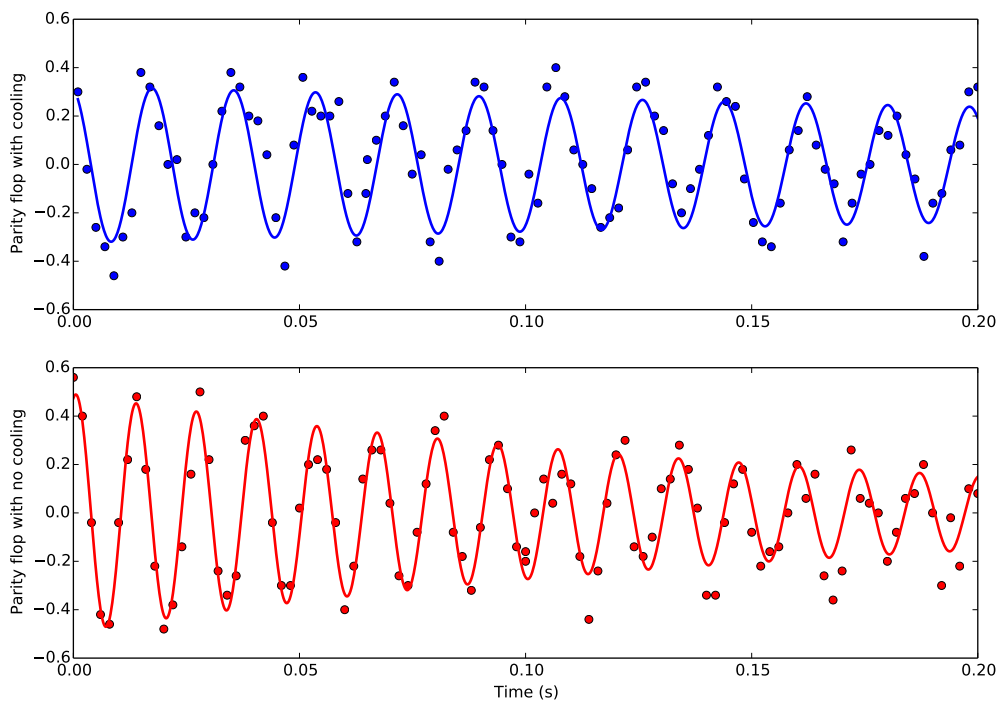


Figure 7-6: Effect of sympathetic cooling on the parity signal. Top: With cooling. The decay constant of the parity fringe is  $\tau = 0.65(40)$  seconds. Bottom: Without cooling.  $\tau = 0.17(3)$  seconds.

State	Energy shift
$\left  \frac{5}{2}, -\frac{5}{2} \right\rangle + \left  \frac{1}{2}, -\frac{1}{2} \right\rangle$	$-2g_{5/2}\mu_B \delta\vec{B} $
$\left  \frac{5}{2}, -\frac{5}{2} \right\rangle + \left  -\frac{1}{2}, \frac{1}{2} \right\rangle$	$-3g_{5/2}\mu_B \delta\vec{B} $
$\left  -\frac{5}{2}, \frac{5}{2} \right\rangle + \left  \frac{1}{2}, -\frac{1}{2} \right\rangle$	$3g_{5/2}\mu_B \delta\vec{B} $
$\left  -\frac{5}{2}, \frac{5}{2} \right\rangle + \left  -\frac{1}{2}, \frac{1}{2} \right\rangle$	$2g_{5/2}\mu_B \delta\vec{B} $

Table 7.1: Energy shifts due to magnetic field gradient for each possible combination of the state  $|\Psi_B\rangle = |1/2, -1/2\rangle + |5/2, -5/2\rangle$ .

negligible for this state. For our experimental configuration ( $f_{\text{axial}} \sim 200$  kHz), we measure  $\Delta E/h \sim 50 - 60$  Hz. In principle, the magnetic field gradient can be reduced further using a set of Helmholtz coils.

If instead we use a Bell state  $|\Psi_B\rangle = |1/2, -1/2\rangle + |5/2, -5/2\rangle$ , there will be significant contributions from both the quadratic Zeeman effect and the electric quadrupole shift. The energy shift from these two effects is independent of the possible combinations of this Bell state,  $|\Psi_B\rangle = |\pm 1/2, \mp 1/2\rangle + |\pm 5/2, \mp 5/2\rangle$ . However, the energy shifts from the magnetic field gradient are different for each combination, as shown in Table 7.1. By taking an average over the measured parity oscillation frequencies for every state in Table 7.1, we found that the frequency contribution from both the quadratic Zeeman and electric quadrupole effect is  $\sim 10$  Hz. The measured magnetic field gradient agrees with the measurement using the  $|1/2, -1/2\rangle + |-1/2, 1/2\rangle$  state.

## 7.4 Test of local Lorentz invariance using correlated ions

Local Lorentz symmetry is fundamental to the Standard Model [80]. If Lorentz symmetry is preserved locally, then the outcome of the experiment does not depend on its orientation with respect to a reference frame (usually defined by the Sun). In the atomic physics setting, if there is a violation of local Lorentz invariance (LLI), then the kinetic energy of electrons in an atom is different depending on the direction in which the electrons move. This results in an energy shift of the atomic transition depending on the orientation of the atom. There have been many theoretical and experimental works that probe the violation of LLI by measuring atomic transition frequencies [81, 82, 83, 84]. In this section, we show how we can use a pair of correlated  $^{40}\text{Ca}^+$  ions to probe the effect of a possible violation of LLI to and potentially improve bounds set by other experiments.

### 7.4.1 Energy shift due to the violation of LLI in $^{40}\text{Ca}^+$

The violation of LLI in atoms would appear as a shift in the energy levels. The magnitude of the shift depends on the wave-function of the electrons. For the  $D_{5/2}$

state of  ${}^{40}\text{Ca}^+$ , the energy shift is given by

$$\frac{\Delta E}{h} = (1.4 \times 10^{15}) \cdot C_0^{(0)} + [(2.4 \times 10^{14}) + (8.2 \times 10^{13}) \cdot m_J^2] \cdot C_0^{(2)} \quad (\text{Hz}), \quad (7.45)$$

where the parameters  $C_0^{(0)}$  and  $C_0^{(2)}$  characterize the degree of the violation of LLI in the context of the Standard Model Extension [81].<sup>6</sup> The violation of LLI is contained in the  $m_J$  because the wave-function of the valence electron in  ${}^{40}\text{Ca}^+$  with different  $m_J$  has different projection onto the quantization axis set by the applied magnetic field. As the Earth rotates, the direction of the applied magnetic field in the laboratory changes its direction with respect to the reference frame set by the Sun. Hence, the direction of the electron's momentum also change its direction with respect to the Sun. If there is a violation of LLI, the energy of the atomic transition will change corresponding to the Earth rotation.

Experimentally, we create a magnetic field insensitive state  $|\Psi_B\rangle = |\frac{5}{2}, -\frac{5}{2}\rangle + |\frac{1}{2}, -\frac{1}{2}\rangle$ , which has an energy difference between the two components given by

$$\frac{\Delta E}{h} = (9.84 \times 10^{14} \text{ Hz}) \cdot C_0^{(2)}. \quad (7.46)$$

We monitor this energy difference and look for a variation that coincides with the Earth's rotation frequency. To the first order, we expect a variation in the energy level with a period of 12 hours.<sup>7</sup> The bound of the energy variation translates directly to the bound of the parameter  $C_0^{(2)}$ , which is currently set by an experiment with dysprosium atoms in Dima Budker's group to be  $C_0^{(2)} < 2.2 \times 10^{-16}$  with 400 seconds of integration time [83].

#### 7.4.2 Experimental procedure

To probe the violation of LLI in  ${}^{40}\text{Ca}^+$ , we simply monitor the energy difference between the two components of the state  $|\Psi_B\rangle = |\frac{5}{2}, -\frac{5}{2}\rangle + |\frac{1}{2}, -\frac{1}{2}\rangle$  using the parity oscillation shown in the previous section. Unfortunately, this energy difference also depends on the magnetic field amplitude (through the quadratic Zeeman effect), the magnetic field gradient and the electric field gradient (through the electric quadrupole shift) created by the trap. In this section, we discuss an experimental procedure that let us separate these contributions from the violation of LLI signal.

To probe the effect of the magnetic field gradient, we measure the oscillation frequencies of the state  $|\Psi_B^+\rangle = |\frac{5}{2}, -\frac{5}{2}\rangle + |\frac{1}{2}, -\frac{1}{2}\rangle$  and  $|\Psi_B^-\rangle = |-\frac{5}{2}, \frac{5}{2}\rangle + |-\frac{1}{2}, \frac{1}{2}\rangle$  to be  $f^+$  and  $f^-$ , respectively. As shown in the previous section, the contribution from the magnetic field gradient for these two states has an opposite sign. Hence, the

---

<sup>6</sup>The derivation is done by Michael Hohensee by evaluating the term  $\langle a | \frac{1}{6m}(p^2 - 3p_z^2) | a \rangle$  and assuming that  ${}^{40}\text{Ca}^+$  has a hydrogen-like atomic structure.

<sup>7</sup>This is because we are looking for a signal with has an even parity. Suppose that the direction from the Earth to the Sun is defined to be  $\hat{z}$ . Then the energy shift in the ions for magnetic field pointing in the  $\hat{x}$  direction is similar to the case with the magnetic field pointing in the  $-\hat{x}$  direction. Hence, the signal for the violation of LLI has a period of 12 hours.

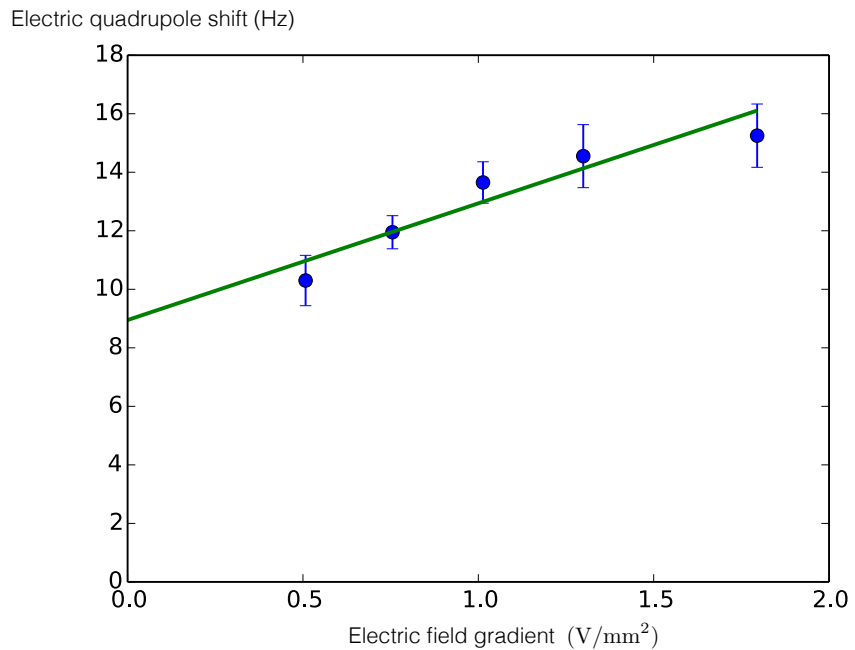


Figure 7-7: Electric quadrupole shift as a function of applied electric field gradient. The offset in the frequency shift at 8.9(8) Hz is due to the quadratic Zeeman effect, which is estimated to be 8 Hz for an applied field of 3.9 G.

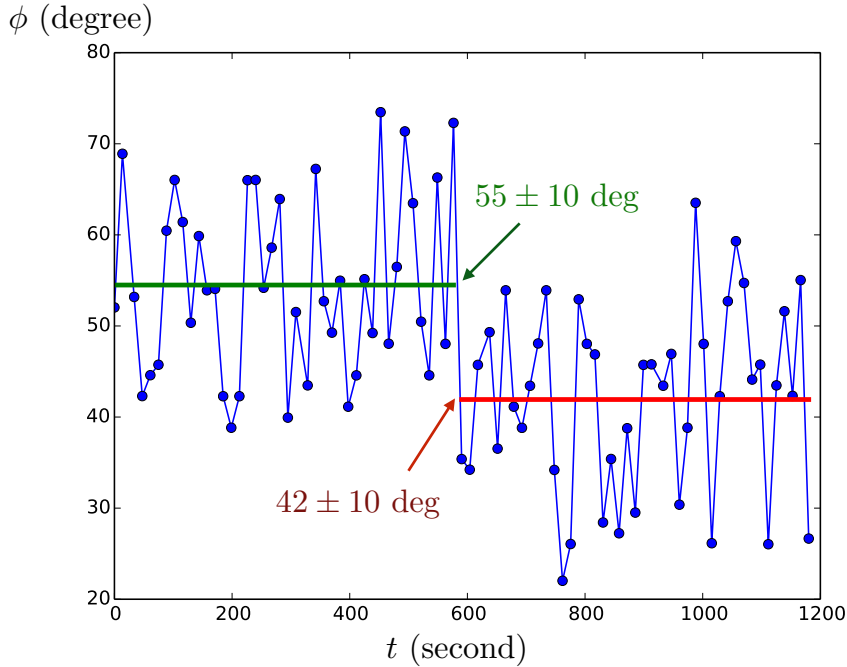


Figure 7-8: Phase jump due to an instantaneous change in the magnetic field gradient. To demonstrate the effect of a drift in the magnetic field gradient on the measurement, we change the current of the magnetic coil at  $t = 600$  seconds by 1 mA. This causes the phase that makes the parity oscillation signal zero jumps by approximately  $13^\circ$ .

oscillation frequency that depends only on the magnetic field magnitude, electric field gradient and the violation of the LLI signal is contained in the averaged frequency  $f^o = (f^+ + f^-)/2$ .

To characterize the effect of the electric quadrupole shift, be measure the frequency  $f^o$  as a function of the electric field gradient in the trap by changing the axial trap frequency. We use Eq. (2.17) to convert from the measured axial trap frequency to the electric field gradient. The result is shown in Fig. 7-7. The fit yields a slope of  $4.0(8)$  Hz $\cdot$ mm $^2$ /V. This translates to a shift in the oscillation frequency of  $27(6)$  mHz per 1 kHz change in the axial trap frequency from the centered value of 210 kHz. The offset of the oscillation frequency at  $8.9(8)$  Hz is due to the quadratic Zeeman shifts. At the applied magnetic field of 3.9 G, the expected quadratic Zeeman shift is calculated to be 8 Hz (see Eq. (2.18)). This translates to a shift in the oscillation frequency of 16 mHz per 1 mG variation in the magnetic field. We actively monitor both the axial trap frequency and the magnitude of the magnetic field by performing spectroscopy on the ion using the 729 nm transition.<sup>8</sup>

To extract the oscillation frequency from the parity signal, one can take the whole parity oscillation curve and extract the frequency by fitting to a model (similar to the

---

<sup>8</sup>Details on how to measure trap frequencies and magnetic field can be found in Michael Ramm's thesis.

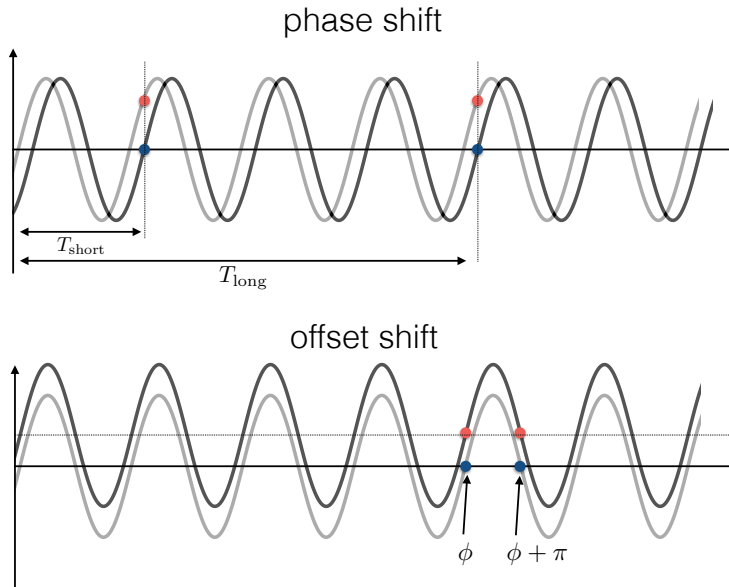


Figure 7-9: Effects of the phase shift and offset shift. Top: a shift in the overall phase of the parity oscillation appears as a frequency shift. To distinguish the phase shift from the frequency shift, we probe the parity oscillation also at a short Ramsey time, which is largely sensitive to the phase shift but not the frequency shift. Bottom: a shift in the overall offset appears also as a frequency shift. To distinguish the offset shift from the frequency shift, we measure the parity oscillation signal where the laser light phase is added by  $\pi$ .

plots in Fig. (7-6)). However, we are more interested in the change in the oscillation frequency rather than the absolute value of the frequency. To monitor the change in the frequency, can constantly probe the parity signal at a fixed Ramsey time. To maximize the sensitivity of the signal to the change in frequency, we calculate the phase of the oscillation from the parity signal. This phase is then used to provide a feedback to the phase of the 729 nm laser such that the parity signal is always close to zero, where the sensitivity is the highest. We monitor the change in the oscillation frequency by monitoring the value of the this phase correction. Fig. 7-8 shows a sudden jump in the phase data when we intentionally change the magnetic field gradient by changing the current on one of the magnetic coils. We convert the variation in the phase to the variation in the frequency using

$$f \text{ (Hz)} = \frac{\phi \text{ (degree)}}{360^\circ \cdot T_{\text{Ramsey}} \text{ (s)}}, \quad (7.47)$$

where  $T_{\text{Ramsey}}$  is the Ramsey time.

There are two effects that can influence the monitoring of the oscillation frequency

of the parity signal using a phase feedback method: phase shift and offset shift. These two effects are shown in Fig. 7-9. We observe a slight dependence of the phase of the parity oscillation on the detuning of the 729 nm laser light from the carrier transitions of  $^{40}\text{Ca}^+$ .<sup>9</sup> To subtract out the effect from the phase shift, we additionally monitor the parity signal at a short Ramsey time  $T_{\text{short}}$ , where the phase feedback is more sensitive to the phase shift. The difference of the parity oscillation signals between  $T_{\text{short}}$  and  $T_{\text{long}}$  depends only on the frequency shift of the parity oscillation but not the phase shift. However, we sacrifice the sensitivity by having instead an effective Ramsey time equals to  $T_{\text{long}} - T_{\text{short}}$ .

To subtract out the effect of the offset drift, we compare the parity signal to the signal where we add  $180^\circ$  (or  $\pi$ ) to the phase of one of the readout 729 nm laser (see Fig. 7-9). The phase correction is derived from the difference between these two signals.

In summary, each measurement iteration consists of probing the parity signal with the state  $|\Psi_B^+\rangle$  and  $|\Psi_B^-\rangle$ , with  $T_{\text{short}}$  and  $T_{\text{long}}$ , and with two opposite phases of the 729 nm laser pulse. For our measurement of the violation of LLI, we chose  $T_{\text{short}} = 2$  ms and  $T_{\text{long}} = 100$  ms.  $T_{\text{short}}$  is chosen to be long enough such that the state of our ions has already dephased to the mixed state. As shown in Fig. 7-2, at 2 ms, the random fluctuation in the magnetic field has completely dephased any component that is sensitive to the magnetic field. We can potentially increase  $T_{\text{long}}$  to increase the sensitivity of our measurement. Currently, the heating rate of the trap limits our Ramsey fringe decay constant to about 170 ms. This effect can be circumvented by performing sympathetic cooling on the additional ions. However, we observed that the 866 nm laser light can induce an AC-Stark shift of the state  $|\Psi_B^\pm\rangle$  up to 20 Hz.

#### 7.4.3 Experimental result

With the experimental parameters given in the previous section, we monitor the frequency variation of the state  $|\Psi_B^+\rangle = \left| \frac{5}{2}, -\frac{5}{2} \right\rangle + \left| \frac{1}{2}, -\frac{1}{2} \right\rangle$  in a course of 12 hours starting from 7:30 pm of April 14th, 2014. The frequency data corrected with independently measured magnetic field (Fig. 7-10) and axial frequency (Fig. 7-11) is shown in Fig. 7-12. The fit yields the amplitude of the variation to be  $17 \pm 22$  mHz. The Allan deviation of the frequency data is shown in Fig. 7-13. Deviations from the fitted line are likely caused by systematics that we have not accounted for.

To convert from the variation of the measured frequency to the violation of LLI parameter, we use Eq. (7.46) which assumes a simple hydrogen-like model of  $^{40}\text{Ca}^+$ . Our preliminary result yields the bound for the parameter  $C_0^{(2)}$  to be  $1.7 \pm 2.2 \times 10^{-17}$ . This is an improvement of almost an order of magnitude compared to the previous work done in Ref. [83].

---

<sup>9</sup>The origin of this dependence is yet to be understood.

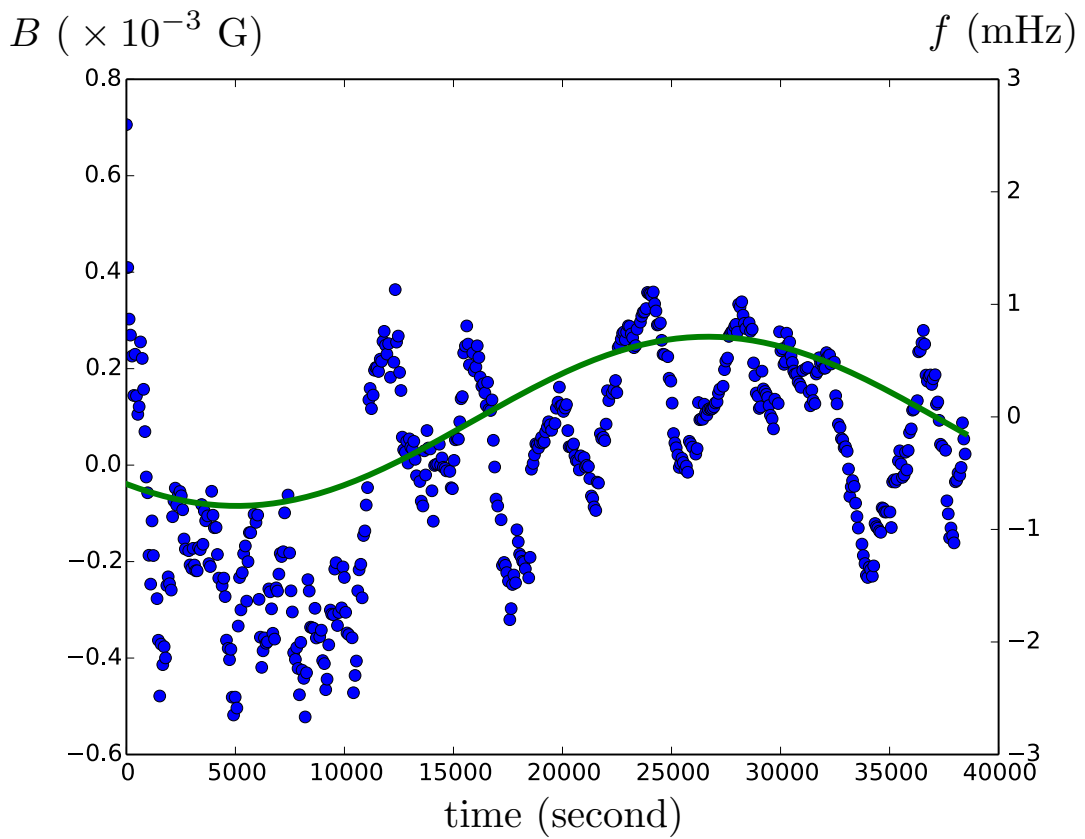


Figure 7-10: Variation in the magnetic field from the mean value of 3.929 G observed for 12 hours. The right vertical axis provides a correction to the frequency shift due to the quadratic Zeeman effect. To see the effect of drifts in the magnetic field on the final Lorentz violation signal (which has a period of 12 hours), we fit the magnetic data with a sine function with a period of 12 hours. The fit yields the amplitude of the frequency variation to be 0.75(4) mHz.

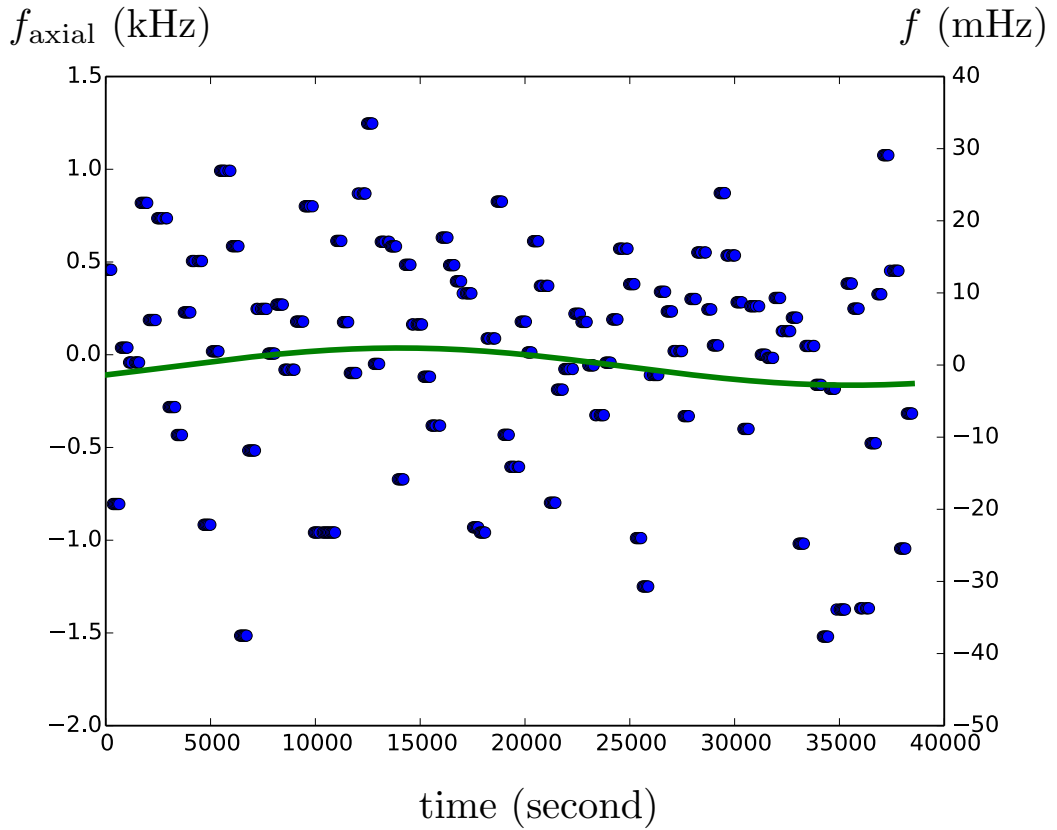


Figure 7-11: Variation in the axial trap frequency from the mean value of 210.4 kHz observed for 12 hours. The right vertical axis provides a correction to the frequency shift due to the electric quadrupole shift. Similar to the magnetic field in Fig. 7-10, we fit the axial trap frequency data with a period of 12 hours to see its effect on the final Lorentz violation signal. The fit yields the amplitude of the parity oscillation frequency variation to be 3(1) mHz.

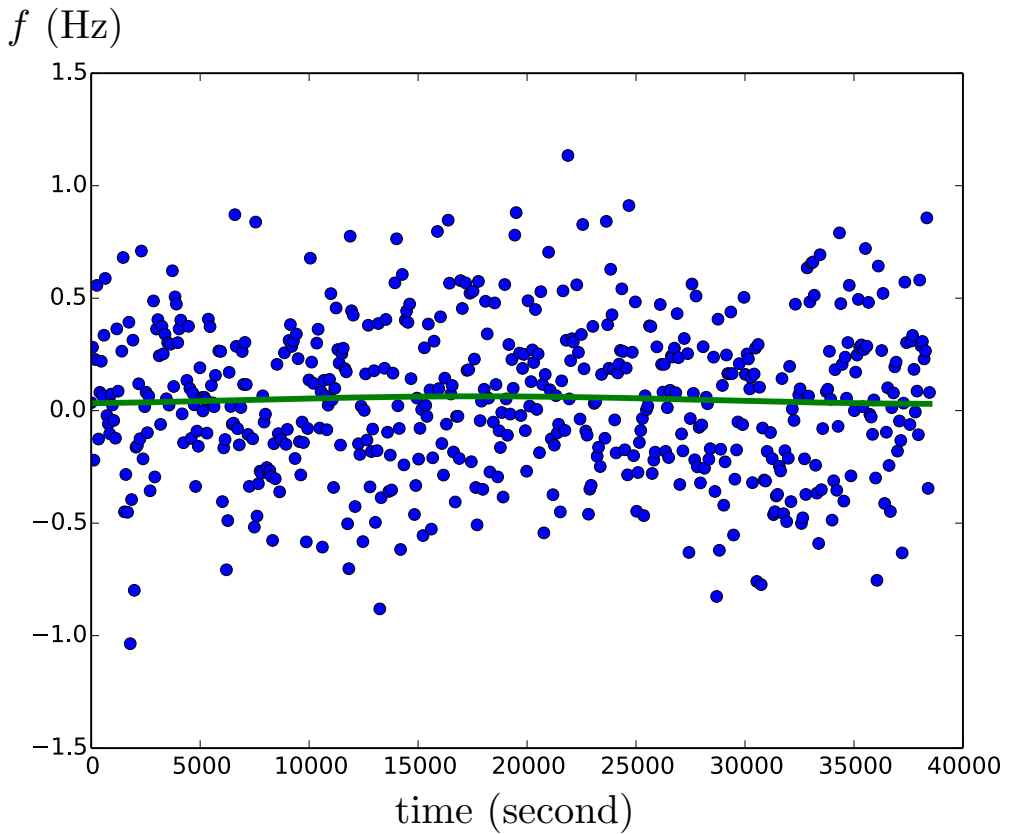


Figure 7-12: Variation in the frequency of the quadrupole shift of the ions observed for 12 hours. The fit gives a 12-hour oscillation period with an amplitude of  $17 \pm 22$  mHz.

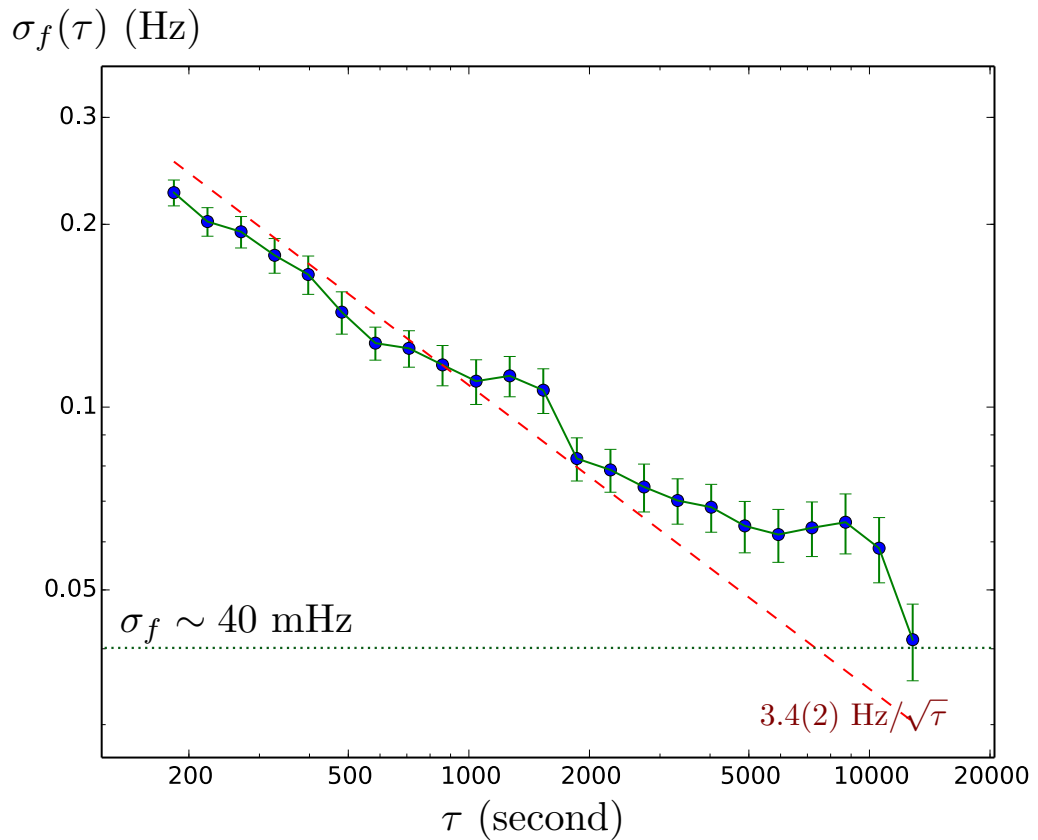


Figure 7-13: Allan deviation of the frequency calculated from the phase data shown in Fig. 7-12. Deviations from the linear fit are likely caused by some other systematics that we have not accounted for.



# Chapter 8

## Quantum simulation of the Frenkel-Kontorova model

In this chapter, we investigate the prospect of using a trapped linear ion chain superimposed with an optical lattice to study an interface between two periodic structures with two arbitrary lattice constants. This model is known as the Frenkel-Kontorova model. We show numerically that, using realistic experimental parameters, the signature of the Aubry transition is still observable despite a deviation from an ideal Frenkel-Kontorova model. This model is also useful in describing how friction works in the nano-scale regime. We present an experimental scheme one might use to study the physics of nano-friction using trapped ions.

### 8.1 The Frenkel-Kontorova model

The Frenkel-Kontorova (FK) model is a simple one-dimensional model where particles of equal masses, joined together by identical springs, are subjected to an external periodic potential of an arbitrary period, as shown in Fig. 8-1. The original model describes a system with infinite number of particles [86]. The Hamiltonian of the system is described by

$$H = \sum_i \left[ \frac{1}{2}m\dot{x}_i^2 + \frac{1}{2}k(x_i - x_{i-1} - a)^2 + K \cos\left(\frac{2\pi x_i}{\lambda}\right) \right], \quad (8.1)$$

where  $m$  is the mass of each particle,  $k$  is the spring constant,  $x_i$  is the position of the  $i$ -th particle,  $K$  is the strength of the external periodic potential with a period of  $\lambda$  and  $a$  is the unperturbed lattice spacing of the chain. The behavior of the system is governed by the magnitude of  $K$  and the ratio  $\lambda/a$ .

Let's look at the two limiting cases of the FK model as depicted in Fig. 8-2. For a very weak external potential strength ( $K \rightarrow 0$ ), obviously the ground state of the system is a chain of equally spaced particles with a lattice constant  $a$ . The dynamics of the chain can be described by rudimentary waves dynamics. We can call this case a “sliding” phase because the particle chain can glide over the external potential without

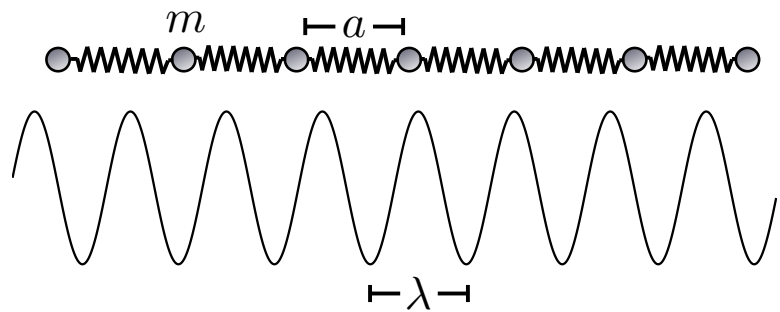


Figure 8-1: The Frenkel-Kontorova model. Each pair of particles with masses  $m$  is held together by a spring such that the lattice constant is given by  $a$ . The external periodic potential has a period of  $\lambda$ .

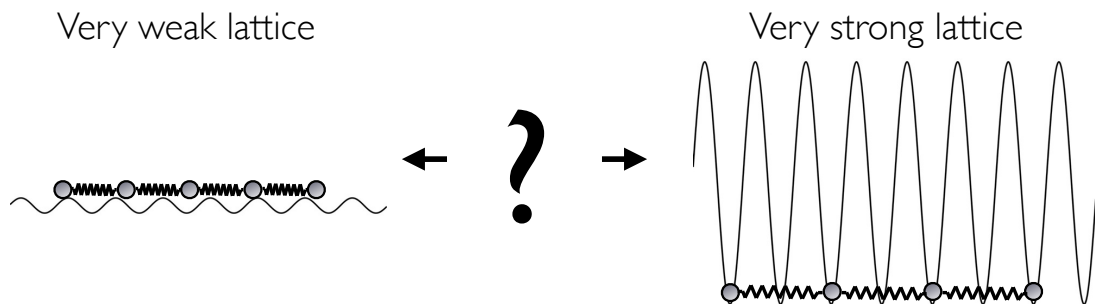


Figure 8-2: Left: system with a very weak external potential. Right: system with a very strong external potential. The intermediate regime which bridges the two extreme cases is the main subject of Aubry's study in his seminal paper [85].

any difficulty. However, for a very strong external potential strength ( $K \rightarrow \infty$ ), all the particles are found at the minima of the external potential. Each particle behaves approximately as an independent oscillator with a local oscillation frequency given by the curvature of the external potential. The spacing between particles is a multiple of  $\lambda$ . We call this case a “pinned” phase since each particle is locked by the external potential.

Clearly the behavior of the system is very different in the two extreme cases. The next interesting question to ask is how does the system transition from the “sliding” to the “pinned” phase as we increase the value of  $K$ ? It is clear that there is a critical value  $K_c$  where the particle chain becomes pinned by the external potential. This is called in the literature later on as the Aubry structural phase transition. Serge Aubry studied this problem in 1983 and found the characteristic of this sliding-to-pinned structural phase transition depends strongly on the ratio  $\lambda/a$  [85]. If  $\lambda/a$  is a rational number, then the system is commensurate and  $K_c = 0$ . However, if  $\lambda/a$  is irrational, the system is incommensurate and  $K_c \neq 0$ . This is striking because it means that the system is in a sliding phase even with a finite small external potential [87, 88].

To see the onset of the structural phase transition in the FK model, we first find the equilibrium positions of the particles by solving

$$\frac{\partial H}{\partial x_i} = k(-x_{i+1} + 2x_i - x_{i-1}) - \frac{2\pi K}{\lambda} \sin\left(\frac{2\pi x_i}{\lambda}\right) = 0. \quad (8.2)$$

This set of equations can be written in a form of an area-preserving map

$$\begin{bmatrix} x_{i+1} \\ x_i \end{bmatrix} = T \begin{bmatrix} x_i \\ x_{i-1} \end{bmatrix} = \begin{bmatrix} 2x_i - \kappa \sin\left(\frac{2\pi x_i}{\lambda}\right) - x_{i-1} \\ x_i \end{bmatrix}, \quad (8.3)$$

where  $\kappa = 2\pi K/\lambda k$ . To use this map, we first pick an ion and denote the position of that ion (modulo  $\lambda$ ) to be  $x_0$ . Next we pick the position of the adjacent ion and denote that to be  $x_1$ . Subsequent ion positions can be generated by repeatedly applying the mapping in Eq. (8.3) to the initial positions  $[x_0, x_1]$ . We generate maps of different values of  $\kappa$  in Fig. 8-3. For a weak external potential ( $|\kappa| = 0.1$ ), most of the trajectories in the map are well-defined separated lines called “dense curves.” According to Aubry, a dense curve, which is a curve consists of points infinitesimally close to each other, in the map represents an incommensurate phase of the system. We interpret this dense curve as a sliding phase configuration since it does not cost any energy to traverse along the trajectory in the map. As the value of  $\kappa$  increases, more and more dense curves are destroyed and eventually no dense curve is observed in the map for  $|\kappa| = 0.9$ . The last dense curve that survives is the last incommensurate configuration. This turns out to be the configuration with a golden ratio  $\lambda/a = (1 + \sqrt{5})/2$ . In this case,  $\kappa_c \sim 0.972$  [89, 90].<sup>1</sup> It is no surprise that this particular

---

<sup>1</sup>If the last dense curve is destroyed at  $\kappa_c \sim 0.972$ , why don’t we see any curve for  $|\kappa| = 0.9$  in Fig. 8-3? This is because to generate such curve, we have to pick a very specific set of initial positions. This is very challenging in a computer where essentially every number is rational.

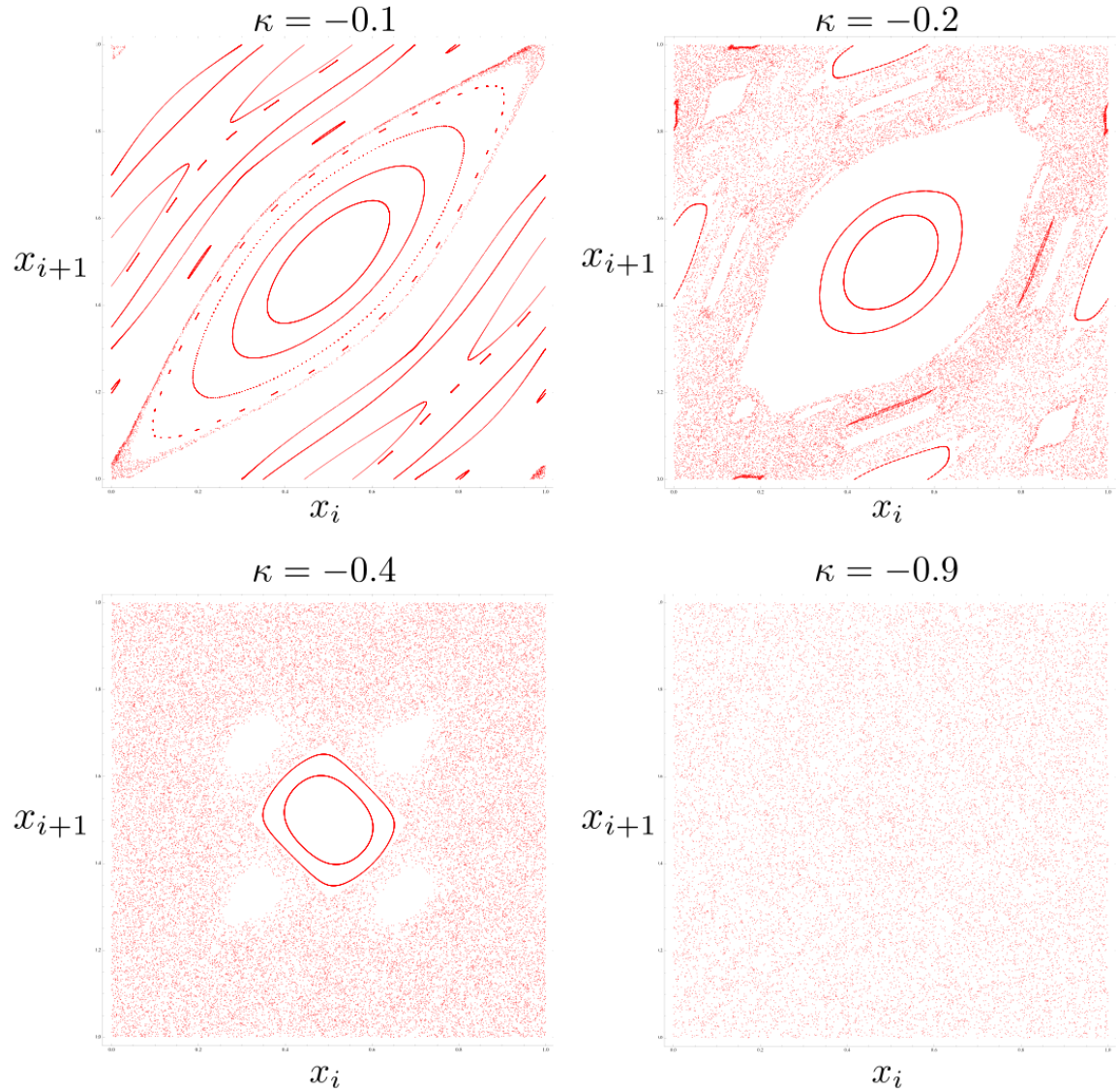


Figure 8-3: Maps generated using Eq. (8.3) for different values of  $\kappa$ . At small value of  $\kappa$ , most of the trajectories in the map look like well-connected lines. For large value of  $\kappa$ , most of the region in the map consists of randomly scattered points which represent chaotic trajectories in the map.

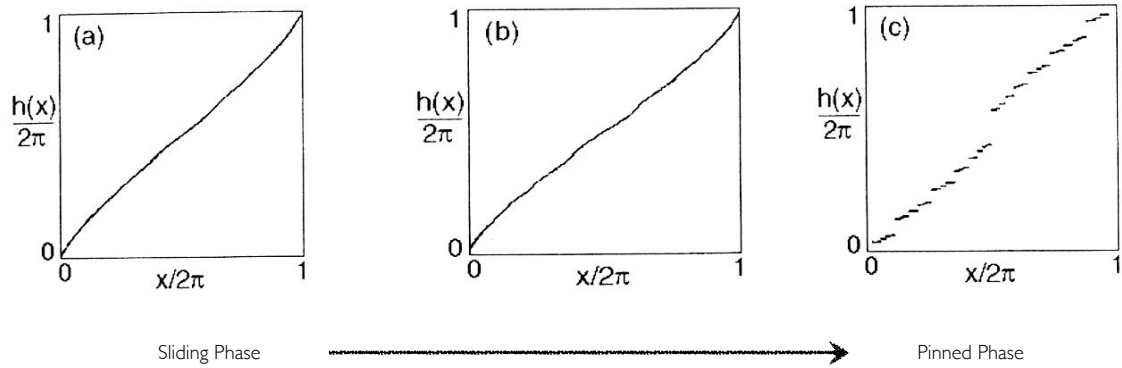


Figure 8-4: The hull function of the incommensurate FK model in different phases. The figure is taken from [91].

value of  $\lambda/a$  gives the last dense curve since the golden ratio is the “most irrational” number defined by a continued fraction

$$\frac{1 + \sqrt{5}}{2} = 1 + \frac{1}{1 + \frac{1}{1 + \dots}}. \quad (8.4)$$

While the area-preserving map in Eq. (8.3) can be used to characterize the phase of any configuration of the system, it is more convenient to describe the phase using an order parameter similar to other kinds of phase transition. One possible definition of the order parameter is to use the so-called hull function,  $h(x)$ . The hull function is a collection of particle positions with respect to the phase<sup>2</sup> of the external periodic potential. We consider only the case of an incommensurate system (sliding phase). For  $\kappa \rightarrow 0$ , since the ratio  $\lambda/a$  is an irrational number, the particles in the system sample equally every possible phase of the external periodic potential. This is shown in the leftmost plot in Fig. 8-4. As the value of  $\kappa$  increases, if the system is still in a sliding phase, the hull function is still continuous. However, if  $\kappa$  is large enough (and the system is in a pinned phase), the hull function becomes discontinuous and we see clearly the gap in the middle. This is because, for large  $\kappa$ , particles are not found near the top of the external potential. We use this gap in the middle of the hull function as an order parameter which quantify the phase of the system. When this gap is zero, the system is in a sliding phase. When this gap is non-zero, the system is in a pinned phase.

Additionally, there have been many studies that consider the FK model in the quantum mechanical regime [21, 92, 93, 94, 95, 96]. By introducing quantum fluctuations into the system, the Aubry transition becomes less sharp compared to the classical model. However, distinct features between the sliding and the pinned in

---

<sup>2</sup>Not to be confused with the term “phase” in the phase transition.

the quantum FK model are still observable when looking at the wave-function of the particles in the chain. For instance, Borgonovi *et al.* show in Ref. [21] that the hull function, which in the quantum case plots the expectation value of the particle position with respect to the phase of the external period potential, can still be used to distinguish between the two structural phases.

## 8.2 Numerical simulation of the Frenkel-Kontorova model with trapped ions

We discuss now how a long string of trapped ions can be used to study the FK model. We can realize the external periodic potential using an optical lattice with a period defined by the wavelength of the light in the cavity. The strength of the perturbation is governed by the AC Stark effect [14, 97]. A possible experimental setup is shown in Fig. 8-5. The FK model with ions (FKI) is more complicated than the FK model in Eq. (8.1) because of the long range Coulomb interactions between ions. The Hamiltonian of the system is given by

$$H = \sum_i \left[ \frac{1}{2} m \dot{x}_i^2 + \frac{1}{2} m \omega_{\text{axial}}^2 x_i^2 + K \cos \left( \frac{2\pi x_i}{\lambda} \right) \right] + \sum_{i < j} \left[ \frac{e^2}{4\pi\epsilon_0 |x_j - x_i|} \right]. \quad (8.5)$$

The axial trapping potential and mutual Coulomb interactions act like springs connecting the ions. The lattice constant analogous to  $a$  in Eq. (8.1) is not well-defined in the FKI model because the ion-ion spacing is not a constant. Ions are more closely spaced near the center of the trap and spreaded out toward the end of the ion chain (see Fig. 2-6). García-Mata *et al.* suggested that we consider only the middle part of the ion chain where the spacing can be approximated to be homogeneous [14]. Despite a departure from an ideal FK model, they found a clear distinct signature between the sliding phase and the pinned phase of the ion chain. Another approach is to shape the axial potential such that the ions are spaced equally, which can be easily done in a planar trap since more electrodes are typically available for fine tuning the shape of the axial potential.

We saw from the previous section that the sliding phase is least perturbed by the external potential when the ratio between the lattice constant and the period of the external potential is given by the golden ratio ( $\sim 1.618$ ), which is assumed by both García-Mata *et al.* [14] and Benassi *et al.* [97]. Typical ion-ion spacing in a trap with an axial frequency of  $\sim 1$  MHz is about  $5 \mu\text{m}$ . This means that the wavelength of the light in the optical lattice is also on the order of  $\mu\text{m}$ . Laser light at this wavelength is far detuned from the atomic transitions of any ion species used in most trapped ion experiments (which are usually at optical wavelengths), making the strength of the external potential very weak compared to the Coulomb interaction between ions. To observe the Aubry transition, we estimate that one would need a laser power on the order of kW.

It is more realistic to use a laser wavelength not too far detuned from the atomic transition to avoid requiring too high power of the optical lattice. For  $^{40}\text{Ca}^+$ , we

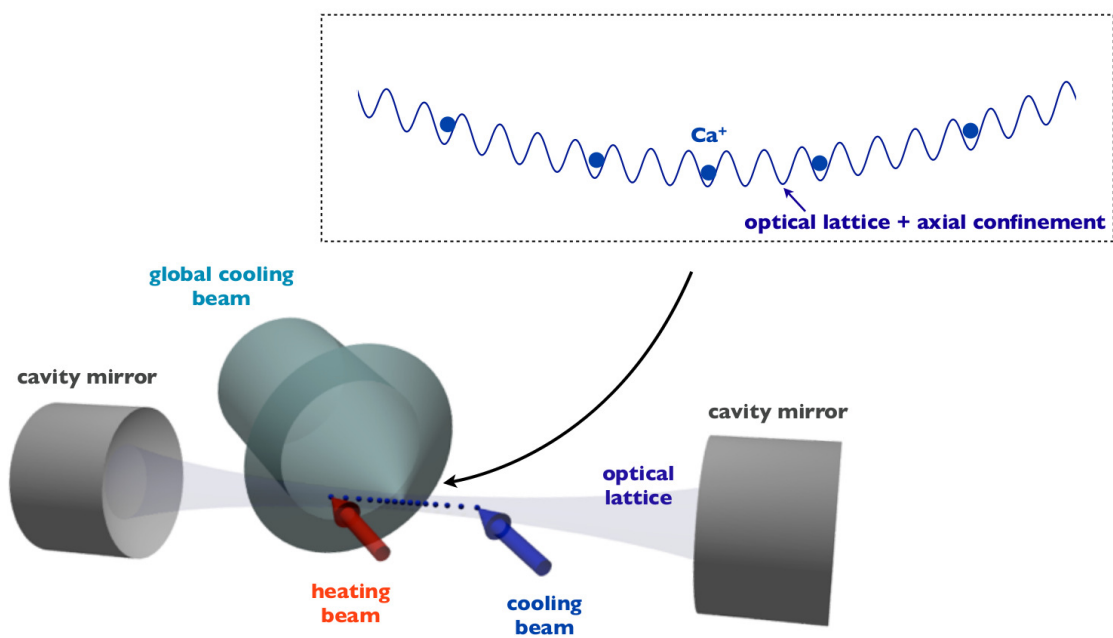


Figure 8-5: Linear chain of ion in an optical lattice created by a standing wave formed by an optical cavity. The ions are trapped with the axial confinement from the RF trap and small microtraps formed by an optical lattice, as shown in the inset.

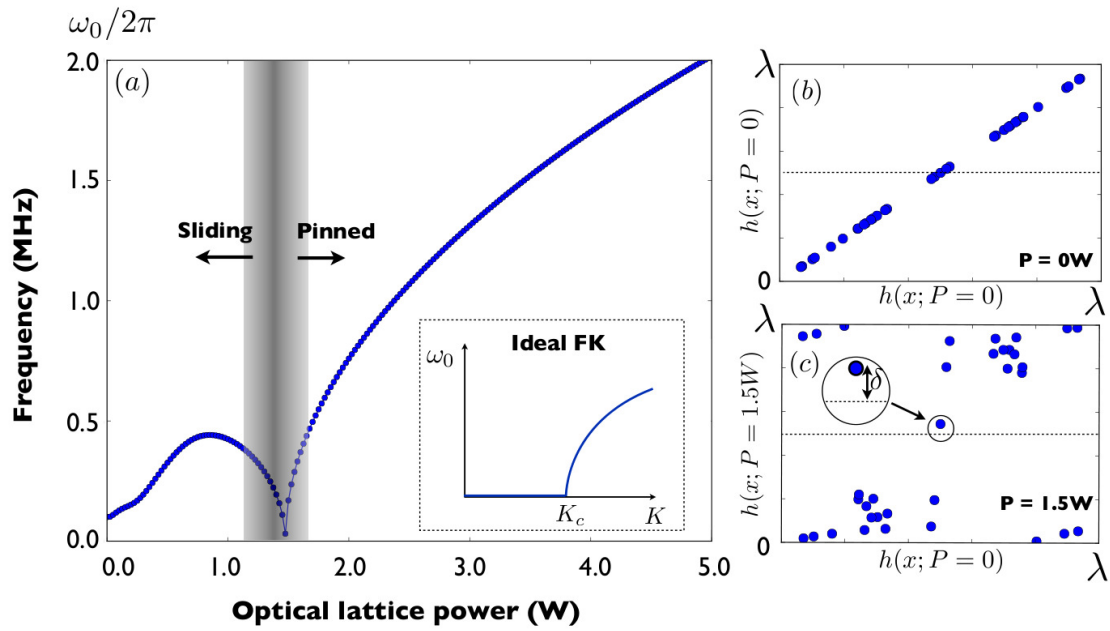


Figure 8-6: Effect of an optical lattice at 405 nm on the ion chain. (a) The frequency of the first normal mode of the ion chain as a function of intra-cavity laser power. The inset shows the case for an ideal FK model. (b) The hull function at zero optical lattice power. (c) The hull function for optical lattice power of 1.5 W.

choose a laser light at 405 nm for an optical lattice. This is because a laser diode at 405 nm is commercially available and typical diodes that capable of producing light at this wavelength can deliver 120 mW of light power easily. We now show that we still see a signature of the Aubry transition despite not having a golden ratio between the ion-ion spacing and the laser wavelength. In our simulations, we use an axial trap frequency of  $f_{\text{axial}} = 100$  kHz with the beam waist of the optical lattice of 25  $\mu\text{m}$ . We assume that there are 35 ions in the chain—a size we have already trapped successfully (see Fig. 2-6).

First we numerically solve for the equilibrium positions of the ions with the Hamiltonian given in Eq. (8.5). We numerically find a solution to a set of equations generated by the conditions  $\partial H / \partial x_i = 0$ . For low optical lattice power, the solution to these equations is unique, which is similar to the case where no optical lattice is present. However, at higher optical lattice power, there is more than one solution. This means that there are many configurations of the ion positions that locally minimize the potential. To truly find the ion positions that globally minimize the potential is computationally intensive. In the experiment, one likely would adiabatically ramp up the optical lattice power from zero. In our simulation, we find the equilibrium positions of the ions at any optical lattice power by gradually increasing the optical lattice power and solve for the equilibrium positions at each lattice power step. For each step, the initial positions of the ions are the equilibrium position from the previous step.

Next, we linearize the system and calculate the normal mode frequencies as a function of the external optical potential power,  $K$ . The normal mode frequencies are the eigenvalues of the coupling matrix  $\partial^2 H / \partial x_i \partial x_j$ . The frequency of the lowest normal mode against the optical lattice power is given in Fig. 8-6. We can see that for  $K > 1.5$  W, the frequency increases monotonically with the optical lattice power. The hull function at  $K = 1.5$  W also shows a clear gap in the middle compared to the case  $K = 0$  W (see Fig. 8-6). An optical lattice power at 1.5 W can be realized with a moderate finesse optical cavity.<sup>3</sup>

The presence of the optical lattice also affects the dynamics of the ions in the chain. If the displacements of the all ions from their equilibrium positions are small, then the system is well described by the normal mode picture. The optical lattice can strongly modify the structure of the normal mode frequencies and thus affects the dynamics of the ion chain. In Fig. 8-7a, we show the normal mode frequencies of the ion chain for different optical lattice powers. At moderate optical lattice power ( $P = 1.5$  W), there exists a large gap between the first and the second normal mode frequencies which in not found in the strong lattice power ( $P = 5.0$  W) or weak lattice power ( $P = 0$  W).

We study the dynamics of the ion chain by means of numerical simulations. We apply a small displacement in the axial direction to one of the outermost (leftmost) ion in the chain and let the system evolve freely. The decomposition of this initial displacement into the normal mode basis is shown in Fig. 8-7b, where we show the

---

<sup>3</sup>In these simulations, we assume that the center ion is at the maximum of the optical lattice.

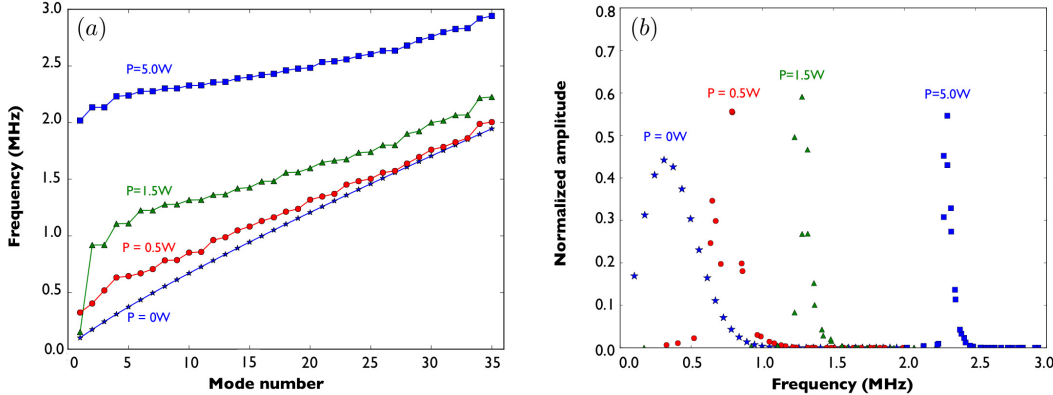


Figure 8-7: The effect of the optical lattice on the mode structure of the ion chain. (a) Frequencies of the normal modes for different optical lattice powers. (b) Mode distribution for when only the first ion is displaced for different optical lattice powers.

normal mode decomposition of the initial state for different optical lattice powers.<sup>4</sup> We look at the kinetic energy of the ion on the other end of the chain (rightmost) as a function of the free evolution of the kicked system (see Fig. 8-8).

An interesting observation can be made regarding the so-called the “turn-around” time, which is defined by the time when the last ion acquires the maximum energy. Fig. 8-8a shows the time evolutions of the rightmost ion for different ion number without any external optical lattice. The “turn-around” time, which is indicated by a grey line in the plot, does not seem to depend on the number of the ions. This is a special feature of long-range Coulomb interactions among ions in the chain. With more ions in the chain, while the length of the chain increases, the coupling rate between ions also increase due to the ions being closer to each other. These two effects cancel out and thus the “turn-around” time has only a weak dependence on the ion number. The dynamics of the ion crystal similar to the simulations here is explored more deeply in Michael Ramm’s thesis for radial excitations of ion strings.

Next we look at the time evolution of the energy of the rightmost ion for different optical lattice powers. This is shown in Fig. 8-8b to Fig. 8-8e. For  $P = 0$  W, the time evolution shows no obvious pattern. However, at  $P = 0.5$  W, the mode structure is heavily altered and the time evolution shows a distinctive pattern. As we increase the optical lattice power further, the ions are pinned to the optical lattice minima and the coupling between ions becomes relatively weaker.

### 8.3 Using trapped ions to study nano-scale friction

The origin of friction that we experience in daily life is still not well understood from the microscopic point of view [98, 99]. This is extremely important in designing

---

<sup>4</sup>For larger excitation, the normal mode picture does not hold because of the non-linearity of the Coulomb interaction.

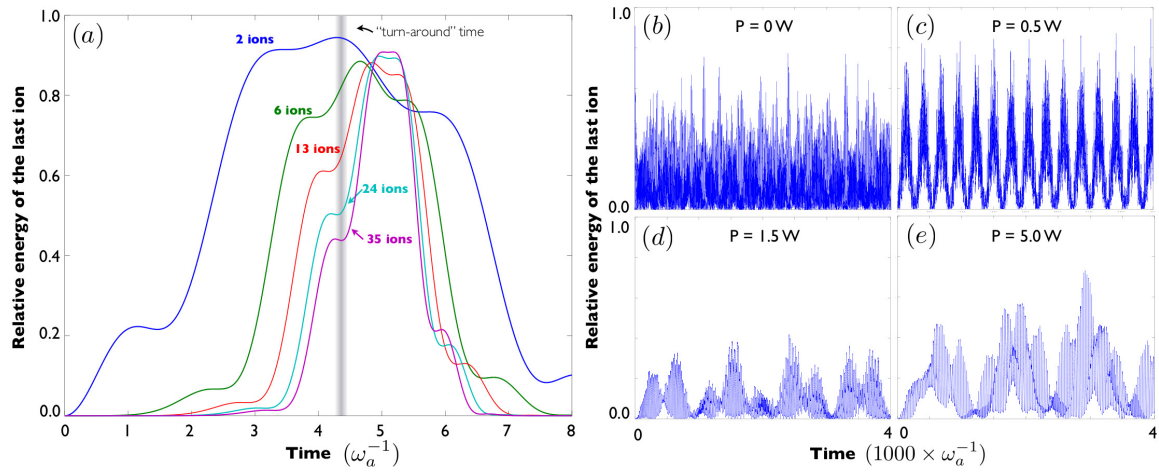


Figure 8-8: Dynamics of the last ion in a chain with different optical lattice power when the first ion is kicked. (a) The position of the last ion for different number of ions in the chain with no optical lattice. (b-e) Time evolutions of the last ion for different optical lattice powers. The horizontal axis displays time in a unit of the inverse of the axial trap frequency,  $\omega_a^{-1}$ .

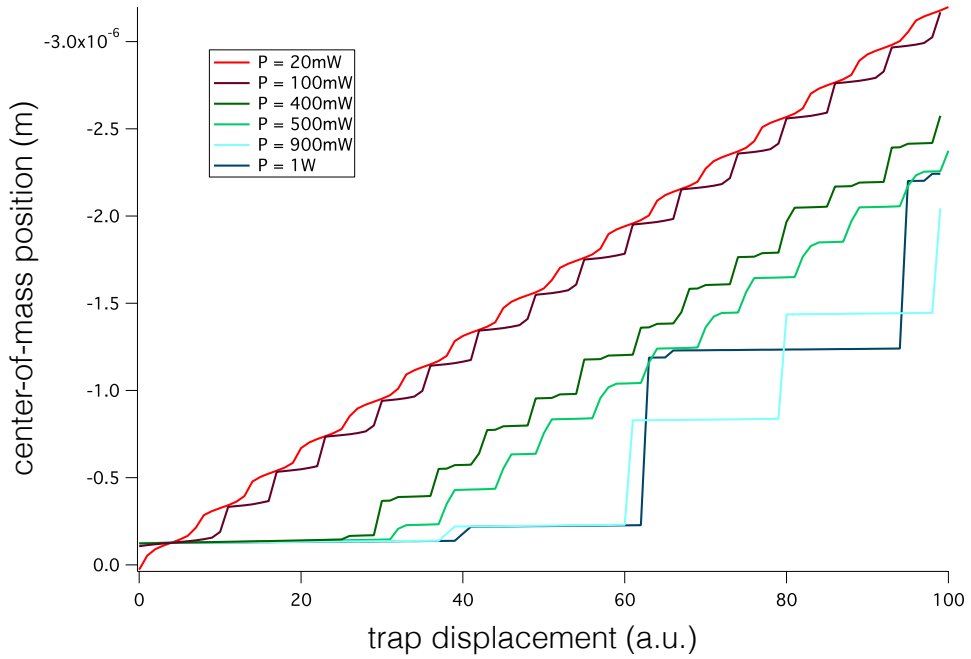


Figure 8-9: Center-of-mass position of the chain as a function of the axial tilting of the trap ( $\gamma$ ) for different optical lattice powers.

nano-scale machines. Recently, there has been a proposal that combines the field of nano-scale friction and trapped ions [97, 100]. Usually, experimental investigations of nano-scale friction are done using atomic force microscopy (AFM) to probe the surface of materials (for example, see Ref. [101, 102]). Since the level of control over experimental parameters of trapped ions is exceptional, using trapped ions to study nano-scale friction will hopefully provide a fresh look into this old physics problem of friction. The two interfaces are modeled using the ion chain interaction with the periodic potential of an optical lattice similar to the FK model presented in the previous section. Here we show a numerical simulation that demonstrates how we might perform experiments to study nano-friction.

The most natural way to study friction is to displace the two interfaces with respect to each other by means of applying a shear force and measure their responses. Experimentally, we can easily displace the position of the ion chain along the optical lattice axis by applying voltages to the endcaps of the trap. The Hamiltonian of the system, which is given in Eq. (8.5), has then an additional tilting term:

$$V = \sum_i \left[ \frac{1}{2} m \omega_{\text{axial}}^2 x_i^2 + \gamma x_i + K \cos \left( \frac{2\pi x_i}{\lambda} \right) \right] + \sum_{i < j} \left[ \frac{e^2}{4\pi\epsilon_0 |x_j - x_i|} \right]. \quad (8.6)$$

The parameter  $\gamma$  is the amount of pull what we apply to the ion chain. For each  $\gamma$ , we calculate the equilibrium position of each ion in a 20-ion chain with an optical lattice parameters similar to what we use in the previous section. The center-of-mass position of the ion chain as a function of the amount of drag is shown in Fig. 8-9 for different optical lattice powers. We see that for small optical lattice powers (red and brown curves in the figure) the chain glides over the optical lattice without being pinned down by the lattice. In this sense, the name “sliding” phase is appropriate since it does not require a large magnitude of force to displace the ion chain. On the other hand, with large optical lattice powers (blue and dark blue curves in the figure) the chain gets stuck on the lattice most of the time (horizontal lines). Then the chain jumps over this barrier with a large displacement and gets stuck again. This “slip-stick” mechanism of a trapped ion chain over an optical lattice is also studied numerically in depth by Mandelli *et al.* [100]. Here, we show that such an effect can be observed with reasonable optical lattice power and wavelengths. Our numerical simulation, however, does not take into account a finite motion of the ions due to finite temperature of the ion crystal. This effect, together with an instability of the axial confinement, can cause the ions to hop to adjacent lattice site and blur-out the “slip-stick” motion of the chain.

## 8.4 Experimental progress toward realizing the FK model with trapped ions.

Experimental progress toward realizing the FK model with trapped ions is underway both in our group and in other ion trapping groups. The effect of localization of the ion motion from an optical lattice has been reported by the Vuletić group at

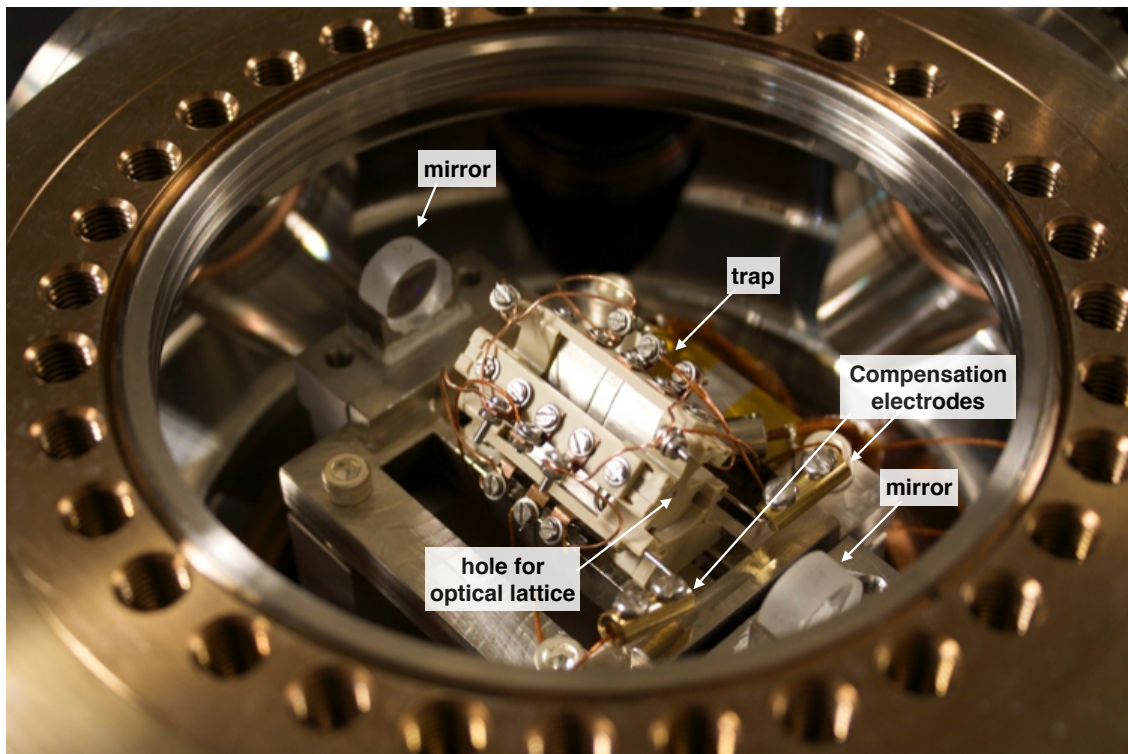


Figure 8-10: Our current trap with an optical cavity for the realization of the FK model. The mirrors which form an optical cavity are placed about 7 cm apart from each other. The holes at the end of the trap is for the optical lattice to enter the trap at the center.

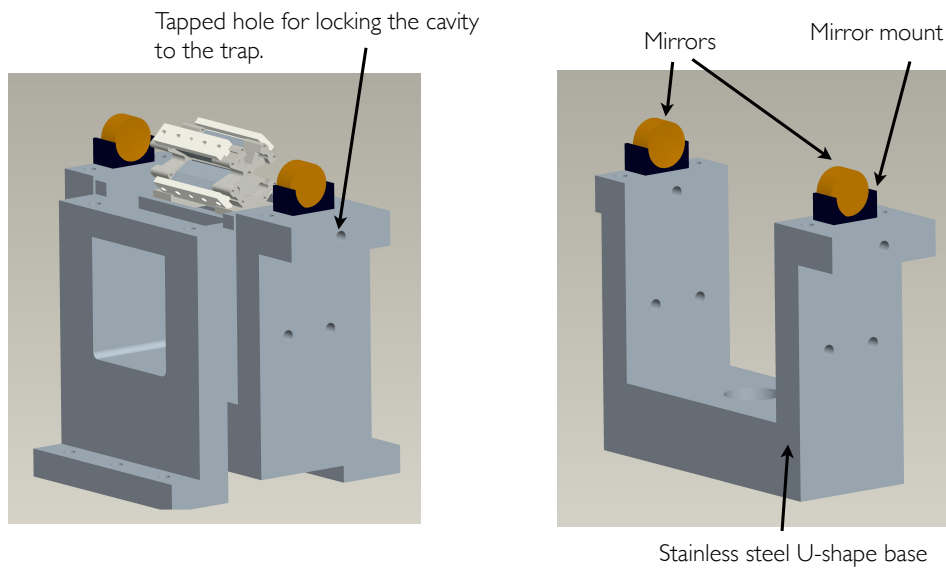


Figure 8-11: Mechanism to align the optical lattice with the trap in-vacuum. Right: a u-shape stainless steel base houses a pair of mirrors that form an optical cavity. Left: the u-shape base can move independently with respect to the trap, which is mounted on another stainless steel base. A tapped hole is for locking the position of the cavity to the trap.

MIT [103]. For our setup, the optical lattice in our first iteration of the experimental system unfortunately did not work well. Here we summarize some problems that arose during our first attempt.

Our main concern is the overlapping of the optical cavity mode with the ions. To increase the intensity of the lattice light, the waist size should be as small as possible. This can be realized by having an optical lattice close to being a concentric configuration. However, in this configuration, the stability of the cavity is very sensitive to the distance between the mirrors, making it difficult to align the mirrors. Moreover, aligning a cavity with a very small waist to the center of the trap is challenging since we cannot predetermine the position of the ion in the trap to be better than a few micrometers. We chose a compromise between the intra-cavity light intensity and beam waist and decided to choose the waist of the optical cavity to be  $35 \mu\text{m}$ . This provides a large enough Rayleigh range for the optical lattice to clear the holes on both ends of the trap, as shown in Fig. 8-10.

To provide an ability to align the optical cavity with the ions after we place both in the vacuum chamber, we use a manipulator-bellow system to separately move the optical lattice mounted on a u-shape stainless steel base as shown in Fig. 8-11. Once the cavity is aligned, we have another manipulator (with a screw-driver attached) to screw and lock the position of the cavity with respect to the trap. Before we baked the vacuum chamber, the whole cavity moving and locking system worked reasonably well. We observed that the position of the cavity moved during the locking process. However, the cavity mode was still visible after the locking of the screw. Tightening of the screw further also exerts a pressure enough to distort the alignment of the mirrors. But with a few trials-and-errors, we found the right amount of tightening to avoid any significant distortion to the structure of the trap and the cavity. Unfortunately, after the vacuum bake-out, we could not observe any mode of the cavity. We suspect that the mirrors were coated with neutral calcium atoms during our attempt to load ions into the trap for during the first couple of months. It is difficult to know exactly the reason for the failure of the cavity until we open up the vacuum chamber and investigate.



# Chapter 9

## Summary and outlook

We have surveyed many aspects of using trapped ions to touch on many branches of physics. First, we perform spectroscopy of the dipole transitions of  $^{40}\text{Ca}^+$  and measure directly the effect of the micromotion on the spectrum of the fluorescence. This is perhaps the most basic form of spectroscopy: scanning the frequency of the probe laser over the atomic transition. We remove interference from the repumpers by switching them off during the probe duration of the spectroscopy laser. Then we measure precisely the branching fractions of the excited state of  $^{40}\text{Ca}^+$  using a simple technique that involves only two lasers. The result obtained has small enough uncertainty to discriminate between different theoretical models. Another atomic property of  $^{40}\text{Ca}^+$  that can be measured precisely is the lifetime of the excited state. We investigate the possibility of using the Hanle effect to measure this quantity. All these measurements extract parameters built into the atomic structure of  $^{40}\text{Ca}^+$ .

Then we use  $^{40}\text{Ca}^+$  as a probe to measure properties of the environment. We can measure the magnetic field strength, magnetic field gradient and electric field gradient precisely using a pair of correlated ions. Performing measurements in a decoherence-free manifold suppresses a fast external magnetic fluctuation and allows exceptional measurement accuracies. We then apply this technique to perform a measurement that directly tests and looks for the violation of local Lorentz invariance.

Finally, we investigate the prospect of using trapped ions as a (quantum or even classical) simulator to study complex systems where simulations in a computer might not be possible. The Frenkel-Kontorova model, with the external perturbing optical lattice, is closely related to the problem of nano-friction, which is one of the oldest physics problems that we do not yet understand well. We show that it is possible to observe various physical features related to the Aubry transition using realistic experimental parameters.

All experiments reported in this thesis have been carried out with the first generation of the Paul trap in our group. Certainly, there are many improvements that can be done to either suppress systematic errors in the measurements or realize some of the experimental plans outlined in the previous chapters. In any case, we list here according to the topics mentioned in this thesis how we can improve the experimental setup and pursue the next stage of the project.

**Spectroscopy on dipole transitions** A frequency comb can reference the frequencies of different laser lights to the 729 nm light, which we can use the ions to determine the absolute frequency with high precision. The transition frequencies of all the dipole transition of  $^{40}\text{Ca}^+$  can then be measured to a precision of less than 200 kHz. This is already competitive with, if not better than, most recent work on measuring dipole transitions in trapped ions [104, 105, 106].

**Measurement of the branching fractions** The main uncertainty currently is the birefringence in the detection optics. With better characterization of all the optics, we certainly can significantly reduce this uncertainty at least 1 or 2 orders of magnitude. To improve the photon counting statistics, a better detector with a higher collection efficiency is needed. Many research groups around the world are currently working on improving the collection efficiency. Optical systems with 100 times more efficient detection as compared to ours have been reported [107, 108, 109]. The experimental scheme demonstrated here can be applied to measure the branching fraction of the  $^2\text{P}_{3/2}$  state and also to other species of ions.

**Observation of the Hanle effect** One limitation of our current setup is the strength of the applied magnetic field. Currently, to apply a suitable magnetic field, the current coil has to be water-cooled. It still creates potential thermal drifts of the experimental setup. With properly placed Helmholtz coils, we have a better control over the direction and the magnitude of the magnetic field. Similar to the branching fractions measurement, a higher collection efficiency will drastically improve the result.

**Spectroscopy with correlated ions** If the measurement is done with an entangled pair of ions instead of just a correlated pair, we gain twice the signal-to-noise ratio. One limitation that prevents us from creating an entangled state with high enough fidelity is our inability to cool ions to the ground state. This is because of an exceptionally high background heating rate. The source of this heating rate is not well understood and one suspect is the fact that we cannot compensate micromotion well enough in the current trap. Performing sideband cooling with Raman beams might circumvent this problem. However, the high background heating rate also requires us to perform sympathetic cooling during the Ramsey time. Having a trap with low heating rate definitely will improve the systematic errors of the measurement tremendously. Also the stability in all electrical equipment that provide the voltages to the endcaps and compensation electrodes can certainly be improved.

**Study of Frenkel-Kontorova model and nano-friction with trapped ions** Certainly, the most important ingredient missing from the current trap is the optical lattice. Integrating an optical lattice with ions has always been challenging, even with a moderate finesse optical cavity. The most demanding task is to align the optical lattice with the center of the trap. One solution is to have additional RF electrodes in the trap to be able to move the RF null to align with the optical lattice. Then there

is a concern with the stability of the optical lattice with respect to the ion. Since the wavelength of the optical lattice is  $\sim 200$  nm, any sub-micron instability of the setup will make the observation of the Aubry transition very difficult. Having a monolithic setup where the mirrors that form the optical lattice and the trap are solidly joined together seem to be a reasonable solution.

**General improvement** Our current trap has a limited optical access which limits the number of laser beams we can use to address the ions. This prevents us from potentially realize a more complex experiments. For example, the experiment with a correlated (or entangled) pair of ions can be done with four ions which required four 729 nm beam paths. In this case, the systematic errors such as the influence of the magnetic field gradient can be canceled out within the same measurement run.



# Bibliography

- [1] F. Schmidt-Kaler, H. Häffner, M. Riebe, S. Gulde, G. P. T. Lancaster, T. Deuschle, C. Becher, C. F. Roos, J. Eschner, and R. Blatt. Realization of the Cirac-Zoller controlled-NOT quantum gate. *Nature* **422**, 408 (2003).
- [2] H. Häffner, C. F. Roos, and R. Blatt. Quantum computing with trapped ions. *Phys. Rep.* **46**, 155 (2008).
- [3] P. Schindler, J. T. Barreiro, T. Monz, V. Nebendahl, D. Nigg, M. Chwalla, M. Hennrich, and R. Blatt. Experimental repetitive quantum error correction. *Science* **332**, 1059 (2011).
- [4] L. M. Duan and C. Monroe. Colloquium: Quantum networks with trapped ions. *Rev. Mod. Phys.* **82**, 1209 (2010).
- [5] T. Rosenband, P. Schmidt, D. Hume, W. Itano, T. Fortier, J. Stalnaker, K. Kim, S. Diddams, J. Koelemeij, J. Bergquist, and D. Wineland. Observation of the  $^1\text{S}_0 \rightarrow ^3\text{P}_0$  Clock Transition in  $^{27}\text{Al}^+$ . *Phys. Rev. Lett.* **98**, 220801 (2007).
- [6] T. Rosenband, D. B. Hume, P. O. Schmidt, C. W. Chou, A. Brusch, L. Lorini, W. H. Oskay, R E Drullinger, T M Fortier, J E Stalnaker, S A Diddams, W C Swann, N R Newbury, W. M. Itano, D. J. Wineland, and J. C. Bergquist. Frequency ratio of  $\text{Al}^+$  and  $\text{Hg}^+$  single-ion optical clocks: metrology at the 17th decimal place. *Science* **319**, 1808 (2008).
- [7] C. F. Roos, M. Chwalla, K. Kim, M. Riebe, and R. Blatt. ‘Designer atoms’ for quantum metrology. *Nature* **443**, 316 (2006).
- [8] N. Fortson. Possibility of measuring parity non-conservation with a single trapped atomic ion. *Phys. Rev. Lett.* **70**, 2383 (1993).
- [9] H. Loh, K. C. Cossel, M. C. Grau, K. K. Ni, E. R. Meyer, J. L. Bohn, J. Ye, and E. A. Cornell. Precision spectroscopy of polarized molecules in an ion trap. *Science* **342**, 1220 (2013).
- [10] C. W. Chou, D. B. Hume, T. Rosenband, and D. J. Wineland. Optical clocks and relativity. *Science* **329**, 1630 (2010).
- [11] R. Feynman. Simulating physics with computers. *Int. J. Theor. Phys.* **21**, 467 (1982).

- [12] M. Greiner, O. Mandel, T. Esslinger, T. W. Hänsch, and I. Bloch. Quantum phase transition from a superfluid to a Mott insulator in a gas of ultracold atoms. *Nature* **415**, 39 (2002).
- [13] J. I. Cirac and P. Zoller. A scalable quantum computer with ions in an array of microtraps. *Nature* **404**, 579 (2000).
- [14] I. García-Mata, O. V. Zhirov, and D. L. Shepelyansky. Frenkel-Kontorova model with cold trapped ions. *Eur. Phys. J. D* **41**, 325 (2007).
- [15] R. Schmied, T. Roscilde, V. Murg, D. Porras, and J. I Cirac. Quantum phases of trapped ions in an optical lattice. *New J. Phys.* **10**, 045017 (2008).
- [16] H. Friedenauer, H. Schmitz, J. T. Glueckert, D. Porras, T. Schaetz, and A. Friedenauer. Simulating a quantum magnet with trapped ions. *Nature Physics* **4**, 757 (2008).
- [17] K. Kim, M.-S. Chang, S. Korenblit, R. Islam, E. E. Edwards, J. K. Freericks, G.-D. Lin, L.-M. Duan, and C. Monroe. Quantum simulation of frustrated Ising spins with trapped ions. *Nature* **465**, 590 (2010).
- [18] R. Islam, E. E. Edwards, K. Kim, S. Korenblit, C. Noh, H. Carmichael, G. D. Lin, L. M. Duan, C. C. J. Wang, J. K. Freericks, and C. Monroe. Onset of a quantum phase transition with a trapped ion quantum simulator. *Nat. Commun.* **2**, 377 (2011).
- [19] J. T. Barreiro, M. Müller, P. Schindler, D. Nigg, T. Monz, M. Chwalla, M. Henrich, C. F. Roos, P. Zoller, and R. Blatt. An open-system quantum simulator with trapped ions. *Nature* **470**, 486 (2011).
- [20] R. Blatt and C. F. Roos. Quantum simulations with trapped ions. *Nature Physics* **8**, 277 (2012).
- [21] F. Borgonovi, I. Guarneri, and DL Shepelyansky. Quantum effects in the Frenkel-Kontorova model. *Phys. Rev. Lett.* **63**, 2010 (1989).
- [22] M. Gessner, M. Ramm, T. Pruttivarasin, A. Buchleitner, H.-P. Breuer, and H. Häffner. Local detection of quantum correlations with a single trapped ion. *Nature Physics* **10**, 105 (2013).
- [23] M. Ramm, T. Pruttivarasin, and H. Häffner. Energy Transport in Trapped Ion Chains. ArXiv: 1312.5786 (2013). (submitted to New J. Phys.)
- [24] T. Pruttivarasin, M. Ramm, and H. Häffner. Direct spectroscopy of the  $^2\text{S}_{1/2}-^2\text{P}_{1/2}$  and  $^2\text{D}_{3/2}-^2\text{P}_{1/2}$  transitions and observation of micromotion modulated spectra in trapped  $^{40}\text{Ca}^+$ . ArXiv: 1312.7617 (2013). (submitted to J. Phys. B: At. Mol. Opt. Phys.)

- [25] M. Ramm, T. Pruttivarasin, M. Kokish, I. Talukdar, and H. Häffner. Precision Measurement Method for Branching Fractions of Excited  $P_{1/2}$  States Applied to  $^{40}\text{Ca}^+$ . *Phys. Rev. Lett.* **111**, 023004 (2013).
- [26] J. Jin and D. Church. Precision lifetimes for the  $\text{Ca}^+$  4p 2P levels: Experiment challenges theory at the 1% level. *Phys. Rev. Lett.* **70**, 3213 (1993).
- [27] M. S. Safronova and U. I. Safronova. Blackbody radiation shift, multipole polarizabilities, oscillator strengths, lifetimes, hyperfine constants, and excitation energies in  $\text{Ca}^+$ . *Phys. Rev. A* **83**, 012503 (2011).
- [28] T. Pruttivarasin, M. Ramm, I. Talukdar, A. Kreuter, and H. Häffner. Trapped ions in optical lattices for probing oscillator chain models. *New J. Phys.* **13**, 075012 (2011).
- [29] W. Paul. Electromagnetic traps for charged and neutral particles. *Rev. Mod. Phys.* **62**, 531 (1990).
- [30] G. Littich. Electrostatic Control and Transport of Ions on a Planar Trap for Quantum Information Processing. Master thesis, ETH Zürich and University of California, Berkeley, (2011).
- [31] D. J. Berkeland, J. D. Miller, J. C. Bergquist, W. M. Itano, and D. J. Wineland. Minimization of ion micromotion in a Paul trap. *J. Appl. Phys.* **83**, 5025 (1998).
- [32] T. Pruttivarasin. Study of low energy Ytterbium atom-ion charge transfer collisions using a surface-electrode trap. Senior thesis course 8, Massachusetts Institute of Technology, (2008).
- [33] A. Kreuter, C. Becher, G. Lancaster, A. Mundt, C. Russo, H. Häffner, C. Roos, W. Hänsel, F. Schmidt-Kaler, R. Blatt, and M. Safronova. Experimental and theoretical study of the 3d<sup>2</sup>D level lifetimes of  $^{40}\text{Ca}^+$ . *Phys. Rev. A* **71**, 32504 (2005).
- [34] M. Chwalla. Precision spectroscopy with  $^{40}\text{Ca}^+$  ions in a Paul trap. Doctoral thesis, University of Innsbruck, (2009).
- [35] W. M. Itano. External-Field Shifts of the Hg Optical Frequency Standard. *J. Res. NIST* **105**, 829 (2000).
- [36] C. J. Foot. *Atomic Physics*. Oxford Univ. Press, (2005).
- [37] D. Leibfried, R. Blatt, C. Monroe, and D. Wineland. Quantum dynamics of single trapped ions. *Rev. Mod. Phys.* **75**, 281 (2003).
- [38] G. Morigi and J. Eschner. Is an ion string laser-cooled like a single ion? *J. Phys. B At. Mol. Opt. Phys.* **36**, 1041 (2003).
- [39] C. F. Roos. Controlling the quantum state of trapped ions. Doctoral thesis, University of Innsbruck, (2000).

- [40] F. Diedrich, J. C. Bergquist, Wayne M. Itano, and D. J. Wineland. Laser Cooling to the Zero-Point Energy of Motion. *Phys. Rev. Lett.* **62**, 403 (1989).
- [41] S. Hooker. *Laser Physics*. Oxford Univ. Press, (2010).
- [42] W. P. Risk, T. R. Gosnell, and A. V. Nurmikko. *Compact Blue-Green Lasers*. Cambridge Univ. Press, Cambridge, (2003).
- [43] M. Sepiol. Stabilization of a 729 nm laser to an ultra-high finesse reference cavity. Master thesis, ETH, Zürich, (2012).
- [44] C. Raab, J. Bolle, H. Oberst, J. Eschner, F. Schmidt-Kaler, and R. Blatt. Diode laser spectrometer at 493 nm for single trapped Ba + ions. *Appl. Phys. B Lasers Opt.* **67**, 683 (1998).
- [45] C. R. Clark, J. E. Goeders, Y. K. Dodia, C. R. Viteri, and K. R. Brown. Detection of single-ion spectra by Coulomb-crystal heating. *Phys. Rev. A* **81**, 043428 (2010).
- [46] V. Batteiger, S. Knünz, M. Herrmann, G. Saathoff, H. Schüssler, B. Bernhardt, T. Wilken, R. Holzwarth, T. Hänsch, and Th. Udem. Precision spectroscopy of the 3s-3p fine-structure doublet in Mg<sup>+</sup>. *Phys. Rev. A* **80**, 022503 (2009).
- [47] M. Herrmann, V. Batteiger, S. Knünz, G. Saathoff, Th. Udem, and T. Hänsch. Frequency Metrology on Single Trapped Ions in the Weak Binding Limit: The 3s<sub>1/2</sub>→3p<sub>3/2</sub> Transition in <sup>24</sup>Mg<sup>+</sup>. *Phys. Rev. Lett.* **102**, 013006 (2009).
- [48] C. Cohen-Tannoudji and J. Dupont-Roc. *AtomPhoton Interactions: Basic Processes and Applications*. Wiley-VCH, New York, (1992).
- [49] B. Sahoo, B. Das, and D. Mukherjee. Relativistic coupled-cluster studies of ionization potentials, lifetimes, and polarizabilities in singly ionized calcium. *Phys. Rev. A* **79**, 1 (2009).
- [50] C. Guet and W. R. Johnson. Relativistic many-body calculations of transition rates for Ca<sup>+</sup>, Sr<sup>+</sup>, and Ba<sup>+</sup>. *Phys. Rev. A* **44**, 1531 (1991).
- [51] S. S. Liaw. Ab initio calculation of the lifetimes of 4p and 3d levels of Ca+. *Phys. Rev. A* **51**, R1723 (1995).
- [52] B. Arora, M. S. Safranova, and C. W. Clark. Blackbody-radiation shift in a Ca+ 43 ion optical frequency standard. *Phys. Rev. A* **76**, 64501 (2007).
- [53] R. Gerritsma, G. Kirchmair, F. Zähringer, J. Benhelm, R. Blatt, and C. F. Roos. Precision measurement of the branching fractions of the 4p 2P3/2 decay of Ca II. *Eur. Phys. J. D* **50**, 13 (2008).
- [54] N. Kurz, M. R. Dietrich, G. Shu, R. Bowler, J. Salacka, V. Mirgon, and B. B. Blinov. Measurement of the branching ratio in the 6P<sub>3/2</sub> decay of Ba II with a single trapped ion. *Phys. Rev. A* **77**, 060501R (2008).

- [55] A. Gallagher and A. Lurio. Optical Detection of Level Crossing in a J=1/2 State. *Phys. Rev. Lett.* **101**, 25 (1963).
- [56] P. Hannaford, P. L. Larkins, and R. M. Lowe. Radiative lifetimes and branching ratios for the 6 2 P 0 levels of gold. *J. Phys. B: At. Mol. Phys.* **14**, 2321 (1981).
- [57] V. Fivet, P. Quinet, É. Biémont, and H. L. Xu. Transition probabilities and lifetimes in gold Au I and Au II. *J. Phys. B: At. Mol. Opt. Phys.* **39**, 3587 (2006).
- [58] J. Migdalek and M. Garmulewicz. The relativistic ab initio model potential versus Dirac-Fock oscillator strengths for silver and gold isoelectronic sequences. *J. Phys. B: At. Mol. Opt. Phys.* **33**, 1735 (2000).
- [59] D. K. Nandy, Y. Singh, B. K. Sahoo, and C. Li. Sc III spectral properties of astrophysical interest. *J. Phys. B: At. Mol. Opt. Phys.* **44**, 225701 (2011).
- [60] A. Gallagher. Oscillator Strengths of Ca II, Sr II, and Ba II. *Phys. Rev.* **157**, 24 (1967).
- [61] J. E. Sansonetti. Wavelengths, Transition Probabilities, and Energy Levels for the Spectra of Strontium Ions Sr II through Sr XXXVIII. *J. Phys. Chem. Ref. Data* **41**, 013102 (2012).
- [62] R. Pal, D. Jiang, M. Safranova, and U. Safranova. Calculation of parity-nonconserving amplitude and other properties of Ra+. *Phys. Rev. A* **79**, 062505 (2009).
- [63] O. O. Versolato, L. W. Wansbeek, G. S. Giri, J. E. van den Berg, D. J. van der Hoek, K. Jungmann, W. L. Kruithof, C. J. G. Onderwater, B. K. Sahoo, B. Santra, P. D. Shidling, R. G. E. Timmermans, L. Willmann, and H. W. Wilschut. Atomic parity violation in a single trapped radium ion. *Hyperfine Interact.* **199**, 9 (2011).
- [64] V. A. Dzuba and V. V. Flambaum. Calculation of nuclear-spin-dependent parity nonconservation in sd transitions of Ba<sup>+</sup>, Yb<sup>+</sup>, and Ra<sup>+</sup> ions. *Phys. Rev. A* **83**, 052513 (2011).
- [65] G. Moruzzi and F. Strumia. *The Hanle Effect and Level-Crossing Spectroscopy*. Springer, (1991).
- [66] A. Gallagher and A. Lurio. Thallium Oscillator Strengths and 6d<sup>2</sup> D<sub>3/2</sub> State hfs. *Phys. Rev.* **136**, A87 (1964).
- [67] W. W. Smith and A. Gallagher. Radiative Lifetime of the First <sup>2</sup>P<sub>3/2</sub> State of Ionized Calcium and Magnesium by the Hanle Effect. *Phys. Rev.* **145**, 26 (1966).
- [68] L. Hunter, G. Watson, D. Weiss, and A. Zajonc. High-precision measurement of lifetimes and collisional decay parameters in Ca <sup>1</sup>D states using the two-photon Hanle effect. *Phys. Rev. A* **31**, 2268 (1985).

- [69] G. W. Series. Radio-frequency spectroscopy of excited atoms. *Reports Prog. Phys.* **22**, 280 (1959).
- [70] P. Franken. Interference Effects in the Resonance Fluorescence of “Crossed” Excited Atomic States. *Phys. Rev.* **121**, 508 (1961).
- [71] M. Rose and R. Carovillano. Coherence Effects in Resonance Fluorescence. *Phys. Rev.* **122**, 1185 (1961).
- [72] K. Arnett, S. Smith, R. Ryan, T. Bergeman, H. Metcalf, M. Hamilton, and J. Brandenberger. Hanle effect in spectrally broadened light. *Phys. Rev. A* **41**, 2580 (1990).
- [73] D. Budker, D. Kimball, and D. DeMille. *Atomic physics: An exploration through problems and solutions*. Oxford Univ. Press, 2nd edition, (2008).
- [74] J. L. Picque. Hanle effect in an atomic beam excited by a narrow-band laser. *J. Phys. B At. Mol. Phys.* **11**, L59 (1978).
- [75] A.V. Papoyan, M. Auzinsh, and K. Bergmann. Nonlinear Hanle effect in Cs vapor under strong laser excitation. *Eur. Phys. J. D - At. Mol. Opt. Phys.* **21**, 63 (2002).
- [76] J. Mahnke, S. Kulas, I. Geisel, S. Jöllenbeck, W. Ertmer, and C. Klempert. Microwave sidebands for laser cooling by direct modulation of a tapered amplifier. *Rev. Sci. Instrum.* **84**, 063110 (2013).
- [77] R. Blatt and D. Wineland. Entangled states of trapped atomic ions. *Nature* **453**, 1008 (2008).
- [78] G. Kirchmair, J. Benhelm, F. Zähringer, R. Gerritsma, C. F. Roos, and R. Blatt. Deterministic entanglement of ions in thermal states of motion. *New J. Phys.* **11**, 23002 (2009).
- [79] M. Chwalla, K. Kim, T. Monz, P. Schindler, M. Riebe, C. F. Roos, and R. Blatt. Precision spectroscopy with two correlated atoms. *Appl. Phys. B* **89**, 483 (2007).
- [80] M. Maggiore. *A Modern Introduction to Quantum Field Theory*. Oxford Univ. Press, (2005).
- [81] V. Kostelecký and C. Lane. Constraints on Lorentz violation from clock-comparison experiments. *Phys. Rev. D* **60**, 116010 (1999).
- [82] M. Smiciklas, J. M. Brown, L. W. Cheuk, S. J. Smullin, and M. V. Romalis. New Test of Local Lorentz Invariance Using a  $^{21}\text{Ne}$ -Rb-K Comagnetometer. *Phys. Rev. Lett.* **107**, 171604 (2011).

- [83] M. A. Hohensee, N. Leefer, D. Budker, C. Harabati, V. A. Dzuba, and V. V. Flambaum. Limits on Violations of Lorentz Symmetry and the Einstein Equivalence Principle using Radio-Frequency Spectroscopy of Atomic Dysprosium. *Phys. Rev. Lett.* **111**, 050401 (2013).
- [84] M. A. Hohensee, H. Müller, and R. B. Wiringa. Equivalence Principle and Bound Kinetic Energy. *Phys. Rev. Lett.* **111**, 151102 (2013).
- [85] S. Aubry. The twist map, the extended Frenkel-Kontorova model and the devil's staircase. *Phys. D Nonlinear Phenom.* **7**, 240 (1983).
- [86] O. M. Braun and Y. S. Kivshar. *The Frenkel-Kontorova Model: Concepts, Methods, and Applications*. Springer-Verlag, Berlin, (2004).
- [87] S. Aubry and P. Y. Le Daeron. The discrete Frenkel-Kontorova model and its extensions. *Physica D* **8**, 381 (1983).
- [88] S. Aubry, R. Mackay, and C. Baesens. Equivalence of uniform hyperbolicity for symplectic twist maps and phonon gap for Frenkel-Kontorova models. *Phys. D Nonlinear Phenom.* **56**, 123 (1992).
- [89] J. M. Greene. A method for determining a stochastic transition. *J. Math. Phys.* **206**, 1183 (1979).
- [90] J.M. Greene, R.S. MacKay, F. Vivaldi, and M.J. Feigenbaum. Universal behaviour in families of area-preserving maps. *Phys. D Nonlinear Phenom.* **33**, 468 (1981).
- [91] R. Black and I. Satija. Universal phase diagram in the generalized Frenkel-Kontorova model. *Phys. Rev. B* **44**, 4089 (1991).
- [92] B. Hu and B Li. Ground-state wave function of the quantum Frenkel-Kontorova model. *Europhys. Lett.* **46**, 655 (1999).
- [93] C.-L. Ho and C.-I. Chou. Simple variational approach to the quantum Frenkel-Kontorova model. *Phys. Rev. E* **63**, 016203 (2000).
- [94] O. V. Zhirov, G. Casati, and D. L. Shepelyansky. Quantum phase transition in the Frenkel-Kontorova chain: From pinned instanton glass to sliding phonon gas. *Phys. Rev. E* **67**, 56209 (2003).
- [95] H.-W. Zhong, Y. Tang, Z. H.-Wei, and T. Yi. Time-Dependent Variational Approach to the Phonon Dispersion Relation of the Commensurate Quantum FrenkelKontorova Model. *Chinese Phys. Lett.* **23**, 1965 (2006).
- [96] B. Hu and J. Wang. Density-matrix renormalization group study of the incommensurate quantum Frenkel-Kontorova model. *Phys. Rev. B* **73**, 184305 (2006).
- [97] A. Benassi, A. Vanossi, and E. Tosatti. Nanofriction in cold ion traps. *Nat. Commun.* **2**, 236 (2011).

- [98] M. Hirano and K. Shinjo. Atomistic locking and friction. *Phys. Rev. B* **41**, 11837 (1990).
- [99] L. Consoli, H. Knops, and A. Fasolino. Onset of Sliding Friction in Incommensurate Systems. *Phys. Rev. Lett.* **85**, 302 (2000).
- [100] D. Mandelli, A. Vanossi, and E. Tosatti. Stick-slip nanofriction in trapped cold ion chains. *Phys. Rev. B* **87**, 195418 (2013).
- [101] A. Podesta, G. Fantoni, and P. Milani. Quantitative nanofriction characterization of corrugated surfaces by atomic force microscopy. *Rev. Sci. Instrum.* **75**, 1228 (2004).
- [102] M. Langer, M. Kisiel, R. Pawlak, F. Pellegrini, G. E. Santoro, R. Buzio, A. Gerbi, G. Balakrishnan, A. Baratoff, E. Tosatti, and E. Meyer. Giant frictional dissipation peaks and charge-density-wave slips at the NbSe<sub>2</sub> surface. *Nat. Mater.* **13**, 173 (2014).
- [103] L. Karpa, A. Bylinskii, D. Gangloff, M. Cetina, and V. Vuletić. Suppression of Ion Transport due to Long-Lived Subwavelength Localization by an Optical Lattice. *Phys. Rev. Lett.* **111**, 163002 (2013).
- [104] A. Wolf, S. van den Berg, W. Ubachs, and K. Eikema. Direct Frequency Comb Spectroscopy of Trapped Ions. *Phys. Rev. Lett.* **102**, 223901 (2009).
- [105] Y. Wan, F. Gebert, J. B. Wübbena, N. Scharnhorst, S. Amairi, I. D. Leroux, B. Hemmerling, N. Lörch, K. Hammerer, and P. O. Schmidt. Precision spectroscopy by photon-recoil signal amplification. *Nat. Commun.* **5**, 3096 (2014).
- [106] C. Hempel, B. P. Lanyon, P. Jurcevic, R. Gerritsma, R. Blatt, and C. F. Roos. Entanglement-enhanced detection of single-photon scattering events. *Nat. Photonics* **7**, 630 (2013).
- [107] A. P. VanDevender, Y. Colombe, J. Amini, D. Leibfried, and D. J. Wineland. Efficient Fiber Optic Detection of Trapped Ion Fluorescence. *Phys. Rev. Lett.* **105**, 023001 (2010).
- [108] G. Shu, N. Kurz, M. R. Dietrich, and B. B. Blinov. Efficient fluorescence collection from trapped ions with an integrated spherical mirror. *Phys. Rev. A* **81**, 042321 (2010).
- [109] E. W. Streed, B. G. Norton, A. Jechow, T. J. Weinhold, and D. Kielpinski. Imaging of Trapped Ions with a Microfabricated Optic for Quantum Information Processing. *Phys. Rev. Lett.* **106**, 010502 (2011).
- [110] E. U. Condon and G. H. Shortley. *The Theory of Atomic Spectra*. Cambridge University Press, (1935).

# Appendix A

## Matrix elements between magnetic sub-levels

In this section we list the matrix elements which are used in calculating interaction between light and a pair of atomic energy levels with the total angular momentum quantum number,  $j$ , and the magnetic quantum number  $m$ .

### A.1 Geometry

We define the coordinates according to Fig. A-1. The polarization vector of the laser is given by

$$\hat{\mathbf{e}} = \hat{\mathbf{i}}(\cos \theta \cos \phi \cos \alpha - \sin \phi \sin \alpha) + \hat{\mathbf{j}}(\cos \theta \sin \phi \cos \alpha + \cos \phi \sin \alpha) + \hat{\mathbf{k}}(-\sin \theta \cos \alpha), \quad (\text{A.1})$$

We can also define

$$e_z = -\sin \theta \cos \alpha \quad (\text{A.2})$$

$$e_- = (\cos \theta \cos \alpha - i \sin \alpha) e^{-i\phi} \quad (\text{A.3})$$

$$e_+ = (\cos \theta \cos \alpha + i \sin \alpha) e^{i\phi}. \quad (\text{A.4})$$

Note that  $e_-^* = e_+$  and

$$e_z^2 + |e_-|^2 = e_z^2 + |e_+|^2 = \sin^2 \theta \cos^2 \alpha + \cos^2 \theta \cos^2 \alpha + \sin^2 \alpha = 1. \quad (\text{A.5})$$

### A.2 General form of the matrix elements

From [110], the matrix elements are

$$\langle \alpha, j, m | \overset{\leftrightarrow}{\mathbf{T}} | \alpha', j+1, m \pm 1 \rangle = \mp \overset{\leftrightarrow}{T}_{j,j+1} \frac{1}{2} \sqrt{(j \pm m + 1)(j \pm m + 2)} (\hat{\mathbf{i}} \pm i \hat{\mathbf{j}}) \quad (\text{A.6})$$

$$\langle \alpha, j, m | \overset{\leftrightarrow}{\mathbf{T}} | \alpha', j+1, m \rangle = \overset{\leftrightarrow}{T}_{j,j+1} \sqrt{(j+1)^2 - m^2} \hat{\mathbf{k}} \quad (\text{A.7})$$

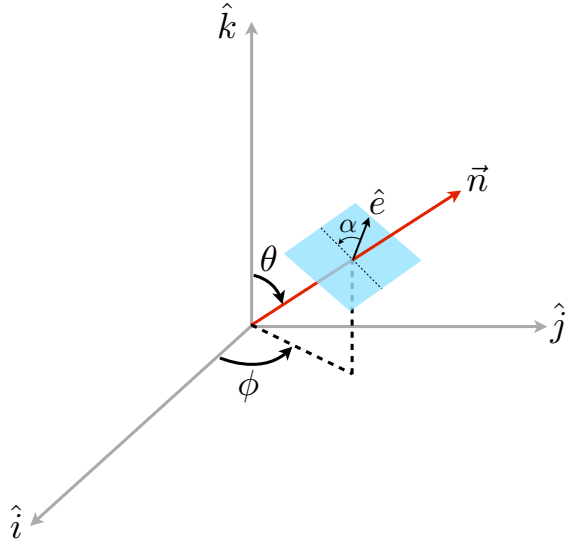


Figure A-1: Coordinate of the direction of light propagation  $\hat{n}$ . The angle  $\alpha$  measure the polarization of the light with respect to the vertical direction.

$$\langle \alpha, j, m | \overleftrightarrow{\mathbf{T}} | \alpha', j, m \pm 1 \rangle = T_{j,j} \frac{1}{2} \sqrt{(j \mp m)(j \pm m + 1)} (\hat{\mathbf{i}} \pm i\hat{\mathbf{j}}) \quad (\text{A.8})$$

$$\langle \alpha, j, m | \overleftrightarrow{\mathbf{T}} | \alpha', j, m \rangle = T_{j,j} m \hat{\mathbf{k}} \quad (\text{A.9})$$

$$\langle \alpha, j, m | \overleftrightarrow{\mathbf{T}} | \alpha', j - 1, m \pm 1 \rangle = \pm T_{j,j-1} \frac{1}{2} \sqrt{(j \mp m)(j \mp m - 1)} (\hat{\mathbf{i}} \pm i\hat{\mathbf{j}}) \quad (\text{A.10})$$

$$\langle \alpha, j, m | \overleftrightarrow{\mathbf{T}} | \alpha', j - 1, m \rangle = T_{j,j-1} \sqrt{j^2 - m^2} \hat{\mathbf{k}}, \quad (\text{A.11})$$

where we write  $\langle \alpha, j | \overleftrightarrow{\mathbf{T}} | \alpha', j' \rangle = T_{j,j'}$ .

### A.2.1 $J = 1/2 \rightarrow J = 1/2$

These are matrix elements for light that couples  $|S_{1/2}\rangle \rightarrow |P_{1/2}\rangle$ :

$$\left\langle \alpha, j = \frac{1}{2}, m = \frac{1}{2} | \overleftrightarrow{\mathbf{T}} | \alpha', j = \frac{1}{2}, m = -\frac{1}{2} \right\rangle = T_{\frac{1}{2},\frac{1}{2}} \frac{1}{2} (\hat{\mathbf{i}} - i\hat{\mathbf{j}}) \quad (\text{A.12})$$

$$\left\langle \alpha, j = \frac{1}{2}, m = -\frac{1}{2} | \overleftrightarrow{\mathbf{T}} | \alpha', j = \frac{1}{2}, m = \frac{1}{2} \right\rangle = T_{\frac{1}{2},\frac{1}{2}} \frac{1}{2} (\hat{\mathbf{i}} + i\hat{\mathbf{j}}) \quad (\text{A.13})$$

$$\left\langle \alpha, j = \frac{1}{2}, m = \frac{1}{2} | \overleftrightarrow{\mathbf{T}} | \alpha', j = \frac{1}{2}, m = \frac{1}{2} \right\rangle = T_{\frac{1}{2},\frac{1}{2}} \frac{1}{2} \hat{\mathbf{k}} \quad (\text{A.14})$$

$$\left\langle \alpha, j = \frac{1}{2}, m = -\frac{1}{2} | \overleftrightarrow{\mathbf{T}} | \alpha', j = \frac{1}{2}, m = -\frac{1}{2} \right\rangle = T_{\frac{1}{2},\frac{1}{2}} (-\frac{1}{2}) \hat{\mathbf{k}}. \quad (\text{A.15})$$

For arbitrary angles,

$$\left\langle \alpha, j = \frac{1}{2}, m = \frac{1}{2} | \overset{\leftrightarrow}{\mathbf{T}} | \alpha', j = \frac{1}{2}, m = -\frac{1}{2} \right\rangle = \overset{\leftrightarrow}{T}_{\frac{1}{2}, \frac{1}{2}} \frac{1}{2} (\cos \theta \cos \alpha - i \sin \alpha) e^{-i\phi} \quad (\text{A.16})$$

$$\left\langle \alpha, j = \frac{1}{2}, m = -\frac{1}{2} | \overset{\leftrightarrow}{\mathbf{T}} | \alpha', j = \frac{1}{2}, m = \frac{1}{2} \right\rangle = \overset{\leftrightarrow}{T}_{\frac{1}{2}, \frac{1}{2}} \frac{1}{2} (\cos \theta \cos \alpha + i \sin \alpha) e^{i\phi} \quad (\text{A.17})$$

$$\left\langle \alpha, j = \frac{1}{2}, m = \frac{1}{2} | \overset{\leftrightarrow}{\mathbf{T}} | \alpha', j = \frac{1}{2}, m = \frac{1}{2} \right\rangle = \overset{\leftrightarrow}{T}_{\frac{1}{2}, \frac{1}{2}} \left( -\frac{1}{2} \right) \sin \theta \cos \alpha \quad (\text{A.18})$$

$$\left\langle \alpha, j = \frac{1}{2}, m = -\frac{1}{2} | \overset{\leftrightarrow}{\mathbf{T}} | \alpha', j = \frac{1}{2}, m = -\frac{1}{2} \right\rangle = \overset{\leftrightarrow}{T}_{\frac{1}{2}, \frac{1}{2}} \frac{1}{2} \sin \theta \cos \alpha. \quad (\text{A.19})$$

### A.2.2 $J = 3/2 \rightarrow J = 1/2$

Similarly, these are matrix elements for light that couples  $|D_{3/2}\rangle \rightarrow |P_{1/2}\rangle$ :

$$\left\langle \alpha, j = \frac{1}{2}, m = \frac{1}{2} | \overset{\leftrightarrow}{\mathbf{T}} | \alpha', j = \frac{3}{2}, m = \frac{3}{2} \right\rangle = \overset{\leftrightarrow}{T}_{\frac{1}{2}, \frac{3}{2}} \left( -\sqrt{\frac{3}{2}} \right) (\hat{\mathbf{i}} + i\hat{\mathbf{j}}) \quad (\text{A.20})$$

$$\left\langle \alpha, j = \frac{1}{2}, m = \frac{1}{2} | \overset{\leftrightarrow}{\mathbf{T}} | \alpha', j = \frac{3}{2}, m = \frac{1}{2} \right\rangle = \overset{\leftrightarrow}{T}_{\frac{1}{2}, \frac{3}{2}} \sqrt{2} \hat{\mathbf{k}} \quad (\text{A.21})$$

$$\left\langle \alpha, j = \frac{1}{2}, m = \frac{1}{2} | \overset{\leftrightarrow}{\mathbf{T}} | \alpha', j = \frac{3}{2}, m = -\frac{1}{2} \right\rangle = \overset{\leftrightarrow}{T}_{\frac{1}{2}, \frac{3}{2}} \sqrt{\frac{1}{2}} (\hat{\mathbf{i}} - i\hat{\mathbf{j}}) \quad (\text{A.22})$$

$$\left\langle \alpha, j = \frac{1}{2}, m = -\frac{1}{2} | \overset{\leftrightarrow}{\mathbf{T}} | \alpha', j = \frac{3}{2}, m = \frac{1}{2} \right\rangle = \overset{\leftrightarrow}{T}_{\frac{1}{2}, \frac{3}{2}} \left( -\sqrt{\frac{1}{2}} \right) (\hat{\mathbf{i}} + i\hat{\mathbf{j}}) \quad (\text{A.23})$$

$$\left\langle \alpha, j = \frac{1}{2}, m = -\frac{1}{2} | \overset{\leftrightarrow}{\mathbf{T}} | \alpha', j = \frac{3}{2}, m = -\frac{1}{2} \right\rangle = \overset{\leftrightarrow}{T}_{\frac{1}{2}, \frac{3}{2}} \sqrt{2} \hat{\mathbf{k}} \quad (\text{A.24})$$

$$\left\langle \alpha, j = \frac{1}{2}, m = -\frac{1}{2} | \overset{\leftrightarrow}{\mathbf{T}} | \alpha', j = \frac{3}{2}, m = -\frac{3}{2} \right\rangle = \overset{\leftrightarrow}{T}_{\frac{1}{2}, \frac{3}{2}} \sqrt{\frac{3}{2}} (\hat{\mathbf{i}} - i\hat{\mathbf{j}}). \quad (\text{A.25})$$

For arbitrary angles,

$$\left\langle \alpha, j = \frac{1}{2}, m = \frac{1}{2} | \overset{\leftrightarrow}{\mathbf{T}} | \alpha', j = \frac{3}{2}, m = \frac{3}{2} \right\rangle = \overset{\leftrightarrow}{T}_{\frac{1}{2}, \frac{3}{2}} \left( -\sqrt{\frac{3}{2}} \right) (\cos \theta \cos \alpha + i \sin \alpha) e^{i\phi} \quad (\text{A.26})$$

$$\left\langle \alpha, j = \frac{1}{2}, m = \frac{1}{2} | \overset{\leftrightarrow}{\mathbf{T}} | \alpha', j = \frac{3}{2}, m = \frac{1}{2} \right\rangle = \overset{\leftrightarrow}{T}_{\frac{1}{2}, \frac{3}{2}} \left( -\sqrt{2} \right) \sin \theta \cos \alpha \quad (\text{A.27})$$

$$\left\langle \alpha, j = \frac{1}{2}, m = \frac{1}{2} | \overset{\leftrightarrow}{\mathbf{T}} | \alpha', j = \frac{3}{2}, m = -\frac{1}{2} \right\rangle = \overset{\leftrightarrow}{T}_{\frac{1}{2}, \frac{3}{2}} \sqrt{\frac{1}{2}} (\cos \theta \cos \alpha - i \sin \alpha) e^{-i\phi} \quad (\text{A.28})$$

$$\left\langle \alpha, j = \frac{1}{2}, m = -\frac{1}{2} | \overset{\leftrightarrow}{\mathbf{T}} | \alpha', j = \frac{3}{2}, m = \frac{1}{2} \right\rangle = \overset{\leftrightarrow}{T}_{\frac{1}{2}, \frac{3}{2}} \left( -\sqrt{\frac{1}{2}} \right) (\cos \theta \cos \alpha + i \sin \alpha) e^{i\phi} \quad (\text{A.29})$$

$$\left\langle \alpha, j = \frac{1}{2}, m = -\frac{1}{2} | \overset{\leftrightarrow}{\mathbf{T}} | \alpha', j = \frac{3}{2}, m = -\frac{1}{2} \right\rangle = \overset{\leftrightarrow}{T}_{\frac{1}{2}, \frac{3}{2}} \left( -\sqrt{2} \right) \sin \theta \cos \alpha \quad (\text{A.30})$$

$$\left\langle \alpha, j = \frac{1}{2}, m = -\frac{1}{2} | \overset{\leftrightarrow}{\mathbf{T}} | \alpha', j = \frac{3}{2}, m = -\frac{3}{2} \right\rangle = \overset{\leftrightarrow}{T}_{\frac{1}{2}, \frac{3}{2}} \sqrt{\frac{3}{2}} (\cos \theta \cos \alpha - i \sin \alpha) e^{-i\phi}. \quad (\text{A.31})$$



## Appendix B

# AtomicDensityMatrix package for Mathematica<sup>®</sup>

In atomic physics, most of the time we tackle the interaction between an atom and light using the optical Bloch equations (OBE). If we include in the problem many atomic states, then the mathematical complexity increases and it is more convenient to use a software like Mathematica<sup>®</sup>. Simon Rochester (Dimitry Budker's group) wrote a very useful package called AtomicDensityMatrix (ADM) that generate a set of OBE. The package can be found at <http://budker.berkeley.edu/ADM/>. In this section, we demonstrate the usage of this package to generate OBE relevant to the analysis of the Hanle effect in Chapter 6.

Once the ADM package is installed, we can start using it by calling

```
<<AtomicDensityMatrix`
```

Then we disable the time-dependence option:

```
SetOptions[DensityMatrix, TimeDependence -> False]
```

Next we define the states of the system. In this case there are 4 states

```
system = {AtomicState[1], AtomicState[2], AtomicState[3], AtomicState[4]};
```

To check that we have a reasonable set of state, use this command:

```
DensityMatrix[system]
```

Finally, to generate a set of OBE, we execute

```
eqs = LiouvilleEquation[system, H, A, B]; TableForm[eqs]
```

where the Hamiltonian  $H$  in the atom-laser interaction Hamiltonian is given by, for example,

$$H = \begin{pmatrix} \Delta_b - \epsilon & 0 & \Omega_L/2 & -\Omega_L/2 \\ 0 & \Delta_b + \epsilon & \Omega_L/2 & -\Omega_L/2 \\ \Omega_L/2 & \Omega_L/2 & -\epsilon/3 & 0 \\ -\Omega_L/2 & -\Omega_L/2 & 0 & \epsilon/3 \end{pmatrix}, \quad (\text{B.1})$$

$A$  is the matrix containing the decay of the excited state

$$A = \begin{pmatrix} 0 & 0 & 0 & 0 \\ 0 & 0 & 0 & 0 \\ 0 & 0 & \Gamma & 0 \\ 0 & 0 & 0 & \Gamma \end{pmatrix}. \quad (\text{B.2})$$

and  $B$  is any remaining term. In this case  $B$  contains population increase rate of the ground state from the decay of the excited state and laser linewidth,  $\gamma$ :

$$B = \begin{pmatrix} \frac{1}{3}p\Gamma\rho_{33} + \frac{2}{3}p\Gamma\rho_{44} & \frac{1}{3}p\Gamma\rho_{34} & -\gamma\rho_{13} & -\gamma\rho_{14} \\ \frac{1}{3}p\Gamma\rho_{43} & \frac{1}{3}p\Gamma\rho_{44} + \frac{2}{3}p\Gamma\rho_{33} & -\gamma\rho_{23} & -\gamma\rho_{24} \\ -\gamma\rho_{31} & -\gamma\rho_{32} & 0 & 0 \\ -\gamma\rho_{41} & -\gamma\rho_{42} & 0 & 0 \end{pmatrix}. \quad (\text{B.3})$$

# Appendix C

## Electronics and experiment controls

To make life as an experimentalist easier, most of laboratory equipment are computer controlled. In this chapter, the most important electronics used in our experiment are described. We also show how we use our software framework to control this equipment.

### C.1 Pulse sequencer and direct digital synthesizer (DDS)

The heart of the experiment control is the pulse sequencer (Pulser). This equipment provides an interface between a computer and other equipment, as shown in Fig. C-1. All experimental procedures consist of switching on and off lasers with the correct amplitudes and frequencies at the correct time. Typically, the time scale in modern trapped ions experiment ranges from a few microseconds to a few seconds. This is impossible to do manually. Hence, the sequencing of the laser pulses is carried out using a fast field-programmable-gate-array (FPGA) based on a 200 MHz clock.<sup>1</sup> This FPGA, together with the direct digital synthesizer (DDS) chips, generate TTL pulses and RF signals that control the lasers through AOMs.

The Pulser also collects data from the photo-multiplier tube (PMT) which detects photons scattered from an ion. The photon counting can be done independently using the Normal PMT counter. This is a simple counter which continuously counts the number of photons. Additionally, the photon counting can be tied to a pulse sequence. This is useful when we need to know the photon arrival time with respect to the timing of the pulse sequence.

---

<sup>1</sup>The VHDL code can be found at <https://github.com/HaeffnerLab/Haeffner-Lab-FPGA>.

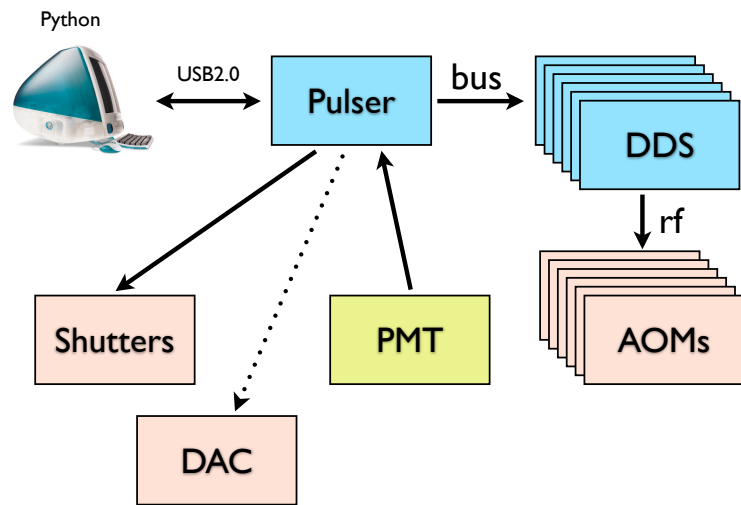


Figure C-1: Hardware wiring configuration for the Pulser.

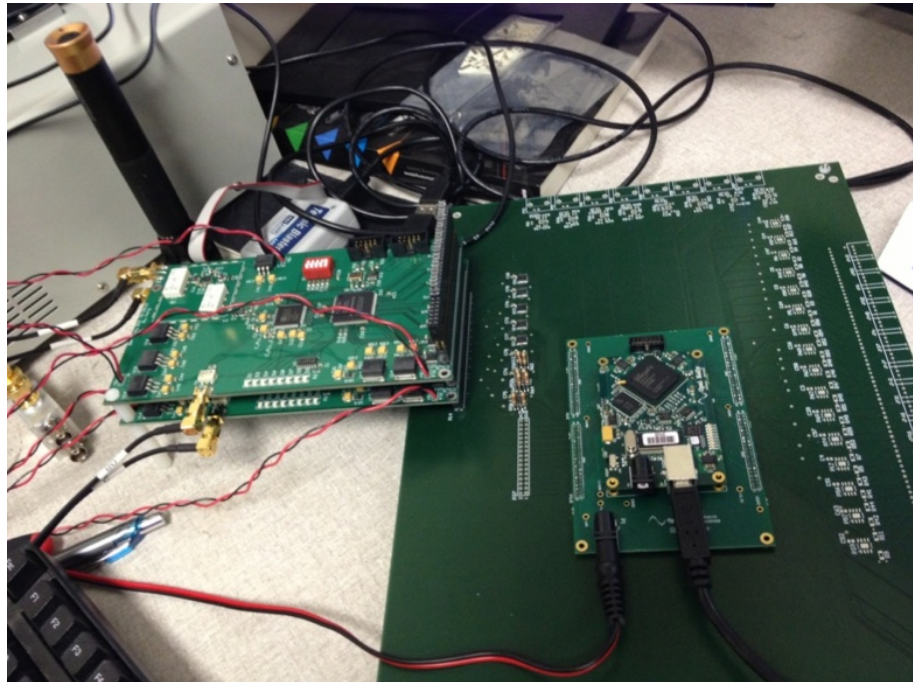


Figure C-2: The Pulse break-out board and two DDS boards under testing.

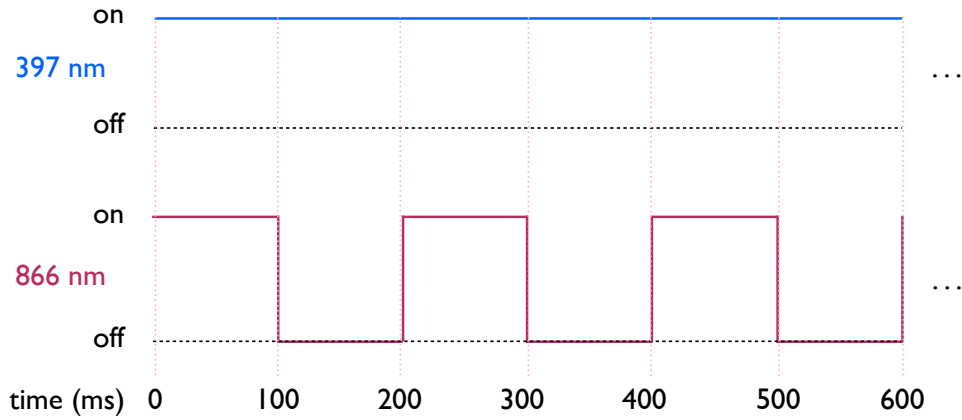


Figure C-3: Sample pulse sequence.

### C.1.1 Pulser

The Pulser uses XEM6010 module from Opal Kelly<sup>®</sup>. (The test setup is shown in Fig. C-2.) This is convenient since Opal Kelly provides a software framework in Python, which is our experiment control programming language. This makes transferring data easy and fast (through USB 2.0). The module itself uses a Spartan 6 FPGA from Xilinx<sup>®</sup>.

#### C.1.1.1 Theory of operation

The Pulser is essentially a programmable pulse sequencer. Its main function is to output trains of pulses in a well controlled way. Each pulse can be used to control a shutter, an AOM, a CCD camera or other equipment. This is essential for most of the ions trapping experiments since the experimental sequence has to be repeated many times to build up statistics. Data from the experiment is usually collected in the form of photons scattered by ions detected by a photo-multiplier tube (PMT).

A basic pulse sequence, for example, is the so-called “differential mode.” The sequence compares the fluorescence of the 397 nm light scattered by an ion when the 866 nm (repumper) is on and off.<sup>2</sup> This is extremely important in ion loading (especially when loading for the first time) because the 397 nm fluorescence from the ion might be buried under a background light. It is hard to conclude whether there is any ion in the trap or not. By using a differential photon counting mode, we subtract the signal when the 866 nm is on from the signal when the 866 nm is off and thus remove the background. Any signal after the subtraction indicates that there is an

---

<sup>2</sup>This is essentially a lock-in technique.

ion in the trap. Once some signal is obtained, other parameters (laser position, laser frequency, etc.) can be optimized to increase the signal.

The pulse sequence of this differential mode is represented in the time domain in Fig. C-3.

To minimize memory space used by the pulser to store the pulse configurations, the pulse sequence consists of looping of a smaller pulser sequence. In this particular case, the pulser is simply a looping of **866 nm on for 100 ms then 866 nm off for 100 ms while keeping 397 nm light on**. The Pulser stores this small pulse in its memory and loops this pulse until it is interrupted.

The pulse configuration is stored in the RAM of the Pulser. Each line of the RAM has 64 bit of data. The first 32 bit represents the channel of the pulse. For example, we might designate **397 nm to be channel 0 and 866 nm to be channel 1**. The last 32 bit is the time. This time is the time when there is any change in the state of the channel. To illustrate this, let us measure time in units of microseconds. A typical line in the RAM will look like [00....0011:250000]. This means that at time = **250000** (and right after), the state of channel 0 and 1 will be “high” or “1” and others to be “low” or “0.”

By convention, the first line of the RAM indicates the initial state of the channels. The RAM will look like this (we show only 4 channels for simplicity):

[Chanel(3..0):Time]

line1: [0011:000000] (At t = 0, channel1 = 1 and channel0 = 1)

line2: [0001:100000] (At t = 100 ms, change channel1 to 0 and channel0 to 1)

line3: [0011:200000] (At t = 200 ms, since the next line consists of t = 0, end the pulse)

line4: [0000:000000]

Note that the channel configuration in line3 does not really matter since it only indicates when the pulse ends (by having the next line to be all zeros). Once the pulse reaches the last line, we have an option to tell Pulser to loop the sequence by going to line1 again until we tell it to stop. Note that the limitation from the memory of the pulser is in the complexity on the pulse (how many times the state of the TTL changes in the pulse sequence) rather than the duration of the pulse.

### C.1.1.2 Time-resolved photon counting module

During the pulse sequence, we might want to know when a photon has been scattered by the ion. This is useful because we might care only about the number of photon detected during a small period in the pulse sequence (for example, only when far blue-detuned 397 nm light is on). We can also extract the information in the frequency domain of the scattered light by taking a Fourier transform of the arrival times of the collected photons.

In the main pulser module, there is a counter which keeps track of the time for each pulse sequence. In our particular case, the Pulser is running from a 100 MHz clock. So we have a counter which counts once every 10 ns. The time-resolved photon counter simply records the time in the memory whenever there is a photon detected

from the PMT. For example, after a pulse sequence, we might have in the memory of the time-resolved photon count module a series of numbers like this:

[000001]  
[000123]  
[000267]  
[000439]  
[001485].

This means after the pulse sequence has finished, we have detected 5 photons, with the arrival time at 10, 1230, 2670, 4390 and 14850 ns. One advantage of using a common clock between the main pulser module and the time-resolved photon counting module is that the arrival times of the photons in the time-resolved are always consistent with the timing in the pulse sequence. For example, if we care only the photon detected during the time  $t = 10$  ms to  $t = 20$  ms, we can disregard any data which has the arrival time outside  $t = 10$  ms to  $t = 20$  ms. Another advantage is when we loop the pulse sequence more than once, we might get a series of photon detected like this:

[000001]  
[000123]  
[000267]  
[000439]  
[001485]  
[000002]  
[000133]  
[000257]  
[000539]  
[001585].

This clearly indicates that the 6th photon and so on belong to the second iteration of the pulse sequence since the main counter of the time reset back to zero after the first iteration. This is beneficial because there is an overhead in data transfer from the memory on the Pulser to the computer. We can wait until the memory of the time-resolved photon counting module is almost full and transfer all the data in one set.

### C.1.1.3 Normal PMT counting

This module is rather independent from the rest of the Pulser. It counts how many photon detected in the PMT module during a given period of detection time. Normally the time period ranges from 10 ms to 1 s. The time period can be set to be automatic (where the counting is totally independent of the pulser) or tied to the pulse sequence (which we use, for example, in the differential counting mode).

## C.1.2 Direct digital synthesizer (DDS)

A direct digital synthesizer (DDS) is a generation of RF signal using a high speed digital-to-analog converter. The main chip used in our setup is AD9910 from Analog

Devices®. Generation of RF is crucial in switching the laser on and off using AOMs. Fig. C-4 shows the block diagram of the DDS board.

The DDS board, once configured, only listens to one of the channels of the Pulser to do frequency, amplitude and phase stepping of the RF. The configuration of the DDS is very similar to the way the main pulser module is configured. Information about the frequency and amplitude is stored in the RAM. Each line in the memory has 64 bit of data. The first 32 bits encode the frequency. The next 16 bits (though only 14 bits are currently used) is the amplitude. The last 16 bits represent the phase. There is no timing information on the DDS board. Once the TTL pulse is received from the Pulser, the DDS board steps to the next frequency/amplitude/phase in the RAM on the DDS board. (If the pulse sequence does not require any frequency/amplitude switching, the DDS will stay at the first frequency/amplitude/phase of the memory on each DDS board). If there are multiple DDS boards connected to the Pulser, all DDS boards share the same stepping TTL pulse. In this way, the number of I/O lines used to connect DDS boards to the Pulser is minimized. As of now, up to 8 DDS boards can be connected to Pulser. The frequency/amplitude/phase of each DDS is sent to each DDS board from the computer through a 16 bit bus.

### C.1.3 Using the Pulser

Most of the hardware configuration is on the FPGAs. We use VHDL to code these FPGAs. We will describe in detail the code structure of each module in this section.

#### C.1.3.1 Pulser

As mentioned before, the main FPGA of Pulser is Spartan 6 FPGA on the XEM6010 module. There are three ways of transferring data between XEM6010 and a PC: Wire, Pipe and Trigger. Wire is a physical signal on the FPGA which can be set from the PC. This is suitable for configuring the FPGA to be operating in a certain mode. Pipe is designed to handle heavy data transfer between the Pulser and the PC. This is used, for example, for writing a pulse sequence to the Pulser or reading time-resolved data from the Pulser. The Trigger is used mainly for resetting the pulse sequence or other modules on the FPGA.

**C.1.3.1.1 Programming the pulse sequence** To program the pulse sequence to the memory on the Pulser, first we generate a string of data to be transferred to Pulser. (A LabRad Python server written by Michael Ramm does this. A detailed description can be found in his Ph. D. thesis.) The data is written to the Pulser by using the command

```
xem.WriteToBlockPipeIn(0x80, 2, buf)
```

which will transfer all data to PipeIn stored in “buf” at address 0x80 on the Pulser. This data is first written to a first-in-first-out (FIFO) memory on the Pulser. This is required because the data transfer of XEM6010 is done on a 48 MHz clock (USB 2.0 clock frequency) which operates somewhat independently from the main clock of the

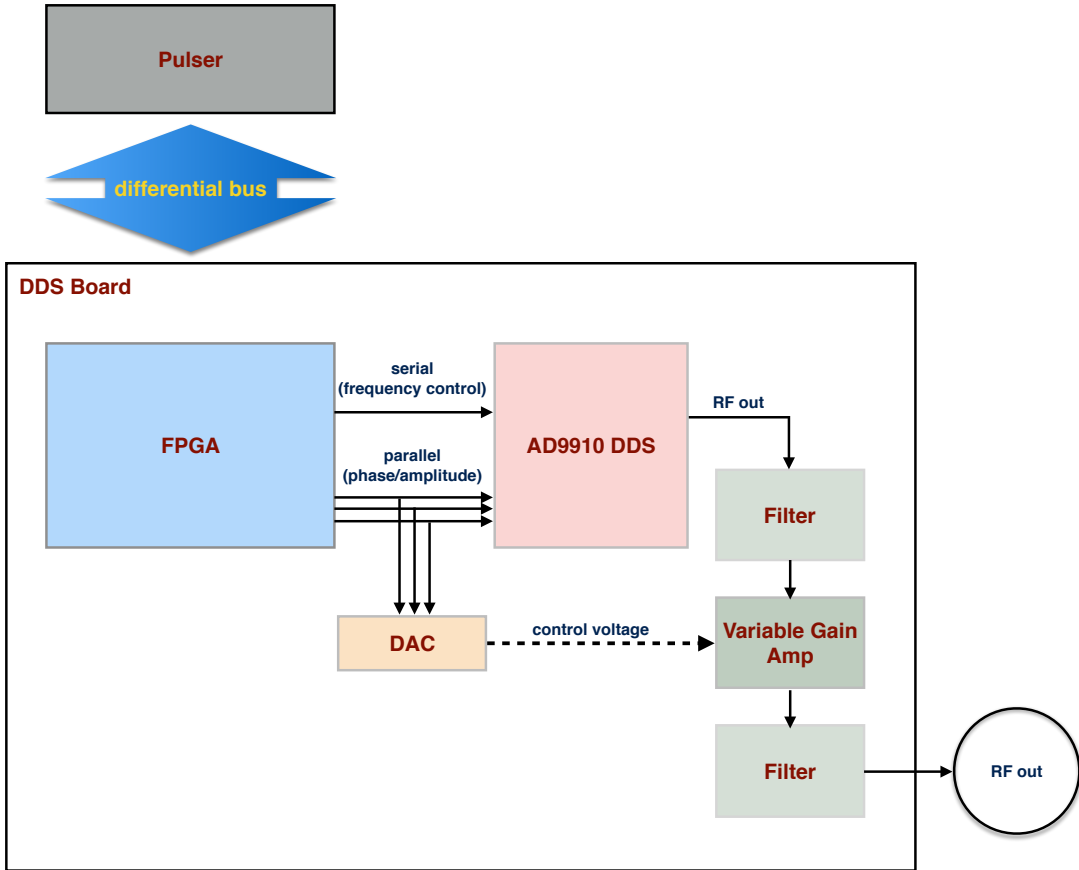


Figure C-4: Block diagram of the DDS board.

FPGA (which is 100 MHz). Once there is some data in the FIFO, the “FIFO empty” pin of the FIFO is set to low. There is a process (call “RAM writer”) in the FPGA which monitors the state of this pin and writes data from the FIFO to the RAM until data in the FIFO is empty. Since the PipeIn data transfer from the PC is done in a chunk of 16 bit, the input of the FIFO is 16 bit wide but the output of the FIFO is 64 bit wide. To program a new pulse sequence, simply run

```
xem.ActivateTriggerIn(0x40,1)
```

This command tells the RAM writer to write to address 0 of the RAM when there is anything in the FIFO.

The RAM is configured to be a simple dual-port RAM (single input and single output). Both the input and the output are 64 bit wide. The input is handled automatically by the RAM writer. The main pulser module looks at the time and channel configurations on the RAM and steps through each line until the last line is reached. Then depending on the mode (whether it is in a looping mode or a one-shot mode), the Pulser will stop or repeat itself.

Note that the clock of the FPGA is running at 100 MHz. The pulse sequence, however, does not require a resolution of 10 ns. There is a coarse counter which runs at 25 MHz and a fine counter which runs at 100 MHz. The pulse sequence timing is based on the 25 MHz time (so that the unit of the timing in the RAM is in 40 ns). The 100 MHz fine counter is used only by the time-resolved photon counting module which requires high timing resolutions.

**C.1.3.1.2 Logic\_out overwrite** The state of each channel of the pulse sequence is stored in a 32 bit vector called master\_logic in the VHDL code. However, there are applications where users need to overwrite the logic of particular channels manually. Each channel is then gated with a manual control logic (ep02wire and ep03wire) set by users. The configuration is:

**If ep02 = '0' and ep 03 = '0', then output follow master\_logic, If ep02 = '0' and ep 03 = '1', then output invert master\_logic, If ep02 = '1' and ep 03 = '0', then output is always '0' and If ep02 = '1' and ep 03 = '1', then output is always '1'.**

**C.1.3.1.3 Time-resolved photon counting** To record the arrival time of each photon detected from the PMT, there is a FIFO (32-bit wide memory) which is written every time a photon is detected. This is done by tying the write\_clk pin of the FIFO to the PMT signal. We also tie the write\_enable pin to one of the channels of the pulse sequence to selectively record photons only when we want to (to reduce the memory used). The timing, as mentioned before, is the same timing used for the pulser module.

The reading is done through a PipeOUT channel A0 by using the command

```
buf = "\x00"*2*2*320
xem.ReadFromBlockPipeOut(0xa0,2,buf)
```

```

a = Struct("H"*(len(buf)/2))
Struct.unpack(a,buf)

```

where the length of “buf” depends on how many photon there are in the FIFO. The Struct method is used to convert binary data to an integer. The number of photons in the FIFO can be read using the command

```

xem.UpdateWireOuts()
xem.GetWireOutValue(0x22)

```

Since PipeOUT reads in a chunk 16 bit, the output of the FIFO is 16 bit wide where the input is 32 bit wide. This means that the max “read\_data\_count” of this FIFO is 65536 lines corresponding to 32768 photons. With this in mind, we have to make sure that we are not filling up the FIFO before reading it out. This limitation, however, could be overcome by implementing SDRAM on the XEM6010 board.

**C.1.3.1.4 Normal PMT Counting** Normal PMT counting is a bit more complicated because there is a counter which we have to reset every counting period. This counter will increase by 1 every time there is a signal from the PMT. There are two modes: automatic and differential modes. In the automatic mode, the Normal PMT modules measure the photons independent of the pulse sequence. We set the counting period manually using

```

xem.SetWireInValue(0x01,0x0064)
xem.UpdateWireIns()

```

In the differential mode, the counting period is tied to one of the channel of the pulser sequence. Basically, the Normal PMT counting process waits for a TTL pulse from the PMT. When it detects a pulse, it writes the data in the counter to the FIFO (which is 32 bit wide) and then resets the counter and wait for the next pulse. In principle, there is a down time of the counter (when it is being reset). However, the down time is short enough such that it does not change the number of photons counted during a period of 100 ms for our typical photon count rate of  $20 - 30 \times 10^3$  counts/s. The most significant bit of the data in the FIFO (bit 32) indicated whether the 866 nm is on or off in the differential mode. The reading of normal PMT count is done by first asking how much data is there in the FIFO by calling

```

xem.SetWireInValue(0x00,0x40,0xf0)
xem.UpdateWireIns()
xem.UpdateWireOuts()
xem.GetWireOutValue(0x21)

```

then read by calling

```

buf = "\x00"*2*2*32
xem.ReadFromBlockPipeOut(0xa1,2,buf)
a = Struct("H"*(len(buf)/2))
Struct.unpack(a,buf)

```

Note that ep21wire displays information depending on bit (7..5) of ep00wire. This is to reduce the number of Wire modules used in the Pulser.

### C.1.3.2 DDS

**C.1.3.2.1 Pulser side** To program the DDS board, users have to write data to the FIFO on the Pulser similar to the way we write the pulse sequence. The FIFO is 16-bit in and 16-bit out. Now, the RAM module is on the FPGA on the DDS board. There is a RAM writer in the FPGA on each DDS board which checks if there is any data on the FIFO on the Pulser. If there is, then it writes the data to the RAM. The RF output of the DDS is automatically set to the frequency, amplitude and phase of the first address of the RAM. Then the DDS board steps to the next setting if there is a pulse from the Pulser.

Since all DDS boards share the same bus, to program the right DDS board, the user has to first set which board to program by calling

```
xem.SetWireInValue(0x04,0x00)  
xem.UpdateWireIns()
```

and then write the DDS data using

```
xem.WriteToBlockPipeIn(0x81, 2, "\x02\x00\x00\x00\x00\xef")
```

Note that PipeIn address is 81 instead of 80 (which is used for pulse sequences). We can also reset all DDS boards and step all DDS boards to the next frequency/amplitude/phase by calling

```
xem.ActivateTriggerIn(0x40,4)
```

and

```
xem.ActivateTriggerIn(0x40,5)
```

respectively. Only the selected DDS board listens to these triggers. One thing to remember is that we cannot selectively step a particular DDS board. We have to step all DDS boards at the same time. In this sense when operating a pulse sequence that contains frequency/amplitude/phase stepping, we have to program all DDS channels accordingly so that all DDS boards behave correctly.

**C.1.3.2.2 DDS side** We also have to program the FPGA on the DDS board. As mentioned in the previous section, there is a RAM writer which looks at the FIFO on the Pulser to see if there is any data in the FIFO. If there is, then the Pulse writes that data to the RAM on the DDS board. The output of the RAM is rather simple. There is a RAM read address which increases by one every time there is a “step to the next parameter” pulse. The output is written to the DDS chip (for frequency) and a variable gain amplifier (for amplitude) on each DDS board.

The DDS chip needs to be programmed before it is functional. This happens every time the DDS boards are powered on. Please refer to the datasheet of AD9910 for details. The chip configuration we are using is

- Frequency tuning through parallel port

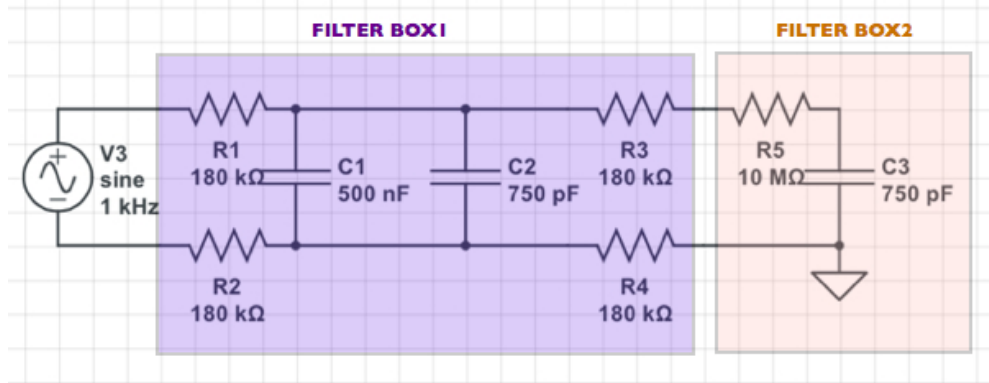


Figure C-5: Filtering of DC voltages. The four  $180\text{ k}\Omega$  resistors are for decoupling both the ground and the signal of the electrodes from the DC power supplies.

- Input clock without dividing by 2
- PLL enabled (800 MHz)
- Disable RAM functionality on the DDS chip
- Retain old data when TxENABLE is asserted low

The address of the board is set by a DIP switch. The LEDs are used for debugging. The DDS board also has an on-board 25 MHz oscillator which lets us use the DDS board as a stand alone RF source. If this is the case, then the PLL of the DDS chip must be enabled. However, the noise floor is higher when operating in this mode. Normally there is a jumper which disconnects the power to the oscillator (P10).

## C.2 DC voltage control using digital-to-analog converter (DAC)

DC voltages on the end caps provide a confinement in the axial direction. These voltages are generated by an AD660 (Analog Devices<sup>®</sup>) chip, which provide a 16-bit  $\pm 10\text{ V}$  of voltage amplified by an op-amp OPA554 (Texas Instrument<sup>®</sup>) to reach  $\pm 40\text{ V}$ . The PC controls two DAC channels for the two end caps through an Opal Kelly<sup>®</sup> XEM6001 module (with Spartan<sup>®</sup> 6 FPGA on board).

Each DC channel is filtered with a low-pass filter to remove electrical noise which can heat up the ion. The most important frequency to filter are the secular frequencies, which for our case from 150 kHz to 3 MHz. This is done using a circuit shown in Fig. C-5. The most important components are the capacitors, which should be verified to work well at the drive frequency (30 MHz).